METAL SULFIDES SEMICONDUCTING MATERIALS: CASE STUDIES ON CADMIUM SULFIDE/CARBON NANOTUBES AND IRON DISULFIDE

Marcos Flávio de Oliveira Silva

Agosto – 2016

METAL SULFIDES SEMICONDUCTING MATERIALS: CASE STUDIES ON CADMIUM SULFIDE/CARBON NANOTUBES AND IRON DISULFIDE

Marcos Flávio de Oliveira Silva

Orientador: Wagner Nunes Rodrigues

Co-Orientador: André Santarosa Ferlauto

Tese apresentada à Universidade Federal de Minas Gerais como requisito parcial para a obtenção de grau de Doutor em física.

Belo Horizonte, Minas Gerais

Agosto – 2016

“Let us cultivate our gardens”

Voltaire

AGRADECIMENTOS

Gostaria de agradecer a pessoas muito especiais, sem as quais não teria sido possível realizar o presente trabalho.

Primeiramente aos meus pais, pelo amor e apoio incondicionais, seguido pelos meus irmãos, amizades eternas, companheiros de, literalmente, todas as etapas da minha vida.

Aos meus orientadores, Wagner e André, pela orientação e dedicação.

À Lígia Parreira, pessoa tão especial que fica difícil expor em algumas poucas linhas tudo o que ela representa em minha vida. Namorada, amiga, companheira, muito obrigada por encher os meus dias de alegria.

Aos amigos e especialistas, Breno, Orlando, Guidão, Lúcio, Bolha, Laurinho, William, e Pedro e suas respectivas namoradas/esposas. Por todas as viagens, reuniões, “sextas-feiras”, conselhos. Serei eternamente grato pelas suas amizades.

Aos amigos do DF, em especial da turma de 2005. Sempre me lembrarei dos momentos que compartilhamos, das “sofrências” em salas de estudo, das festas, das amizades que ficaram. Desejo a todos, sucesso no caminho que trilharem. Dedico um agradecimento especial ao Clyffe e sua família.

A todos os companheiros de casa, Rapaiz, Lobão, Moleques, Medeiros, Felipe e Davi e Frank. Aprendi muito com todos vocês. Em especial, um agradecimento ao Medeiros pelos seus ensinamentos nordestinos. “Sucesso nas tuas vidas”.

A todos os funcionários do DF da UFMG, pelo profissionalismos e eficiência. Em especial, à Shirley, que, além de excelente profissional possui uma simpatia cativante.

Ao Sérgio, que foi de tudo um pouco durante o trabalho. Guru, amigo, conselheiro, um obrigado especial.

Aos funcionários da oficina mecânica do DF, Seu João (que falta vai fazer) e Thiago.

Aos professores do colegiado por terem me permitido terminar o trabalho.

Às agências de fomento de pesquisa Fapemig, Capes e CNPq por contribuírem com o desenvolvimento da pesquisa no Brasil.

RESUMO

Neste trabalho, nós estudamos a síntese e propriedades de sulfetos metálicos. Primeiro, analisamos o alinhamento de bandas de energia na interface de nanopartículas de sulfeto de cádmio com nanotubos de carbono de paredes múltiplas por espectroscopia de fotoelétrons (PES). Nós observamos a formação de contato ôhmico entre o semicondutor (CdS) e os nanotubos de carbono, que possuem caráter metálico, o que também foi verificado por PES. Nós também estudamos o crescimento de filmes de pirita (FeS_2) por *Aerosol Assisted Chemical Vapor Deposition* (AACVD) e sulfurização de óxido de ferro. Os processos de AACVD foram realizados em um reator cuja construção fez parte do trabalho. Os filmes depositados por AACVD apresentaram cor preta opaca e baixa aderência ao substrato, uma composição marcada por variadas misturas de diferentes fases de sulfeto de ferro e uma microestrutura descontínua, formada por várias placas desconexas. Por outro lado, os filmes produzidos através de sulfurização apresentaram cor dourada-escura especular e boa adesão ao substrato. Os processos de sulfurização ocorreram em um novo aparato implementado durante o trabalho, o qual chamamos de Boneca Russa. Nós variamos diversos parâmetros do processo e determinamos uma rota ótima para obter um material com fase pura de pirita. Nós investigamos a influência das propriedades do óxido precursor nas propriedades microestruturais e ópticas do filme sulfurizado e observamos que óxidos com grãos maiores, quando sulfurizados, resultam em dissulfetos também com grãos maiores. Observamos, também, que a qualidade dos precursores influencia as propriedades ópticas da pirita sulfurizada. Todos os filmes com fase pura de pirita apresentaram condutividade do tipo n. Por fim, iniciamos um estudo do processo de sulfurização, usando o novo aparato da Boneca Russa, de outros sulfetos metálicos, MoS_2 e SnS.

ABSTRACT

In this work, we studied the synthesis and properties of metal sulfides. First, we analyzed the energy band alignment at the interface of CdS nanoparticles and metallic MWCNTs by photoelectron spectroscopy, and observed the formation of ohmic contact between the materials. Then, we studied the synthesis of iron pyrite (FeS_2) films by Aerosol Assisted Chemical Vapor Deposition (AACVD) and sulfurization of spin-coated iron oxide (Fe_2O_3) films. AACVD processes were carried out in a reactor built during the realization of this work. The films deposited by AACVD presented opaque black color, poor adhesion to the substrate, mix composition of different iron sulfides and did not show continuous microstructure. Conversely, pyrite films produced by sulfurization presented dark golden specular color and good adhesion to the substrate. The films were sulfurized in a novel apparatus we named Russian Doll. We varied several sulfurization parameters obtaining several different resulting compositions. We determined an optimum route to obtain pure phase good quality films. We investigated the influence of the precursor Fe_2O_3 films in the microstructure of the sulfurized films and observed that oxide films with larger particles resulted in FeS_2 films with larger particles as well. Additionally, we observed that oxide films with varying physical properties also influenced the optical properties of the FeS_2 films. All pure phase pyrite films produced presented n-type conductivity. Lastly, we tested the use of our apparatus to produce MoS_2 and SnS, which have interesting potential applications.

PREFACE

Materials science play a crucial role in applied research. The efficiency of every device is firstly related to individual properties of the constituent materials. Hence, scientists are always pursuing new materials or refining the ones already known, in order to unveil new possible applications or to improve them further. In this context, metal sulfides represent a very important class of materials, since they spam a wide variety of different structures with a wide variety of physical properties. From the well-known CdS, to the layered MoS_2, this class of materials has always been present in materials science history. This work presents our contributions to this field.

We begin by presenting, in Chapter 1, a study of the interface electronic properties of CdS nanocrystals decorating multi-walled carbon nanotubes. CdS is, perhaps, the oldest and most used metal sulfide used for photovoltaic applications. Between the 1950s and the 1970s, CdS was part of the only exclusively thin film solar cell, forming a heterojunction with copper sulfide. Even though such structure was later found inefficient due to elemental diffusion at the interface, CdS continued to be used in solar cells, mainly as window layer. The material is also widely used in light dependent resistors (LDRs). In early 2000s, with the rise of nanotechnology and carbon nanotubes, scientists began to study hybrid semiconductor/carbon nanotubes composite materials for various applications, including photovoltaics. Multi-walled carbon nanotubes were of particular interest to act as charge collectors for semiconductor nanoparticles, due to its favorable electrical conduction properties. Furthermore, the CdS/multi-walled carbon nanotubes became particularly interesting when unusual high photocurrents were reported. Despite the reports of several synthesis studies and successful applications of these hybrid composite materials, little information regarding the interface of the constituent materials remained. Thus, we decided to explore such information gap and unveil the electronic behavior of the CdS/multi-walled carbon nanotube interface. We performed the analysis with photoelectron spectroscopy, one of the most important techniques for studies regarding band alignments at various interfaces. The work was published in Applied Surface Science in 2014.

Later, we set CdS aside to pursue a less aggressive (CdS is highly toxic due to the presence of cadmium, a heavy metal) alternative material for solar cell applications. The idea was to combine both potential for solar to electrical energy conversion with environmental friendly characteristics. With that in mind, we turned to iron pyrite (FeS_2), a metal sulfide that recently, in 2009, was on display for having those exact credentials: its constituents are abundant, present low toxicity, and the material has favorable optical properties enabling its use for photovoltaic applications.

In chapter 2 we present an overview of the material regarding: phase compositions of the Fe:S system and the polymorphic behavior of FeS_2; physical properties of iron pyrite; the background in the synthesis of the material by various techniques; and the advances in pyrite based devices with the respective performances. We show that, even though the first pyrite based device was built in mid 1980s, only recently, in 2014, researchers made fundamental discoveries regarding intrinsic properties of the material which directly affects the performance of any pyrite device. For instance, such discoveries enlightened the problem with persistent low V_{OC} reported in pyrite based solar cells. Therefore, there is still a lot of ground to cover concerning synthesis and understating of the physical properties of FeS_2 in order to extract the full potential of the material. In chapters 3 and 4 we present our contribution to this work. Amongst the several techniques listed in chapter 2, we chose to work with two: Aerosol Assisted Chemical Vapor Deposition (AACVD) and sulfurization of iron oxide thin films. The first technique, whose results are presented in chapter 3, was drawn to our attention due to the possibility of using single source precursors, like dithiocarbamates. Such molecules were widely studied in the research group of Professor Geraldo de Lima in the Chemistry Department of UFMG, and so, a collaboration was established. We even built a reactor to study the effect of several synthesis parameters in the phase composition and microstructure of FeS_2 films. Unfortunately, the materials deposited with the homemade reactor were all sulfur deficient and were poorly adherent, ultimately driving us to the path of the second technique: sulfurization.

In chapter 4, we present the study on sulfurization of spin-coated iron oxide films, using an apparatus implemented by us in the Laboratory of Nanomaterials. We named it the

Russian Doll apparatus, for its resemblance to the Matrioska toy, and we discuss in the text the advantages it has over other sulfurization apparatus and methods, such as ampoules and H_2S flow. Several of the works discussed in the historical reference in chapter 2 regard their produced material as pure phase iron pyrite, solely by an analysis of X-ray diffraction (XRD) patterns. However, one may mistake the actual composition of iron sulfide films with only XRD results in hand. In some cases, even though XRD detect no traces of secondary phases, other characterization techniques may assure the existence of such phases. For instance, in our case, Scanning Electron Microscopy (SEM) showed the coexistence of more than one iron sulfide phases in cases where XRD could not. Moreover, when producing FeS_2 films by sulfurization of Fe_2O_3, little is known about the influence of the precursor oxide in the resulting sulfide. Our works also marks a contribution in this scenario, exposing the effect of varying microstructure and physical properties of the spin-coated iron oxide on the microstructure and physical properties of the sulfurized pyrite films. We published our results concerning the sulfurization of Fe_2O_3 in Thin Solid Films, in 2016.

Recently, two other members of the “metal sulfides” class of materials gained the spotlights: molybdenum disulfide (MoS_2) and tin sulfide (SnS). MoS_2, as part of the advent of 2D materials that took place after the discovery of graphene, ultimately granting the pioneer work a Nobel Prize in 2010. Like other 2D materials, MoS_2 has interesting tuning properties that relate to the number of layers of a given sample. On the other hand, SnS hass drawn the attention of the scientific community for reasons similar to iron pyrite. With a high optical absorption and favorable energy gap value, the **p**-type SnS is of particular interest for us, since all the pure phase pyrite films we produced presented **n**-type behavior. Hence, in chapter 5, we present preliminary results on the synthesis of MoS_2 and SnS, using our Russian Doll apparatus to sulfurize sputtered Mo and spin-coated tin oxide thin films, respectively.

Contents

1 Study of the CdS-MWCNTs interface

In this chapter, we present the study published in Applied Surface Science regarding the determination of the band alignment of cadmium sulfide (CdS) nanoparticles (NPs) at the interface with multi-walled carbon nanotubes (MWCNTs). First, we discuss the principles of photoelectron spectroscopy, which was the technique used to analyze the energy levels at the interface. Then, we show how one may extract information about the band bending of energy levels at an interface by means of photoelectrons spectroscopy and demonstrate the procedure for the case of CdS nanoparticles decorating MWCNTs. We show that the materials formed an ohmic contact, which justifies the use of MWCNTs as a charge collector material which has been suggested to improve the efficiency of devices.

1.1 INTRODUCTION

Since carbon nanotubes (CNTs) were first reported by Iijima [1], they have attracted the attention of scientists in many areas due to their extraordinary mechanical, chemical, and electronic features [2]. Their electrical transport efficiency grants them a huge potential for use in sensors, transistors, and other technological applications [3,4]. Surface modification of CNTs with organic, inorganic or biological species may dramatically alter their electronic characteristics further broadening their potential use [5]. Semiconductor nanoparticles (NPs) have also attracted the interest of many researchers in recent decades, because of their unique size-tunable properties resulting from quantum confinement [6]. The control and development of new features according to the size of the particles is of great technological value. Within the great number of possible applications for this class of material, we highlight optical sensors and other optoelectronic devices. The nanometer size of the NPs provides shorter pathways for charge carriers, which reduces the probability of charge recombination inside the crystal. On the other hand, charge transport across particles is poor, which leads to high recombination rates at their interfaces and limits the mobility and efficiency of electronic devices based on NPs. Thus, in order to overcome this limitation, the use of a charge-collecting material attached directly to the NPs has been suggested [7].

Many authors have reported successful decoration of CNTs with semiconductor NPs over the years. Shi *et al.* attached cadmium sulfide (CdS) NPs on multi-walled carbon nanotubes (MWCNTs) [8]; Ravindram *et al.* covalently coupled ZnS capped CdSe to acid-treated MWCNTs [9]; and others have proposed methods to attach other semiconductors, such as TiO_2,SnO_2, ZnS, and CdSe to CNTs, thus presenting the possibility of CNTs functioning as a charge collector [10,11,12,13]. The CdS/CNT composite is of particular interest, since it was shown capable of generating photocurrent from visible light with unusually high efficiency [14]. However, despite the many reports on the synthesis of NP/CNT composites, there is little information about the electronic properties of the resulting interfaces.

In the next sections, we describe our recent work where we used X-ray and ultraviolet photoelectron spectroscopies (XPS and UPS, respectively) to determine the band alignment of CdS NPs decorating metallic MWCNTs. Our approach is based on the work of Kraut *et al.* [15] and, since then, many groups have used similar approach to study the band alignment in interfaces of different materials mostly thin films [16,17,18,19,20,21]. Firstly, we will discuss the principles of photoelectron spectroscopies.

1.2 PHOTOELECTRON SPECTROSCOPY

Photoelectron spectroscopy (PES) is an old experimental technique widely used to study surfaces. Hertz first detected the photoemission phenomenon in 1887, when he observed that he could activate a secondary discharge arc by means of the radiation produced by a primary arc when certain materials were introduced in between [22]. The electron was discovered later in 1897 and the effect observed by Hertz was then attributed to the emission of the recently discovered particle by ultraviolet radiation. In 1905, Einstein used the new concept of the quantum nature of light, suggested by Planck in 1900, to explain in details the photoelectric effect by means of the interaction of electrons with photons [23].

In principle, PES is performed today almost in the same way as it did a century ago [24]. PES consists of ionizing a material with radiation and measuring the spectrum of kinetic energy of the emitted electrons, as depicted in Fig. 1.1. The light source is either a gas discharge lamp (ultraviolet, UV frequency), an X-ray tube or a synchrotron radiation source. Each electron is differently bonded to the bulk by an energy – here and afterwards referred as the binding energy (BE) and it is determined in reference to the Fermi level (E_f) – as determined by the electronic structure of the sample. The spectrum of kinetic energies (E_K) measured in a PES experiment is given by:

$$E_K = h\nu - \mathrm{BE} - \Phi_{sample}, \qquad [1.1]$$

where, Φ_S is the work function of the sample, and hν is the energy of the irradiated photon.

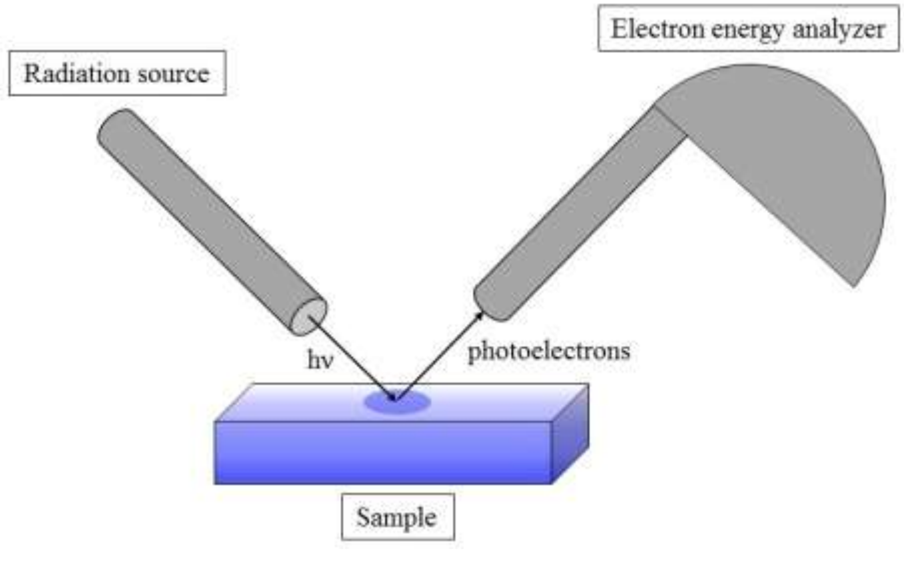

Fig. 1.1: Schematic illustration of a photoelectron spectroscopy measurement. The source of radiation is either a UV or an X-ray source.

Fig. 1.2 schematically shows the relation between the energy distribution diagram – N(E) – of a given solid and the energy distribution – N'(E) – of the kinetic energy of photoemitted electrons in a given experiment. Note that the regions of the electronic structure excited depend on the energy of the radiation source used. When using a gas discharge lamp to produce UV light, one extracts electrons near the Fermi level (in the case of metals) or near the edge of the valence band (in the case of semiconductors). Therefore, UV light is best suited to study the valence structure of materials. In the figure, E_{cutoff} corresponds to an electron with $E_K = 0$. On the other hand, X-rays ionize deeper level electrons, up to electrons near the valence band edge. Thus, X-ray photoelectron spectroscopy (XPS) provides a more complete information about the electronic structure of the analyzed sample. XPS is widely used to characterize the chemical composition of materials, including identification of constituent elements, relative compositional ratio, chemical state of a given element, and more.

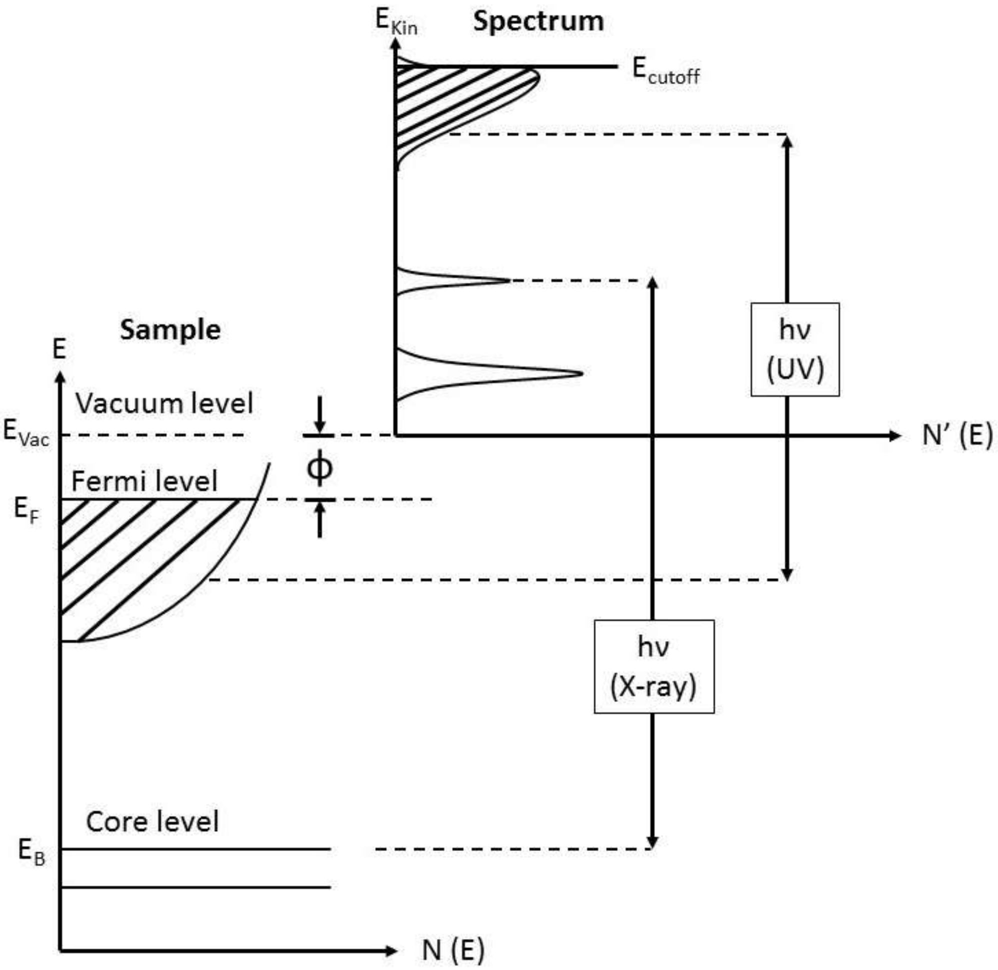

Fig. 1.2: Schematically illustration of the relation between the energy-level diagram of a solid and the energy distribution of photoemitted electrons.

An important step to perform when analyzing a PES spectrum is to determine the kinetic energy of the electron emitted from E_f, establishing the maximum value of the kinetic energy in the spectrum, defined here as E_{Kf}. This procedure depends on whether the material analyzed is i) a metal or ii) a semiconductor.

In the first case, we use the Fermi-Dirac distribution – f(E), as elicited below – as a model for the energy distribution close to E_{Kf} in the spectrum.

$$f(E) = \frac{1}{e^{(E-E_F)/kT}+1}, \qquad [1.2]$$

f(E) represents the probability of a given electronic state to be occupied, considering Pauli`s exclusion principle. At T = 0, all states below E_f are occupied, meaning, f(E) is given by:

$$f(E) = \begin{cases} 1, E < E_F \\ 0, E > E_F \end{cases} \qquad [1.3]$$

For different temperatures, the small energy kT – at room temperature, kT is approximately 25 meV – excites electrons from states with energies a little lower than E_f to states with energies a little higher than E_f. As a consequence, f(E) differs from the form described in eq. 1.2 in an energy range of ~ kT around E_f. Fig. 1.3 depicts the forms of f(E) for both T = 0, and T ≠ 0.

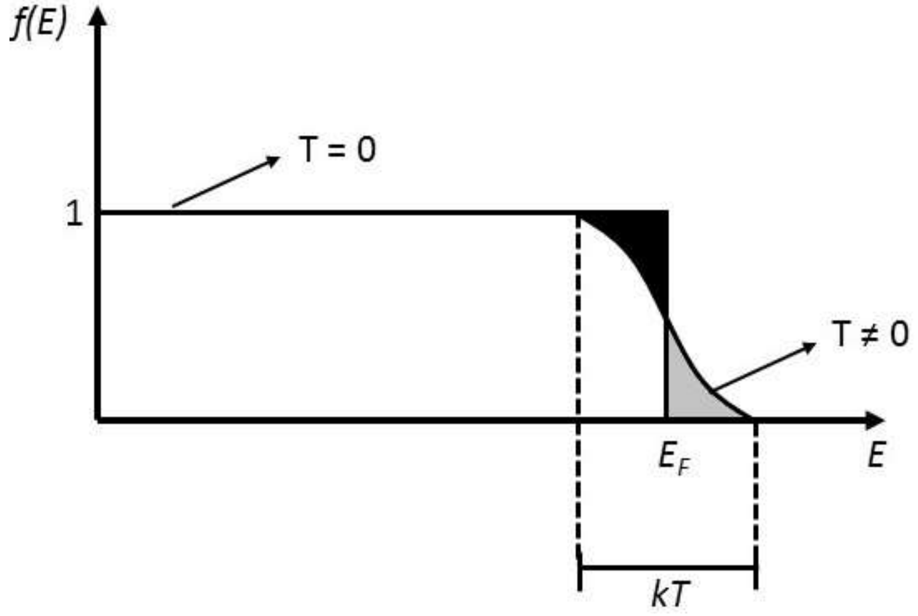

Fig. 1.3: Fermi-Dirac distribution at zero and nonzero T. At zero T, all states up to EF are occupied, and f(E) is given by eq (4). At nonzero T, electrons just below EF (darkly shaded area) are excited to states just above E_f (lightly shaded area).

The kinetic energy spectrum of a given PES experiment with metal samples approaches, then, a distribution function close to the one showed in Fig. 1.3 (T ≠ 0) for values around E_{Kf}.

Therefore, as mentioned before, we may plot this region of the spectrum with a suitable f(E) – *i.e*, with a suitable value for T – to extract the precise value of E_{Kf}, as illustrated in Fig. 1.4. Another simpler possibility lies on the symmetry around E_f for temperatures above zero. Since all the electrons that occupied the states just below E_f were thermally excited to the states equally just above E_f, as shown in Fig. 1.3, the value of E_f may be determined by the midpoint in the curve region that differs from the T = 0 case. This value may be accurately determined by the zero value of the second derivative of the spectrum (inflexion point).

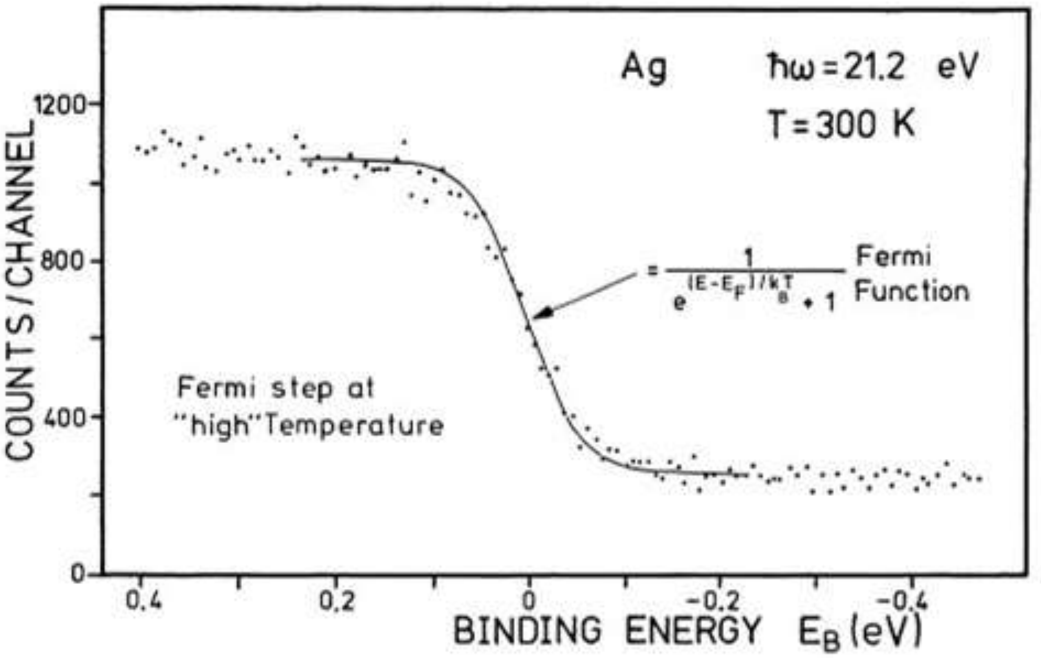

Fig. 1.4: Example of the use of f(E) to determine E_f in a UPS experiment.

In the second case (semiconductor sample), E_f lies, in an intrinsic semiconductor, in the middle of the energy gap, *i.e*, between the conduction and the valence bands. If the semiconductor is doped (extrinsic semiconductor), E_f shifts towards the valence band (**p**-type) doping or the conduction band (**n**-type doping) due to the thermal excitation of electrons in localized acceptor and donor states, respectively. In either case, E_f is still located between the valence and conduction bands. The localization of E_f in the Eg area for semiconductors means that, when performing a PES experiment in this class of material, the electrons with the higher kinetic energies will be excited from the valence band maximum (E_{VBM}) and not from E_f. However, it is still possible to determine E_{Kf}, and, furthermore, to determine position of the valence band maximum (E_{VBM}) in reference to E_f. All the possibilities (intrinsic and both types of extrinsic semiconductors) are illustrated in Fig. 1.5.

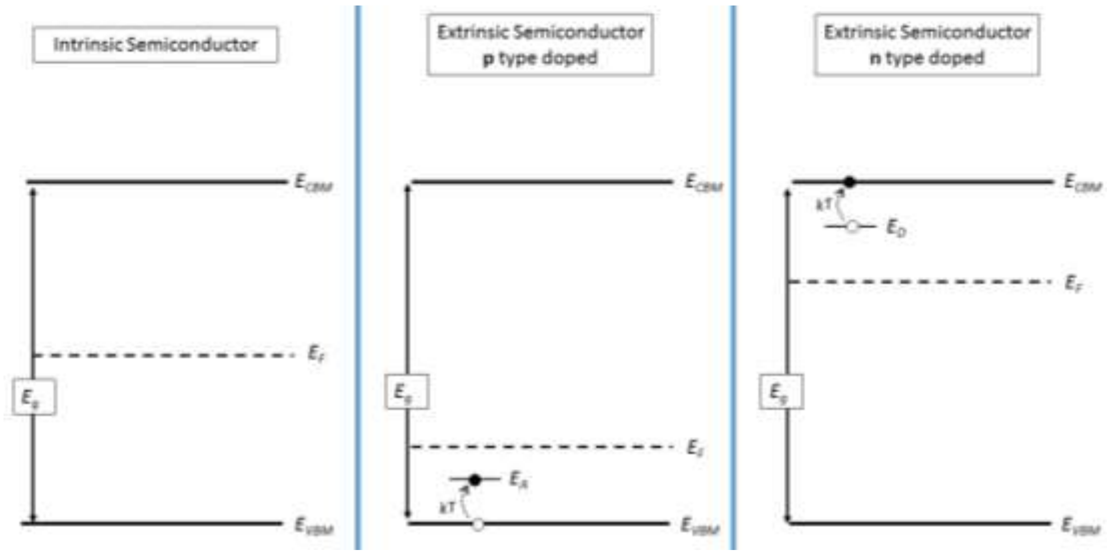

Fig. 1.5: Energy diagram of three types of semiconductors, intrinsic (left), **p**-type doped (center) and **n**-type doped (right), showing the position of the Fermi level (E_f), valence band maximum (E_{VBM}) and conduction band minimum (E_{CBM}). E_A and E_D represent, respectively, the acceptor and donor localized states.

One may determine E_{VBM} following a similar procedure adopted in the case of metals. For metals, one fits the measured spectrum around the expected value of E_f with f(E), whereas for semiconductors, Kraut *et al.* demonstrated that using a nonlocal pseudo-potential (Chelikowsky-Cohen[25]) to model the valence band density of states (V_{BDOS}) of the semiconductor, it is possible to determine E_{VBM} with excellent precision [15]. The authors also used an instrumental resolution function g(E) to represent the broadening of the spectrum caused by the equipment. The V_{BDOS}, according to Kraut, is given by:

$$N_v(E) = \int_0^{\infty} n_v(E')g(E-E')dE' \,, \qquad [1.4]$$

where $n_v(E)$ is the Chelikowsky-Cohen nonlocal pseudo-potential, and g(E) is the instrumental resolution function. Using equation (5) to fit the experimental data, the authors determined E_{VBM} with a precision of ± 0.03 eV.

A simpler procedure used to determine E_{VBM} in a PES experiment, though, consists on linearly extrapolating both the end of the spectrum and the baseline. The intersection between the extrapolations are considered as E_{VBM}. Although less accurate, this procedure is more practical and it still has been widely shown to yield reliable values for E_{VBM} [26], hence, it is the most common method used by several authors over the years, and it is the method we used in this present work, as it will be discussed later in the results session [16-21]. Fig. 1.6 shows an example of the procedure, used by McConville *et al* [27].

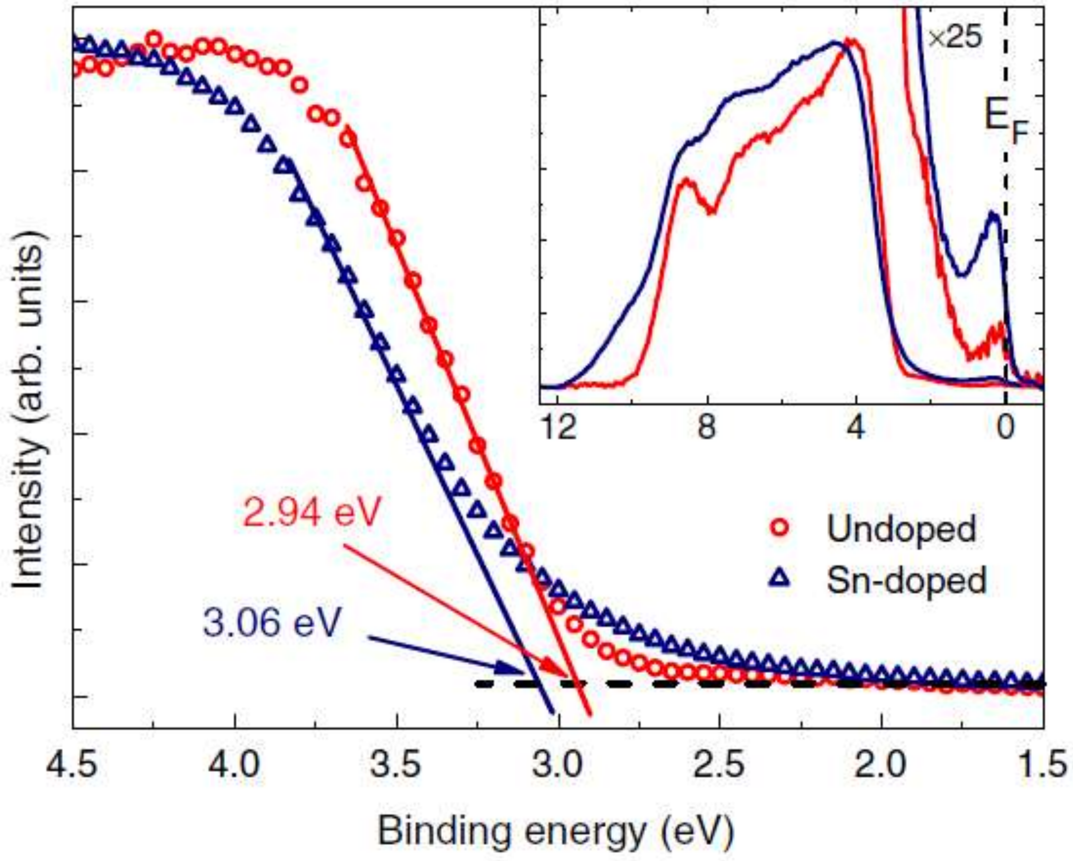

Fig. 1.6: Example of the determination of EVBM by linearly extrapolating the leading edge of the valence band emission. Extracted from ref. 27.

As mentioned, the kinetic energies (E_K) of the emitted electrons are affected by the binding energy (BE), the energy of the irradiated photon (hv), and the work function of the sample, as given by eq. 1.1. However, E_K is also affected by the work function of the detector. Since, it may be complicated to determine the work function of the material analyzed (ϕ_{Sample}), but it is rather easy to determine the work function of the detector (ϕ_{Det}), it is always useful to eliminate the influence of ϕ_{Sample} by properly grounding the sample and the electron detector to a common ground, as illustrated in Fig. 1.7 below. Note that, by using a common ground, we stablish a common value for E_f to the sample and to the equipment. The grounding procedure is also essential when comparing energy levels of different materials, since it guarantees that all the samples have the same value for E_f. Consequently, E_f may be used as a common zero energy reference to all binding energies, from all the analyzed samples, which makes it possible to analyze the BE energy spectra, according to eq. 1, substituting ϕ_{Sample} by ϕ_{Det}.

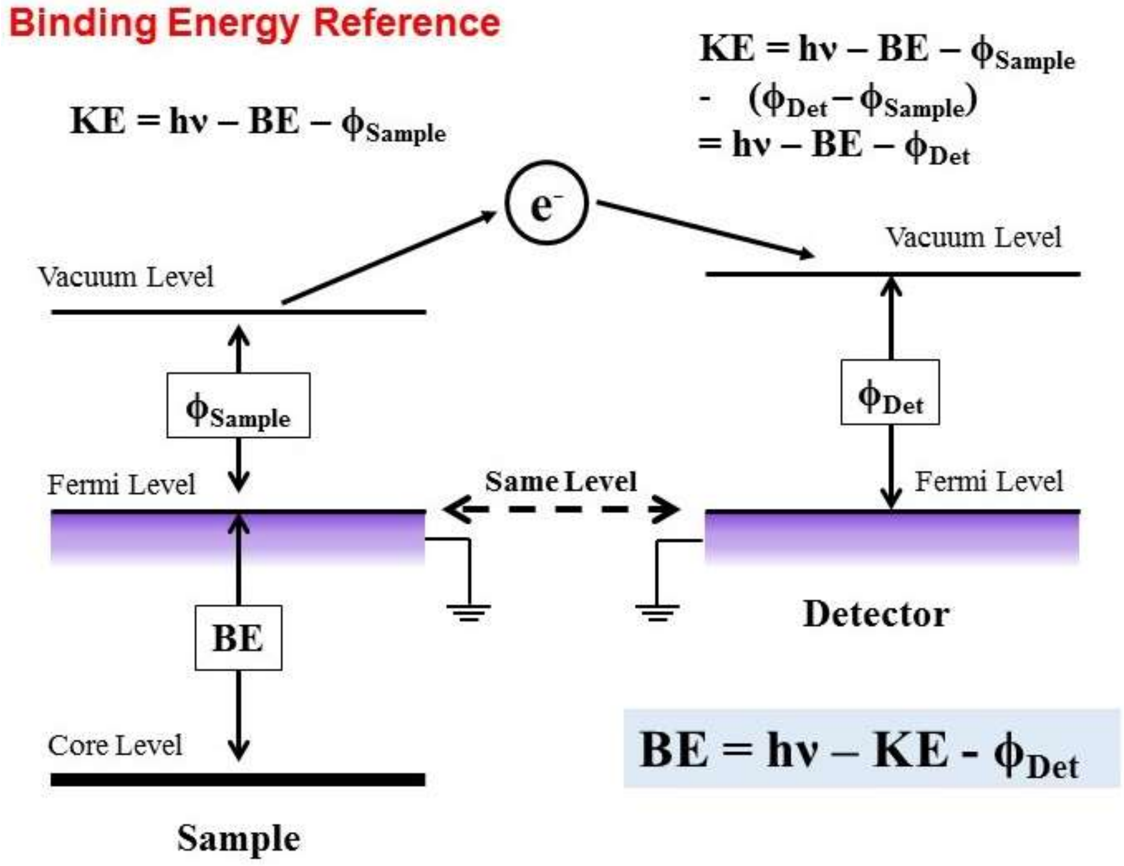

Fig. 1.7: Sketch of the grounding procedure that eliminates the influence of the work function of the sample. A similar diagram may be used to show the case of a semiconductor.

1.3 EXPERIMENTAL METHODS

MWCNTs decorated with CdS NPs (CdS/MWCNTs) were prepared using a solvothermal method, as described elsewhere [28,29]. The obtained material, after rinsing, consists of a dark green powder. Films of this dark green powder were produced by vacuum filtration [30] and transferred to gold-coated alumina plates. We also produced films of pure CdS NPs and pure MWCNTs by the same filtration method, which were also transferred to gold-coated alumina plates, to be used as reference materials for the PES measurements.

Transmission electron microscopy (TEM), selected area diffraction (SAD) and energy-dispersive spectroscopy (EDS) were carried out at the Microscopy Center of UFMG, using a FEI Tecnai G2-20 microscope with a LaB_6 filament operating at 200 kV. X-ray powder diffraction (XRD) was performed using a Rigaku Geigerflex diffractometer, using Cu K_α radiation in a $\theta - 2\theta$ geometry. A Shimadzu UV-3600 UV–Vis–NIR spectrophotometer was used to acquire diffuse reflectance spectrum of CdS/MWCNTs film in the wavelength range of 400 – 800 nm. XPS and UPS measurements were performed using a VG ESCALAB 220i-XL system with Al K_α radiation and base pressure of 1×10^{-10} mbar. XPS survey spectra were collected over the binding energy range from 1100 to 0 eV, with 60 eV pass energy, corresponding to a resolution of 1.0 eV. Individual S 2p, Cd 3d, Au4f, and C 1s peaks were measured with a pass energy of 20 eV, in this case with a resolution of 0.8 eV. The Au 4f peak position at 84.0 eV was used as references for all spectra. Every sample was grounded to the holder in order to assure they shared the same Fermi level (E_f) value, which was used as a reference level. We did not observe any charging effects. UPS spectra were taken using a homemade helium lamp at a photon energy hν = 21.2 eV (He I radiation), operating the electron analyzer at 2 eV pass energy, corresponding to a resolution of 0.05 eV. All the films were first cleaned by Ar^+ sputtering (1.5 keV) at room temperature for 30 min).

1.4 RESULTS AND DISCUSSION

The CdS NPs grew on the outer walls of the MWCNTs forming a coaxial polycrystalline coating, as shown in the SEM image of Fig. 1.8 **a**. We observed, though, that some tubes have only a few isolated NPs attached to, indicating that the coating of the MWCNTs by the CdS NPs was not completely effective. Fig. 1.8 **b** depicts the results of a statistical analysis of the size distribution of the CdS NPs attached to the MWCNTs (as arrowed in Fig. 1.8 **a**), indicating they have an average diameter of 60 nm. Figs. 1.8 **c**, **d** show the TEM images with associated SAD pattern and EDS spectrum, respectively, confirming that the NPs attached to the MWCNTs correspond to CdS. The SAD pattern also indicates that the NPs have Zinc Blende (ZB) structure, confirming the XRD results shown in Fig. 1.9. From the diffractogram of Fig. 1.9, we have estimated that the average size of the crystallites as ∼8 nm by the Scherrer method. This result indicates that each NP shown in the SEM images is composed of a few crystallites. Such finding is also confirmed by TEM and SAD results. The asymmetry at $2\theta \sim 25^o$ is related to the interwall distance of the MWCNTs [31].

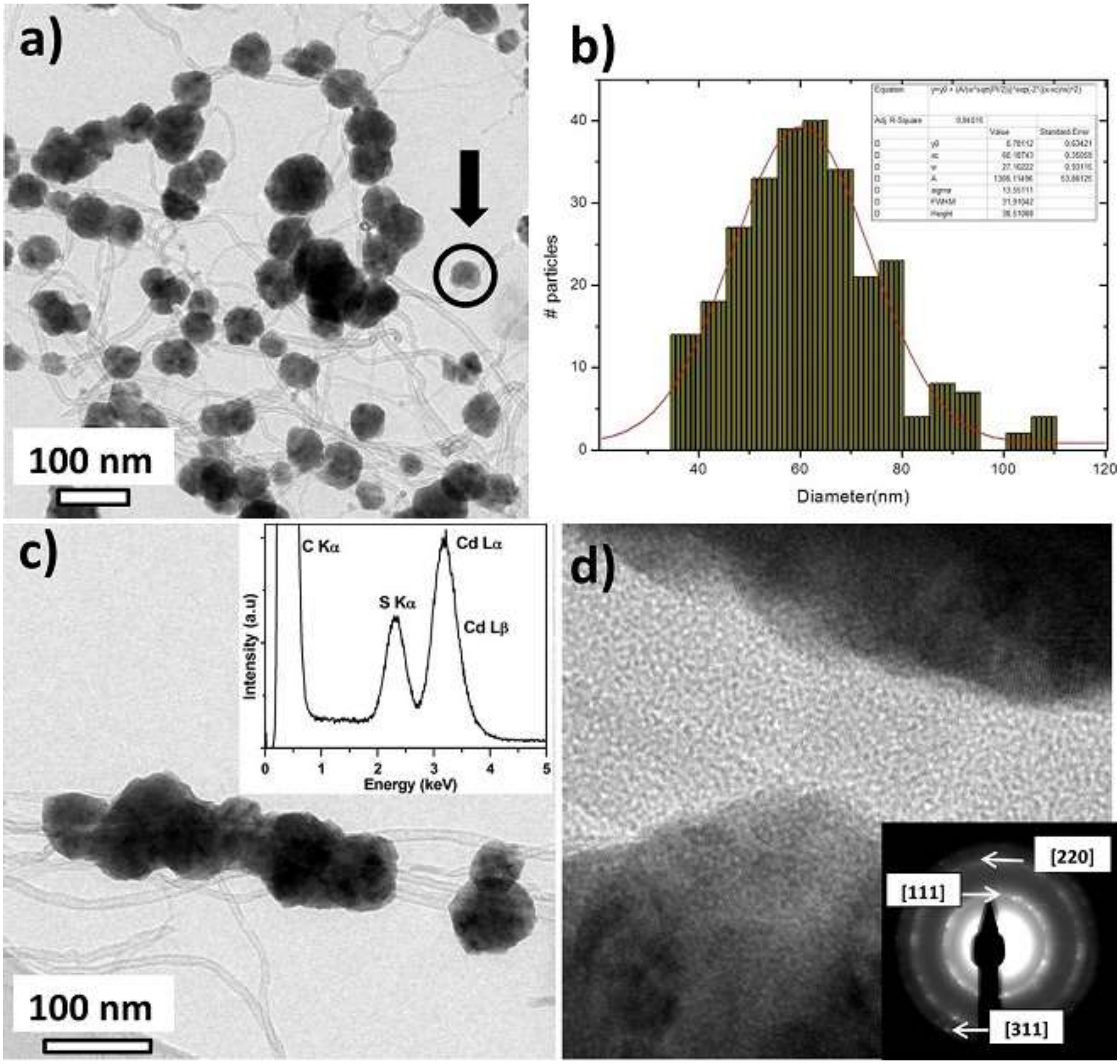

Fig. 1.8: **a)** TEM image of the polycrystalline coating of CdS decorating the MWCNTs; **b)** Size distribution of the polycrystalline coating. The average diameter is approximately 60 nm; **c)** TEM image of NPs decorating MWCNTs with EDS spectrum of the decorating NPs, confirming the presence of Cd and S; **d)** TEM image of NPs decorating MWCNTs; . The inset in **d)** shows the SAD pattern of the NPs. The indexed planes correspond to the cubic phase of CdS.

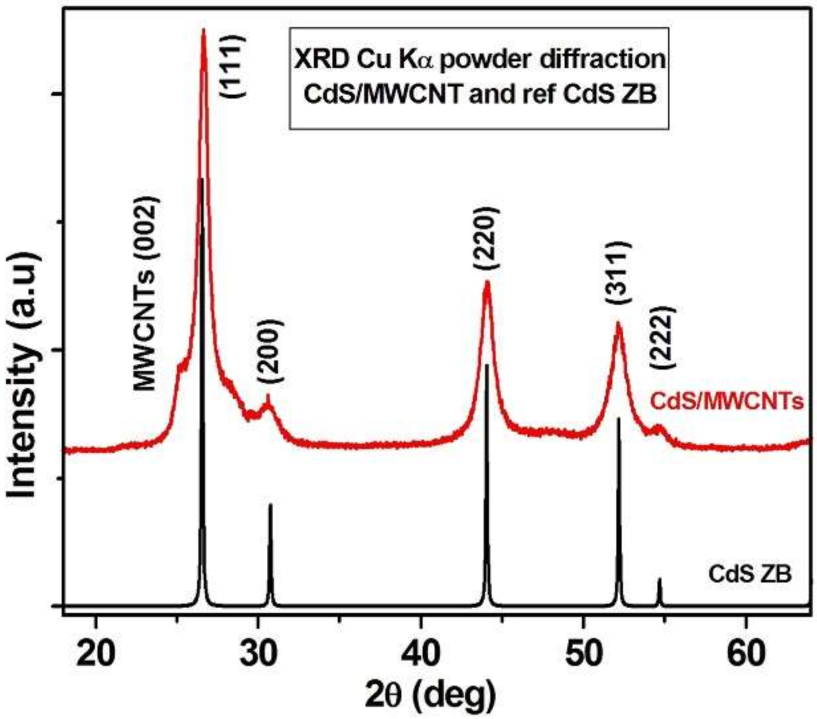

Fig. 1.9: XRD patterns of CdS/MWCNTs. The CdS zinc blende reference was taken from ICSD. The asymmetry at 2θ∼25° is related to the interwall distance of the MWCNTs.

The band gap of the decorating CdS NPs was determined by the Kubelka–Munk transformation, $f(R) = (1-R^2)/2R$, where R is the diffuse reflectance spectrum of the CdS/MWCNTs sample obtained by UV–VIS spectroscopy, as shown in Fig. 1.10. The f(R) spectrum presents a clear absorption onset that is in the expected region for CdS, however it also has a low energy contribution that may be attributed to a Drude-like contribution from the metallic MWCNTs. Due to such contribution, the common Tauc extrapolation [32] analysis becomes difficult. Thus, the value of E_g was determined as the inflection point of f(R), determined by the maximum of the first derivative of the function, shown in the bottom of Fig. 1.10 [33].

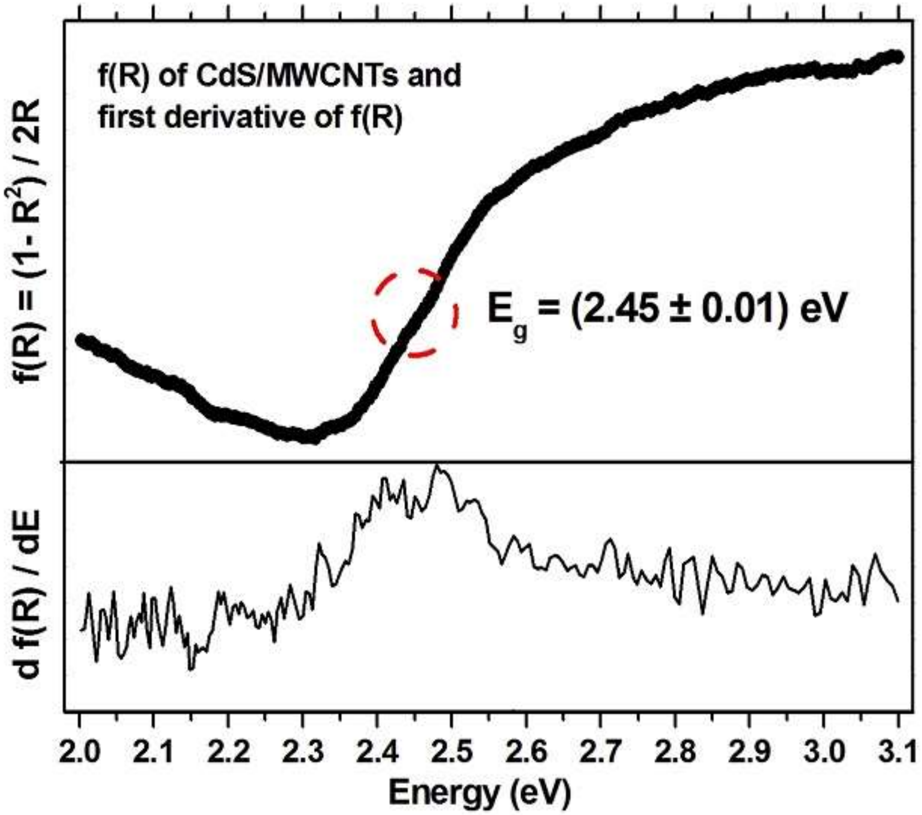

Fig. 1.10: Kubelka–Munk plot transformation of diffuse reflectance, f(R), ofCdS/MWCNTs along with its first derivative. E_g was estimated as the inflexion point, given by the maximum of f'(R) (circled area).

The XPS and UPS measurements were performed on films of CdS, functionalized MWCNTs, and CdS/MWCNTs deposited on gold-coated alumina plates as described previously. Fig. 1.11 shows an SEM image of the CdS/MWCNTs film. Part of the substrate surface was deliberately left uncoated so the gold could be used to determine E_f. The substrates were further attached and grounded to a sample holder using silver paste, as shown in Fig. 1.12. The grounding procedure is essential in order to assure that all materials under measurement have the same E_f, as mentioned.

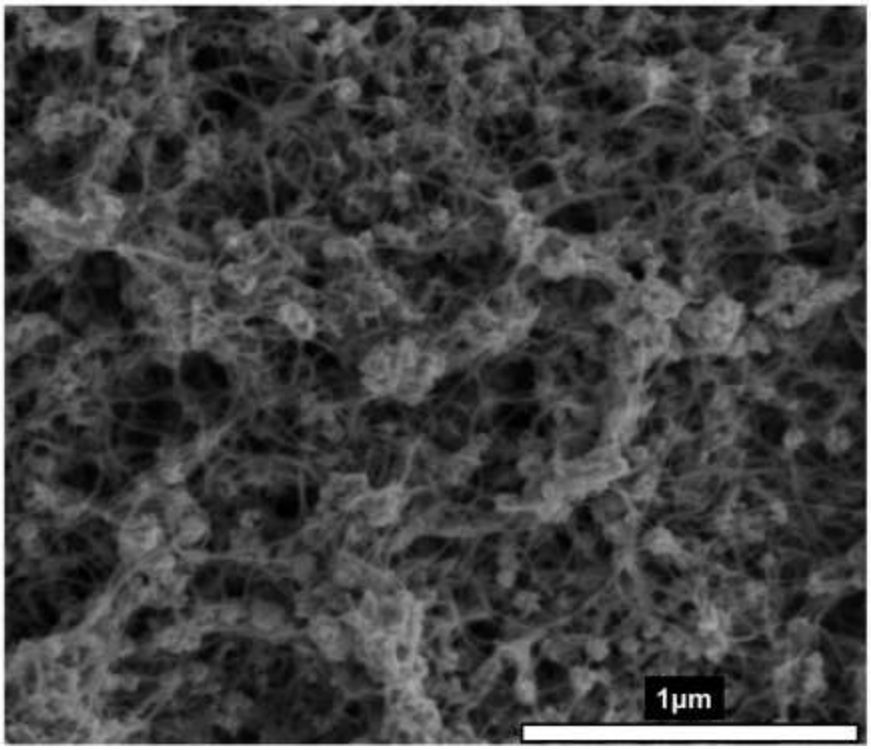

Fig. 1.11: SEM image of the CdS/MWCNT film prepared by filtration used in the PES measurements.

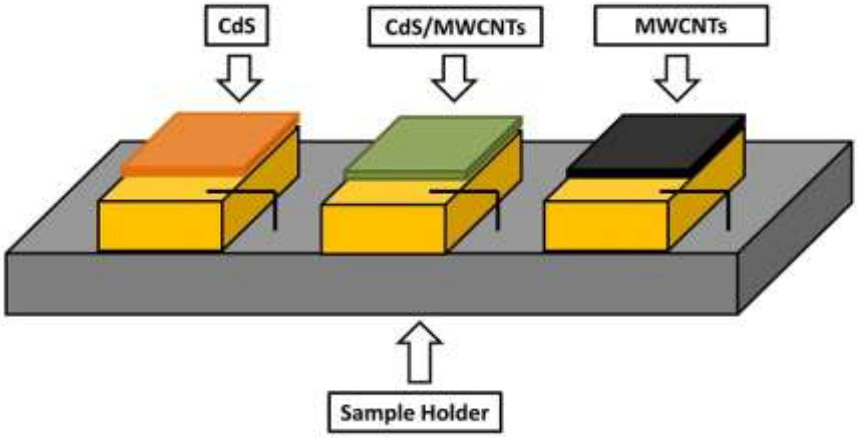

Fig. 1.12: Films deposited on gold-coated alumina plates grounded to the sample holder for XPS and UPS measurements.

To determine the band alignment in the MWCNTs/CdS interface, we used the schematic band diagram outlined in Fig. 1.13, where: E_{VBM} is the valence band maximum, E_{CBM} is the conduction band minimum, E_f is the Fermi level (used as reference for all the other energy values), E_g is the band gap, E_{CL} is the binding energy of a core level, and V_{bb} is the band bending potential. All energies indexed with "(i)" refer to the respective values at the interface. The band bending potential, V_{bb}, shifts all energy levels at the interface. This potential results from a disturbance in the charge distribution, which arises from diffusion of charges at the interface. Moreover, Poisson's equation dictates that all the energy levels must be equally shifted by V_{bb} [13]. For the XPS measurements, we approximated the values of the core levels at the interface (center of Fig. 1.13) as the ones measured on the produced CdS/MWCNTs film, whereas the core levels measured on the CdS pure sample represent the bulk values (left of Fig. 1.13). This approximation has been used in other works with interfaces and PES [14–19], and it is valid for small systems, namely the ones whose surface lies closer to the interface than the length of a typical depletion layer (region of the semiconductor material affected by V_{bb}), which is approximately 100 nm [13]. According to Fig. 1.13, the position of the conduction band minimum at the interface is given by:

$$E_{CBM}^{i} = \left(E_g - E_{VBM}\right) + \left(E_{CL}^{CdS} - E_{CL}^{CdS/MWCNTs}\right), \quad [1.5]$$

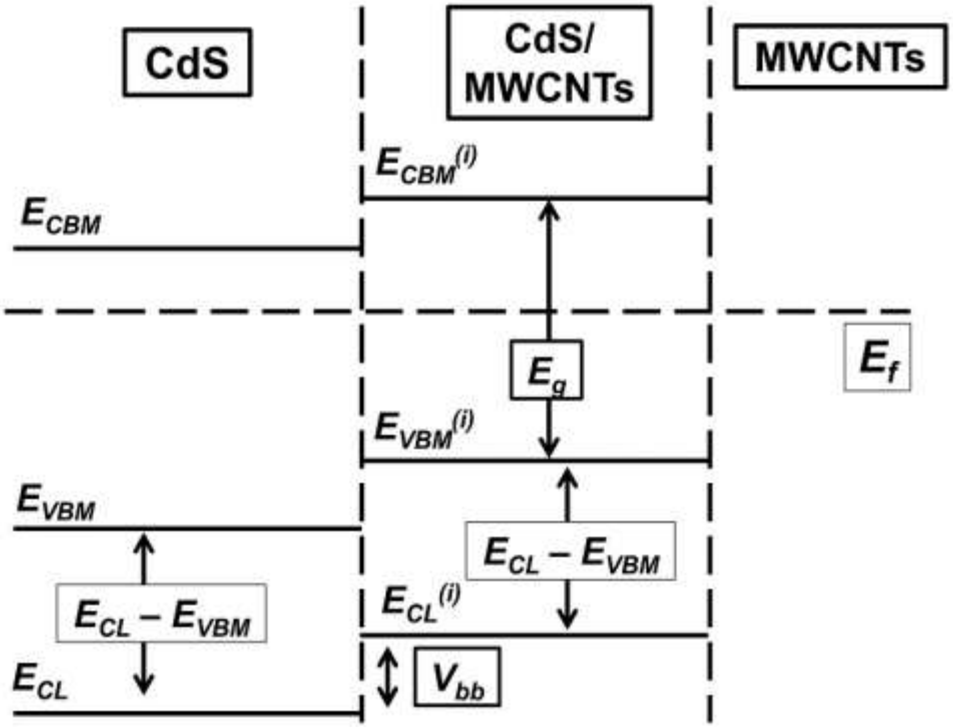

Fig. 1.13: Energy diagram near and at the interface. The E_f is constant throughout the material and it was used as a reference for all the other energy levels.

Note that depending on the sign and value of V_{bb}, we may observe the formation of either an ohmic contact ($V_{bb} < 0$) or a Schottky barrier ($V_{bb} > 0$). A negative value of V_{bb} indicates a downward band bending, whereas a positive value indicates an upward band bending (case illustrated in Fig. 1.13).

Since we are using E_f as the zero reference energy, the first step is to determine this value, which was measured in the UPS spectrum of the gold-coated substrate (top of Fig. 1.14). The inflexion point highlighted in the spectrum determines E_f [34]. The valence band spectrum of the CdS/MWCNT shows electronic signal from both materials, which makes it difficult the determination of the CdS VBM directly in that system, hence, the UPS spectrum of pure CdS is necessary. According to the literature [14–19], E_{VBM} may be determined as the intersection point between the extrapolated UPS spectrum with the respective baseline (E_{Kf}), as mentioned in section 1.2, subtracted from E_f. Therefore:

$$E_{VBM} = \left(E_f - E_{Kf}\right) = (21.0 - 18.7) = (2.3 \pm 0.1)\ eV\ , \qquad [1.6]$$

The obtained value of E_{VBM} indicates that the produced CdS has **n**-type behavior, due to the proximity of E_f to the conduction band (see Fig. 1.5). The result is in good agreement to the literature, as CdS synthesized by chemical routes commonly presents **n**-type behavior [35].

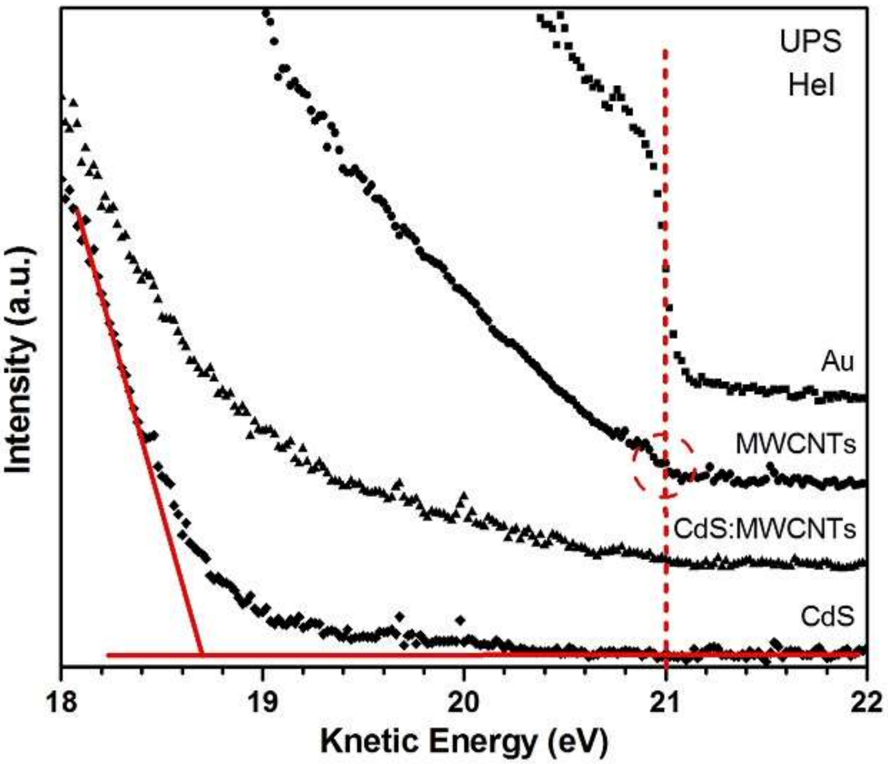

Fig. 1.14: UPS spectra of the exposed gold-coated substrate, the CdS/MWCNTs film, the CdS film, and the MWCNT film. The dashed line marks the value of E_f = 21.0 eV and the intersection between the extrapolated lines represents E_{Kf} = 18.7 eV. The inflexion point (circled) on the UPS spectrum of the MWCNT film confirms the metallic character of the material

The value E_{Kf} in the UPS spectrum represents the kinetic energy of the electron emitted from the valence band maximum. Also shown in Fig. 1.14 is the UPS spectrum of the MWCNTs film, which confirms its metallic character due to the presence of an inflexion point at E_f, similar to the observed in the Au spectrum. Using the band gap value for the CdS NPs obtained from the optical measurements, $E_g = (2.45 \pm 0.01)$ eV, we obtained a value of 0.15 eV for E_{CBM}, *i.e.* the distance of the bottom of the conduction band to E_f. The proximity of E_f to the conduction band indicates an **n**-type character of the CdS NPs, which is typical for CdS materials prepared by chemical routes [36].

The last term in eq. 1.5 was obtained directly by comparing XPS measurements of Cd 3d and S 2p core levels of pure CdS and the hybrid CdS/MWCNTs films, shown in Fig. 1.15. Both core levels showed a binding energy shift of (−0.20 ± 0.01) eV. The observed shift in binding energy, according to Fig. 1.13, represents the value of V_{bb}. Moreover, the negative value of the shift indicates a downward band bending, which may lead to the formation of an ohmic contact. All peaks were adjusted by a combination of Gaussian and Lorentzian line shapes and a Shirley background [13]. Charging effects were not observed in the XPS measurements, as confirmed by the reproducibility of the position of the Au 4f peak (84 eV) in all spectra. The absence of charging effects indicates the grounding procedure was successful. Substituting the obtained values of E_{VBM}, E_g, and V_{bb} into eq. 1.5, we determined the position of the conduction band minimum at the CdS/MWCNTs interface:

$$E^{i}_{CBM} = (2.45 - 2.3) + (-0.2) = (0.0 \pm 0.1)eV, \qquad [1.7]$$

Therefore, no potential barrier was formed between both materials, meaning that the metallic MWCNTs formed an ohmic contact with the CdS NPs. Such result corroborates the idea of using MWCNTs as charge collectors for CdS nanostructured films.

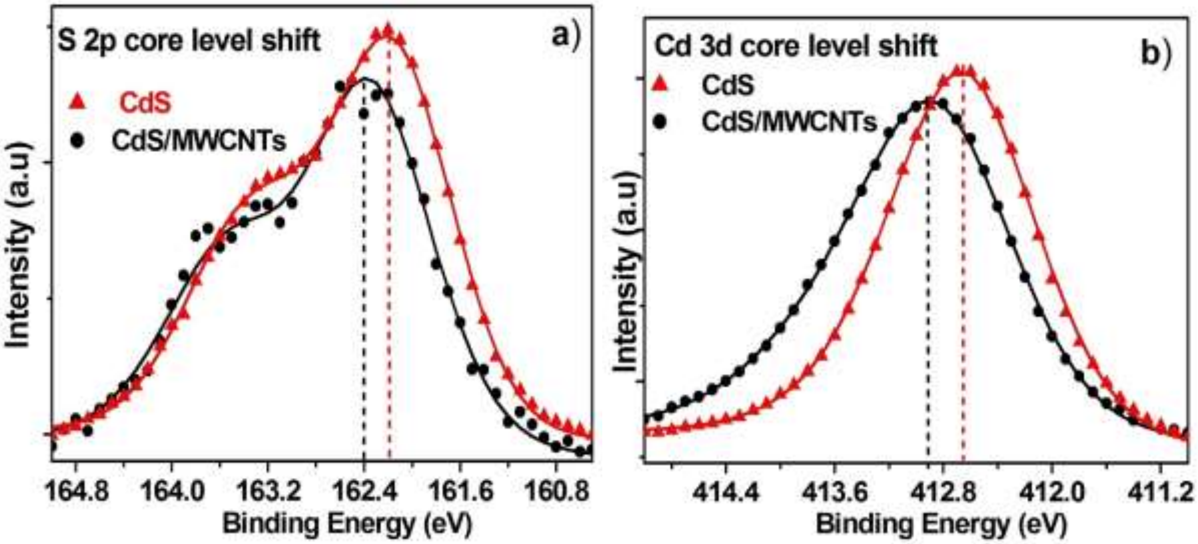

Fig. 1.15: Core level shifts of (a) S 2p and (b) Cd 3d. Symbols and the lines represent the experimental data and the adjust, respectively.

Fig. 1.16 illustrates the energy diagram near and at the interface, with the obtained values, whereas Fig. 1. 17 shows the effect of the band bending at the interface of both materials.

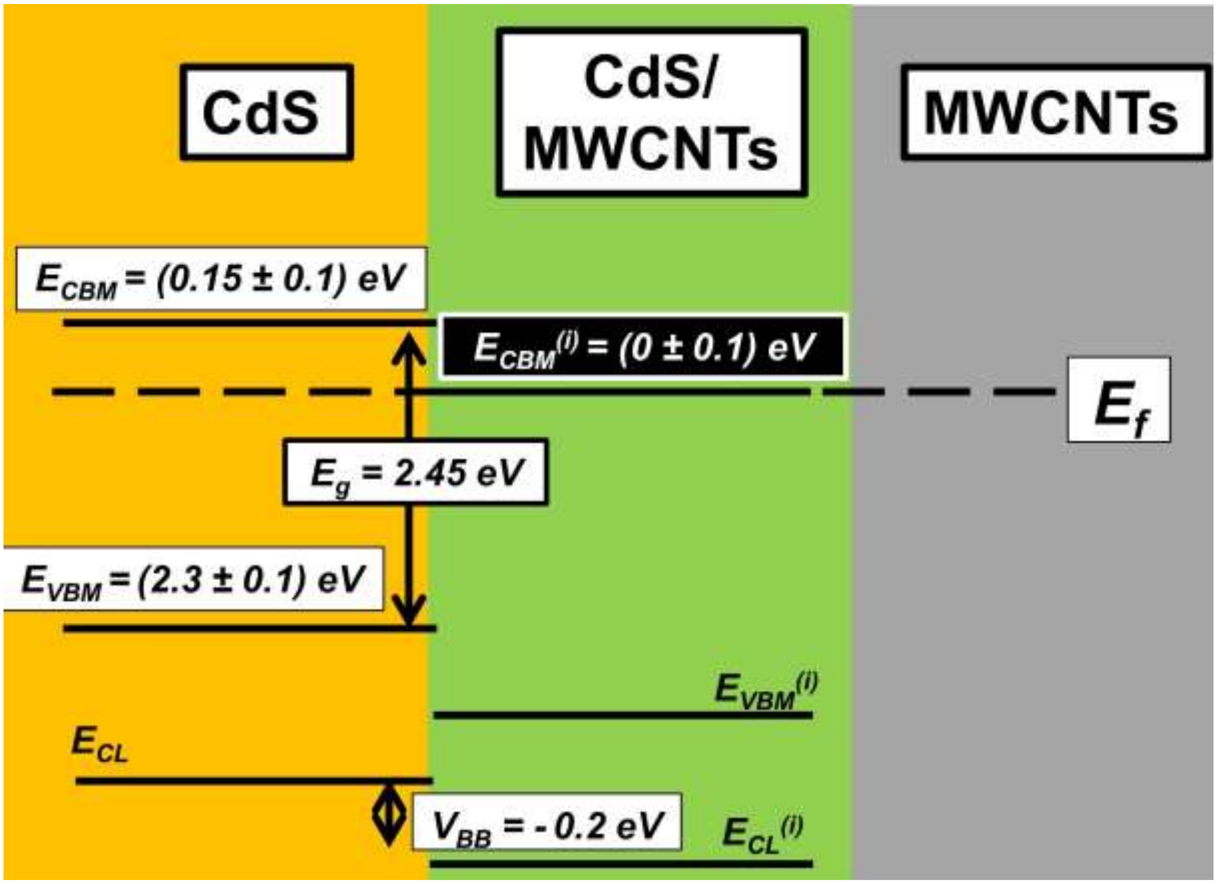

Fig. 1.16: Band diagram near and at the interface of CdS and MWCNTs with the values of the energies used in eq. 1. As observed, the bands bended downward, forming an ohmic contact.

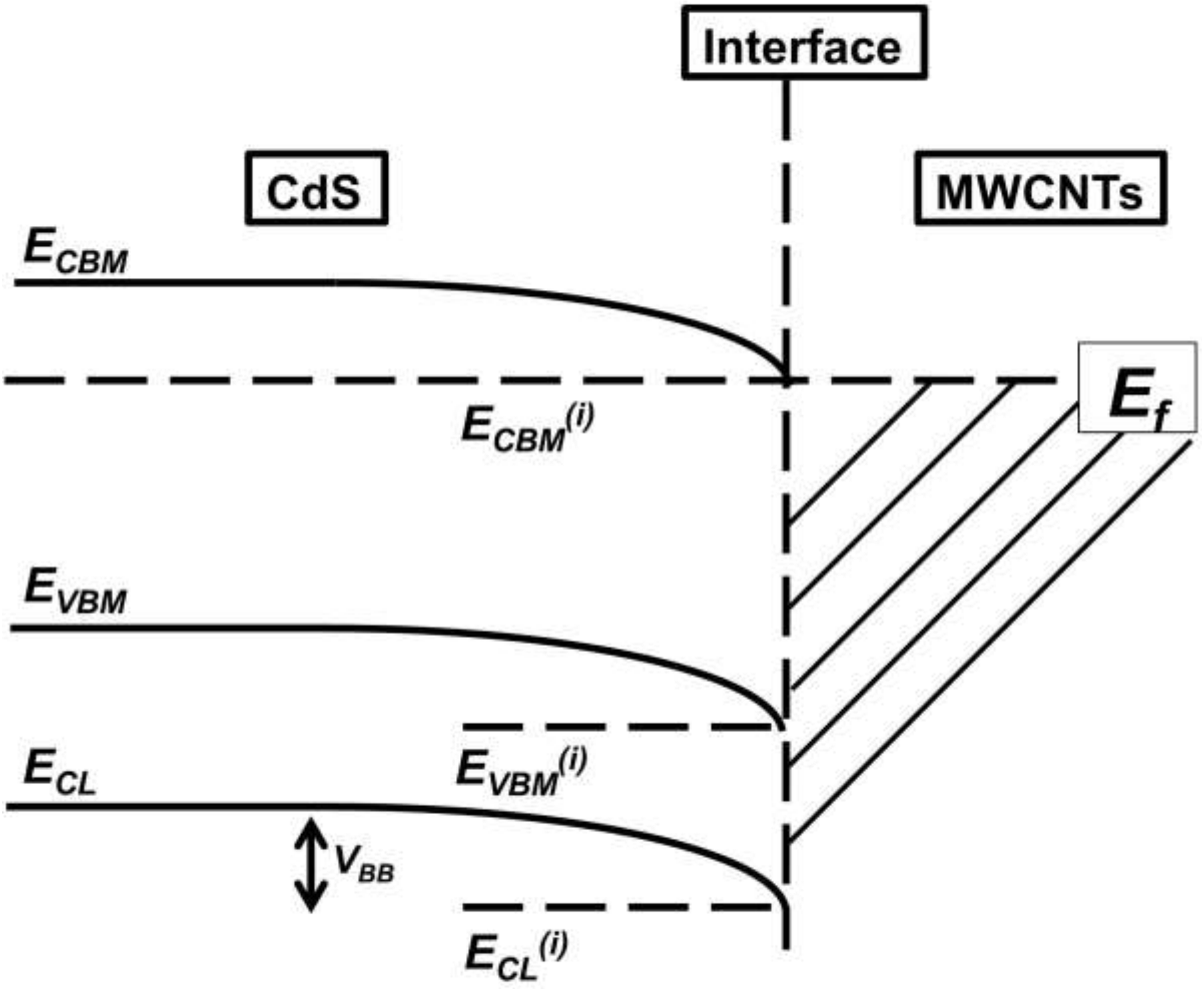

Fig. 1.17: Energy levels of CdS with the band bending at the CdS/MWCNTs interface.

The value of E_{CBM} at the interface represents an average of the actual band alignment, due to both (i) the three-dimensionality of the system and (ii) the fact that the MWCNTs are not fully decorated. (i) Unlike what happens in interfacial thin films, with a single planar interface, the CdS/MWCNTs have a 3D multiple set of interfaces, similar to a bulk heterojunction in organic solar cells [37], ideally depicted in Fig. 1.18 as a network of CNTs immersed in a CdS matrix. During XPS measurements, in such 3D array of interfaces, electrons are photoemitted from different distances from the actual interface, thereby resulting in distinct energy shifts. The binding energy values observed in Fig. 1.15 are, then, an average from all the electrons collected from the different positions along the depletion layer. (ii) In our samples, the decoration of the MWCNTs is not homogeneous (Fig. 1.9). We observed a wide size distribution of the NPs and some MWCNTs are not even decorated. The first aspect contributes to (i), as illustrated by Fig. 1.19, whereas the second does not affect the result. Partially decorated MWCNTs, as well as not decorated ones, only affect the intensity of the binding energies in the XPS spectrum of the CdS/MWCNTs film, but not the position of the peaks. The lack of NPs in some MWCNTs decreases the CdS core level emissions, which could lead to less, but not critically low, resolution of the peaks, while increases the carbon core level emissions.

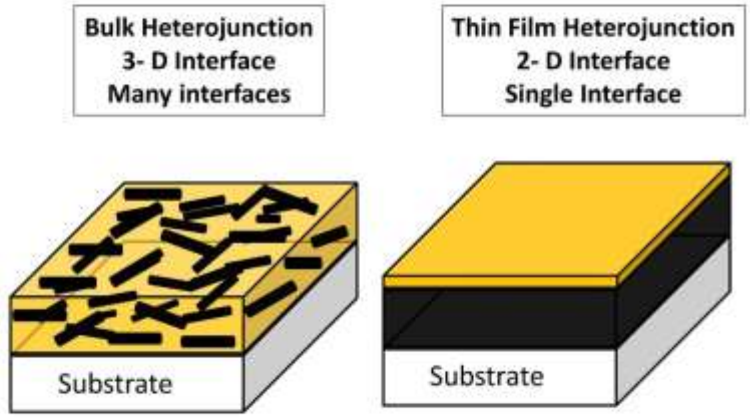

Fig. 1.18: Two types of interfaces: bulk heterojunction (left) and the most common planar heterojunction (right). The CdS/MWCNTs BH is ideally represented here by a network of CNTs immersed in a CdS matrix. In our samples, though, some MWCNTs are not fully decorated or even slightly decorated at all by CdS NPs.

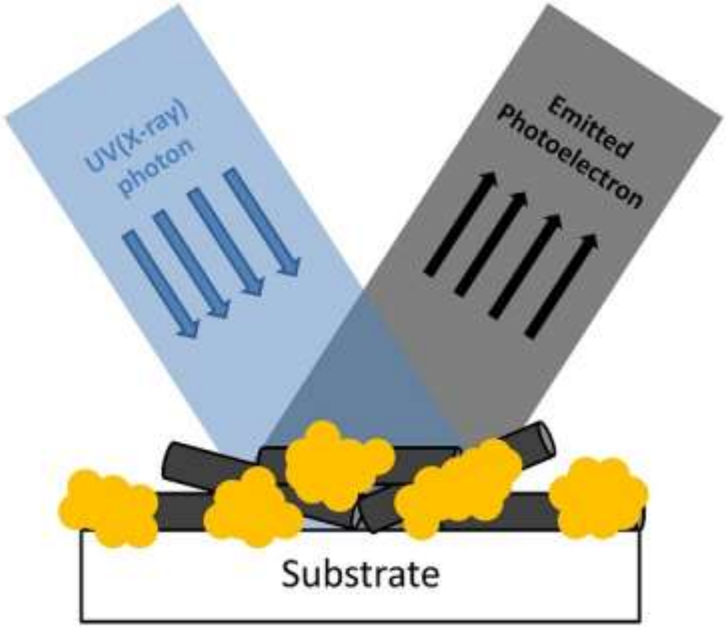

Fig. 1.19: Sketch of the PES experiment on the produced CdS-MWCNT film, illustrating the effect of the differently decorated MWCNTs.

The obtained result, $E_{CBM}^{i} = (0.0 \pm 0.1)eV$ indicates the formation of an ohmic contact between the CdS NPs and the metallic MWCNTs. The formation of ohmic contacts between carbon materials and CdS has already been observed by Smertenko *et al.* in a CdS/carbon fiber interface [38]. The observed ohmic contact may also explain the emission quenching of semiconductor NPs when anchored in CNTs as observed by some groups [39,40], as well as the improvement on the performance of many devices based on metal oxides and CNTs hybrid materials, as presented by Zhang et al. [41]. The authors explain both the quenching emission phenomenon and the enhanced device performances as direct results of charge transfer from the NPs to the CNTs. Such transport mechanism is better explained if the NPs and the MWCNTs form an ohmic contact at the interface, arising from a good interfacial combination, as observed in our CdS/MWCNTs films. Moreover, Linqin Jiang and Lian Gao observed an enhanced photocatalytic activity of ZnO-coated MWCNTs, when compared to a simple mechanical mixture of ZnO and MWCNTs, thus showing that growing NPS directly attached to CNTs in hybrid materials, favors a good interfacial combination [42]. Finally, the band alignment depicted in Figs. 1.16 and 1.17 reinforces the idea to use MWCNTs as a charge collector material in CdS-based devices.

In the following chapters we present the study regarding the growth of iron pyrite (FeS_2) films, which has been published in Thin Solid Films.

References

---

1 S. Iijima., Nature **354** (1991) 56
2 C.N.R. Rao, B.C. Satishkumar, A. Govindaraj, M. Nath, Chem. Phys. Chem. **2** (2001) 78
3 P. Collins, K. Bradley, M. Ishigami, A. Zettl, Science **287** (2000) 1801
4 S. Fan, M.G. Chapline, N.R. Franklin, T.W. Tombler, A.M. Cassel, H. Dai, Science **283** (1999) 512
5 S. Banerjee, M.G.C. Kahn, S.S. Wong, Chem. Eur. J. **9** (2003) 1898
6 A.P. Alivisatos, Science **271** (1996) 933
7 P.V. Kamat, Nanotoday **1** (2006) 20
8 J.H. Shi, Y.J. Qin, W. Wu, A.L. Li, Z.X. Guo, D.B. Zhu, Carbon **42** (2004) 455
9 S. Ravindran, S. Chaudhary, B. Colburn, M. Ozkan, C.S. Ozkan, Nano Lett. **3** (2003) 447
10 S. Ravindran, S. Chaudhary, B. Colburn, M. Ozkan, C.S. Ozkan, Nano Lett. **3** (2003) 447
11 J.M. Haremza, M.A. Hahn, T.D. Krauss, S. Chen, J. Calcines, Nano Lett. **2** (2002) 1253
12 S. Banerjee, S.S. Wong, Nano Lett. **2** (2002)195
13 W.Q. Han, A. Zettl, Nano Lett. **3** (2003) 681
14 L. Sheeney-Haj-Khia, B. Basnar, I. Willner, Angew. Chem. Int. Ed. **44** (2005) 78
15 E.A. Kraut, R.W. Grant, J.R. Waldrop, S.P. Kowalczyk, Phys. Rev. Lett. **44** (1980) 1620
16 A. Zakutayev, J. Tate, H.A.S. Platt, D.A. Keszler, A. Barati, A. Klein, W. Jaegermann, Appl. Phys. Lett. **96** (2010) 162110
17 M. Akazawa, B. Gao, T. Hashizume, M. Hiroki, S. Yamahata, N. Shigekawa, J. Appl. Phys. **109** (2011) 013703
18 K. Shi, D.B. Li, H.P. Song, Y. Guo, J. Wang, X.Q. Xu, .J.M. Liu, A.L. Yang, H.Y. Wei, B. Zhang, S.Y. Yang, X.L. Liu, Q.S. Zhu, Z.G. Wang, Nanoscale Res. Lett. **6** (2011) 50
19 V. Krishnakumar, K. Ramamurthi, A. Klein, W. Jaegermann, Thin Solid Films **517** (2009) 2558
20 M.R. Rajesh Menon, A. Mancini, C. Sudha Kartha, K.P. Vijayakumar, A. Santoni, Thin Solid Films **520** (2012) 5856
21 D.A.R. Barkhouse, D. Aaron, R. Haight, N. Sakai, H. Hiroi, H. Sugimoto, D.B. Mitzi, Appl. Phys. Lett. **100** (2012) 193904
22 H. Hertz, Ann. Physik **31** (1887) 983
23 A. Einstein, Ann. Physik **17** (1905) 132
24 S. Hüfner, Photoelectron Spectroscopy: Principles and Applications: Berlim, Germany, Springer (2010)
25 J.R. Chelikowsky, M.L. Cohen, Phys. Rev. B **14** (1976) 556
26 S.A. Chambers, T. Droubay, T.C. Kaspar, M. Gutowski, J. Vac. Sci. Technol. B **22** (2004) 2205
27 P.D.C. King, T.D. Veal, D.J. Payne, A. Bourlange, R.G. Egdell, C.F. McConville, Phys. Rev. Lett. **101** (2008) 116808
28 M.F.O. Silva, Masters Dissertation: Decoração de Nanotubos de Carbono de Paredes Múltiplas com Nanocristais Semicondutores Visando Aplicações Optoeletrônicas, Belo Horizonte, Brasil (2011)
29 M.F.O. Silva, W.N. Rodrigues, A.S. Ferlauto, L.O. Ladeira, C.B. Pinheiro, D.R. Miquita, MRS Proceedings, **1396** (2011) 1396
30 Z. Wu, Z. Chen, X. Du, J.M. Logan, J. Sippel, M. Nikolou, K. Kamaras, J.R. Reynolds, D.B. Tanner, A.F. Hebard, A.G. Rinzler, Science **305** (2004) 1273
31 M. Terrones, W.K. Hsu, A. Schilder, H. Terrones, N. Grobert, J.P.Hare, Y.Q. Zhu, M. Schwoerer, K. Prassides, H.W. Kroto, D.R.M. Walton, Appl. Phys. A **66** (1998) 307
32 J. Tauc, Mat. Res. Bull. **3** (1968) 37
33 B. Gilbert, C. Frandsen, E.R. Maxey, D.M. Sherman, Phys. Rev. B **79** (2009) 035108

---

34 N.W Ashcroft and N.D Mermin, Solid State Physics, Orlando: Harcourt College Publishers (1976)

35 M.F.O. Silva, R.M. Paniago, D.R. Miquita, C.B. Pinheiro, L.O. Ladeira, A.S. Ferlauto, W.N. Rodrigues, Appl. Surf. Science 321 (2014) 283

36 G. Hodes: Chemical Solution Deposition of Semiconductor Films, New York: Marcel Dekker (2003)

37 G. Yu, J. Gao, J.C. Hummelen, F. Wudi, A.J. Heeger, Science **270** (1995) 1789

38 P.S. Smertenko, D.A. Grynko, N.M. Osipyonok, O.P. Dimitriev, A.A. Pud, Phys. Status Solidi A **210** (2013) 1851

39 F. Vietmeyer, B. Seger, P.V. Kamat, Adv. Mater. **19** (2007) 2935

40 L.C. Jiang, W.D Zhang, Y.X. Yu, J. Wang, Electrochem. Comm. **13** (2011) 627

41 W.D. Zhang, B. Xu, L.C. Jiang, J. Mater. Chem. **20** (2010) 6383

42 L. Jiang, L. Gao, Mater. Chem. Phys. **91** (2005) 313

2 Pyrite: Introduction

In this chapter, we present the motivation for studying iron pyrite (FeS_2). We show the advantages of this semiconductor in the context of photovoltaic devices, as well as the state of the art in the synthesis of the material, listing and briefly describing several of the techniques used. Then, we show some examples and advances in device construction and performance, unveiling some characteristics and problems discovered by authors in the past years.

2.1 POTENTIAL MATERIAL FOR PHOTOVOLTAICS

In 1984, Tributsch *et al* first reported the possibility to use iron disulfide (FeS_2) as semiconducting material in solar cells, by showing high quantum efficiencies for photocurrent generation (33 %), and reasonable open circuit voltages, V_{OC}, (0.2 V) [1]. Since then, many authors have thoroughly studied iron pyrite (FeS_2) due to its potential use as absorber material in solar cells [1,2,3,4,5,6,7]. The fact that FeS_2 combines excellent physical properties, such as high optical absorption coefficient ($\alpha \sim 10^5$ cm^{-1}) with environmental friendly characteristics – low toxicity and abundance of its constituent materials, Fe and S, – makes it a suitable material to be used in photovoltaic devices. Recently, Allivisatos *et al* demonstrated this favorable scenario by comparing the theoretical performances of several different semiconductors as absorber materials in ideal solar cells, *i.*e, with minimum energy loss [3]. Along with the potential efficiencies for power conversion, the authors also investigated the cost of the raw material extraction of each semiconductor, illustrated in Fig. 2.1. In the study, as evidenced in Fig. 2.2, FeS_2 excelled in both aspects, arising as the material with the best potential performance to convert solar energy in electricity as well as the least expensive to build a device, surpassing the other semiconductors, including a-Si.

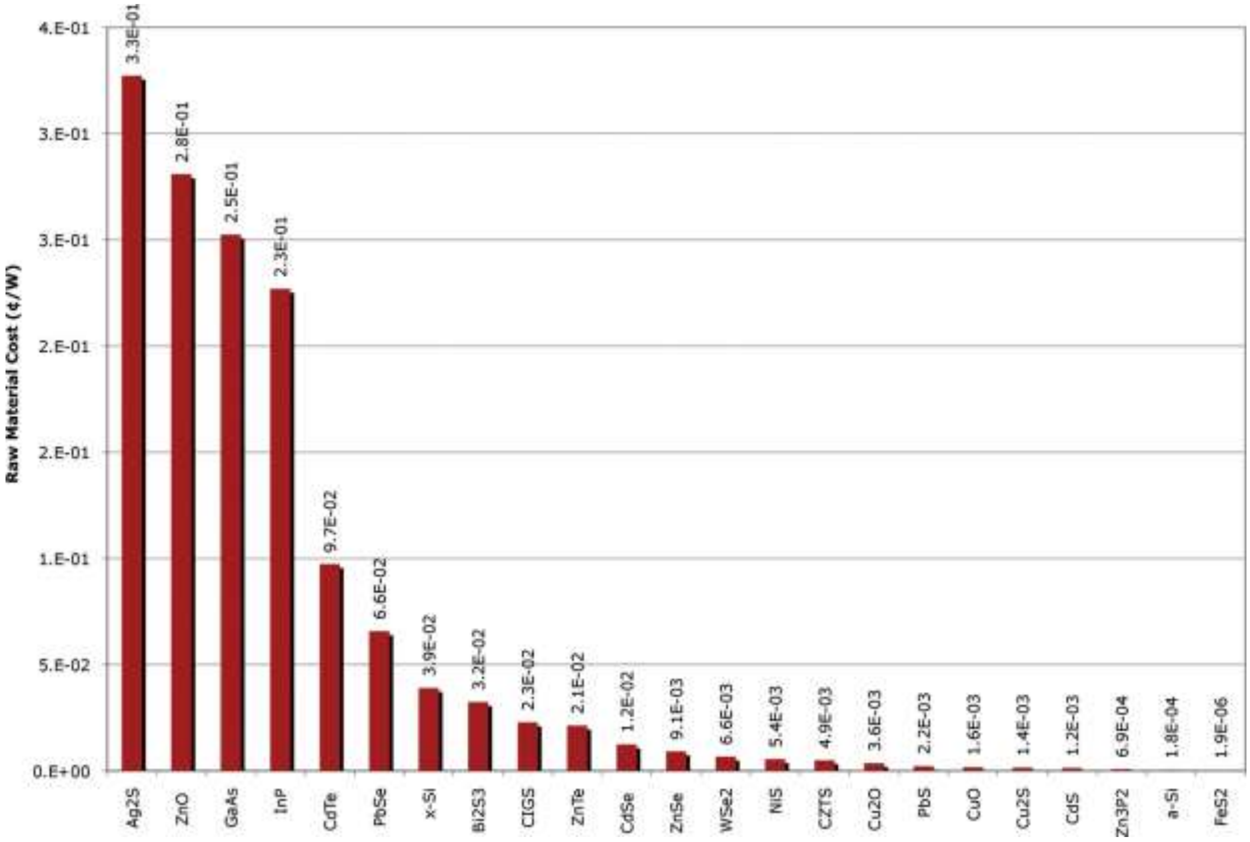

Fig. 2.1: Raw material cost evaluated by Allisivsatos *et al* of different semiconductors, for the production of devices.

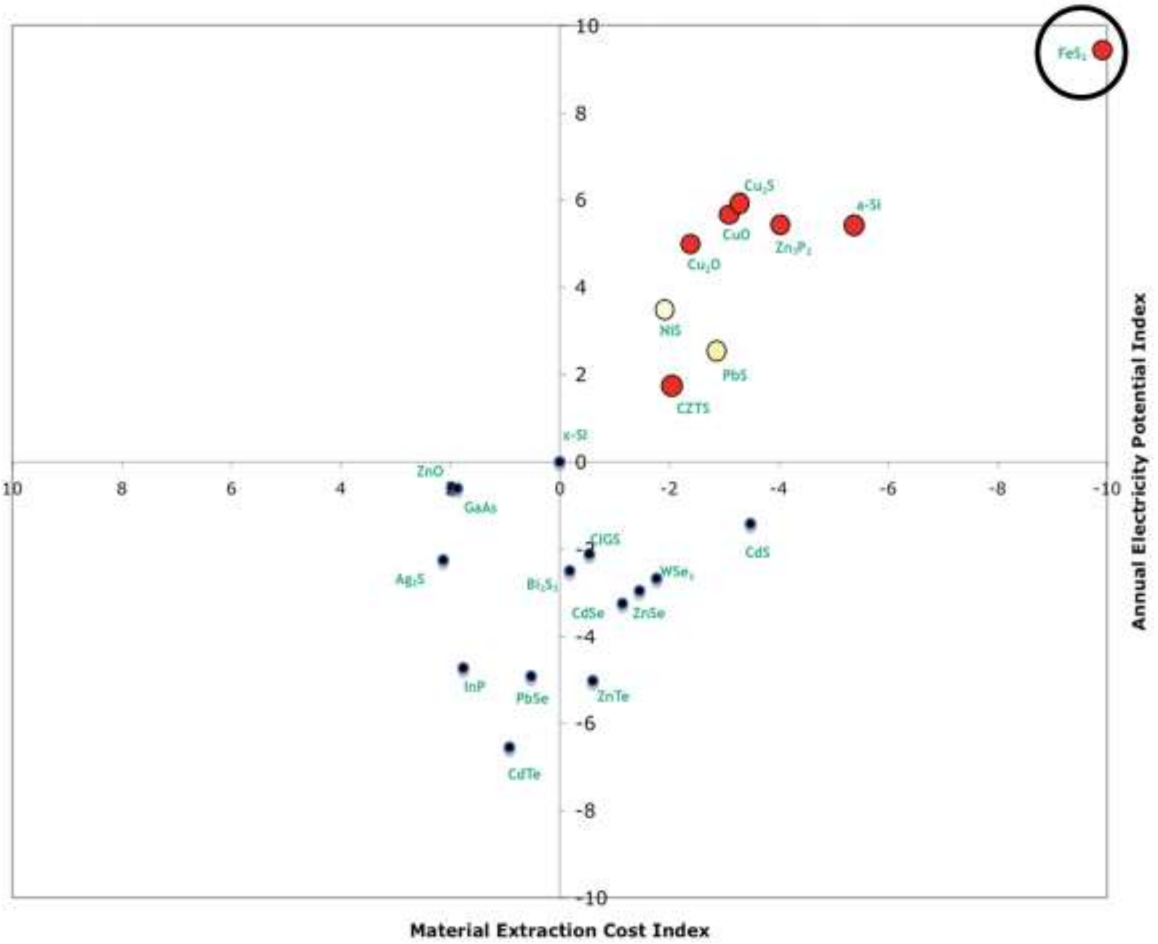

Fig. 2.2: Results of the model proposed by Allivisatos *et al* to compare the cost and potential efficiency of different semiconductor as absorber materials in ideal solar cells. FeS_2 (circled) surpassed every other material.

Despite the overall potential of FeS_2, researchers still struggle to extract considerable power conversion efficiencies from FeS_2 based devices [6, 8]. The reasons for the low efficiencies observed so far in pyrite based devices are mainly related to the low open circuit voltage (V_{OC}) values obtained, and they will be further discussed in section 3 of this chapter. First, in the following section we will present some properties of the material.

2.2 CRYSTAL STRUCTURE, POLYMORPHISM, AND DECOMPOSITION

Iron disulfide (FeS_2) commonly occurs in two polymorph phases both in nature and under laboratory conditions. The cubic pyrite has a rock salt like structure (a = 5.417 Å) with Fe atoms occupying the cation (Na) site and the S_2 dumbbells occupying the anion (Cl) sites. As depicted in Fig. 2.3, Fe atoms are six coordinated with 6 S atoms forming a distorted octahedron, whereas the S atoms are 4 coordinated with 3 other S atoms and one Fe atom, forming a tetrahedral structure [9]. Marcasite has a structure similar to pyrite, with the Fe atoms still located in the center of a distorted octahedron formed by 6 S atoms, and S centered in a tetrahedron composed of 3 S atoms and one Fe. However, in marcasite, the S_2 dumbbells are oriented and linked differently, resulting in an orthorhombic structure (a = 4.436 Å, b = 5.414 Å, c = 3.381 Å). In addition, in marcasite, the octahedrons share a sulfur atom, which does not occur in pyrite [9].

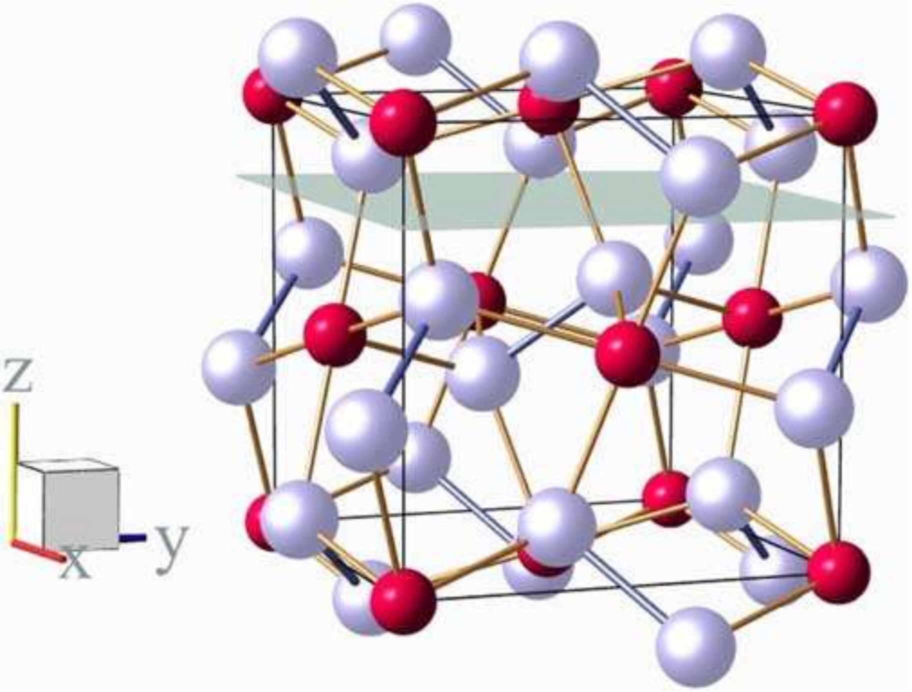

Fig. 2.3: Pyrite crystal structure with Fe and S atoms represented by red and white spheres, respectively [10].

Likewise the similarity in the crystal structure of both FeS_2 phases, the thermodynamic properties of these material differ only slightly, as observed by F. Grønvold and E.F. Westrum Jr., who analyzed the heat capacity and the Gibbs free energy of formation of both materials and observed that marcasite presents slightly higher values over a wide range of temperature (5 to 700 K) [11]. As an example, Fig. 2.4 shows the values of the heat capacity for both FeS_2 polymorphs at different temperatures. This result (that pyrite has lower values of heat capacity and Gibbs free energy of formation and, hence, is more stable than marcasite) explains partially why the cubic phase is often more present in both natural and synthetic FeS_2. Furthermore, marcasite undergoes an exothermic irreversible transformation reaction to pyrite at temperatures above 700 K, which means, as stated by the authors in ref 9, that marcasite is metastable with regard to pyrite, and its formation and persistence are, then, related to kinetic factors.

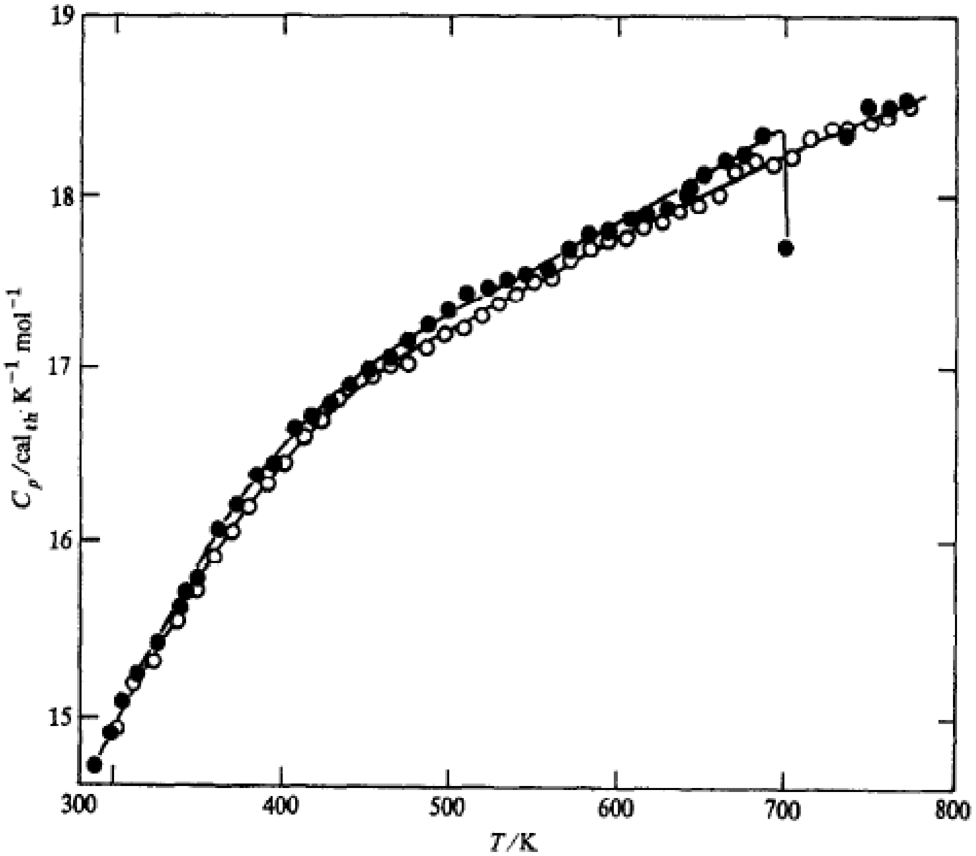

Fig. 2.4: Values of the heat capacity of pyrite (white circles) and marcasite (black circles). Note that marcasite presents values slightly higher than pyrite over the whole temperature range [11].

The works of M.E. Fleet regarding the structural aspects of the marcasite to pyrite transformation, and of A.R. Lennie and D.J. Vaughan, who investigated the kinetics of the reaction, support the idea of Grønvold and Westrum [9,12]. In the first case, XRD measurements were performed *in-situ* during the transformation and minimum structural reorganization was observed, suggesting negligible diffusion of elements. In the second work, the authors recorded the evolution of the transformation reaction by means of infrared spectroscopy, and observed that the parameters that fitted best the used kinetics model was in accordance with a nucleation and growth at grain edges process, rather than to a diffusion process. More details about the marcasite-pyrite reaction will be discussed in chapter 5.

When heated, pyrite may decompose into different materials, depending on the environment conditions. If heated in an inert atmosphere, pyrite releases sulfur vapor and transforms into the iron rich sulfide, pyrrhotite, described as FeS_x, with x varying from the stoichiometric troilite (FeS) to values close to but less than 2 [13,14]. In fact, many phases with different concentrations of sulfur have been reported for pyrrhotite, and the phase formed due to the decomposition of pyrite strongly depend on the sulfur fugacity – $f(S_2)$ – and temperature of the process [12]. On the other hand, if pyrite is heated in oxygen-containing atmospheres, it oxidizes into hematite (Fe_2O_3) or magnetite (Fe_3O_4), depending on the oxygen concentration, particle size of the precursor pyrite material, temperature and other parameters. Kim Dam-Johansen *et al*. presented a review on both decomposition reactions, describing the results for several different conditions, but we will focus only on the first reaction, as it is more relevant during the synthesis of our pyrite films. The decomposition reaction of FeS_2 in inert atmosphere is endothermic and reversible, and may be represented by the simple equation:

$$FeS_2(s) \leftrightarrow FeS_x(s) + (1 - 0.5x)S_2(g), \qquad [2.1]$$

P. Toulmin and P.B Barton Jr studied thoroughly the reaction described above at temperatures between 325 °C and 743 °C. The authors correlated the pyrrhotite composition, sulfur fugacity – f (S_2) – and temperature. The equation obtained is illustrated in the graph depicted in Fig. 2.5 below, which shows lines corresponding to different pyrrhotite compositions below the Py/Po – here, Py and Po stands for pyrite and pyrrhotite, respectively – line, which defines the equilibrium condition of eq. 2.1. It is important to note that if $f(S_2)$ continuously drops at a fixed temperature, pyrrhotite will also continuously release sulfur vapor until it further decomposes, firstly to the stoichiometric troilite and lastly to elemental iron. The outgoing diffusion of the formed sulfur gas across the primary pyrrhotite layer (produced by the reaction of pyrite in eq. 2.1), may result in a sulfur gradient across the pyrrhotite layer [13]. Moreover, the primary pyrrhotite layer may further decompose because of the deviation of sulfur pressure across the FeS_x layer, even before pyrite is completely decomposed [13]. It is also important to note that, at temperatures higher than or equal to 700 ^oC, the equilibrium $f(S_2)$ approaches values close to 1 atm, and at T ~ 750 ^oC, pyrite presents an incongruent melting point, melting irreversibly to form pyrrhotite and a sulfur rich liquid.

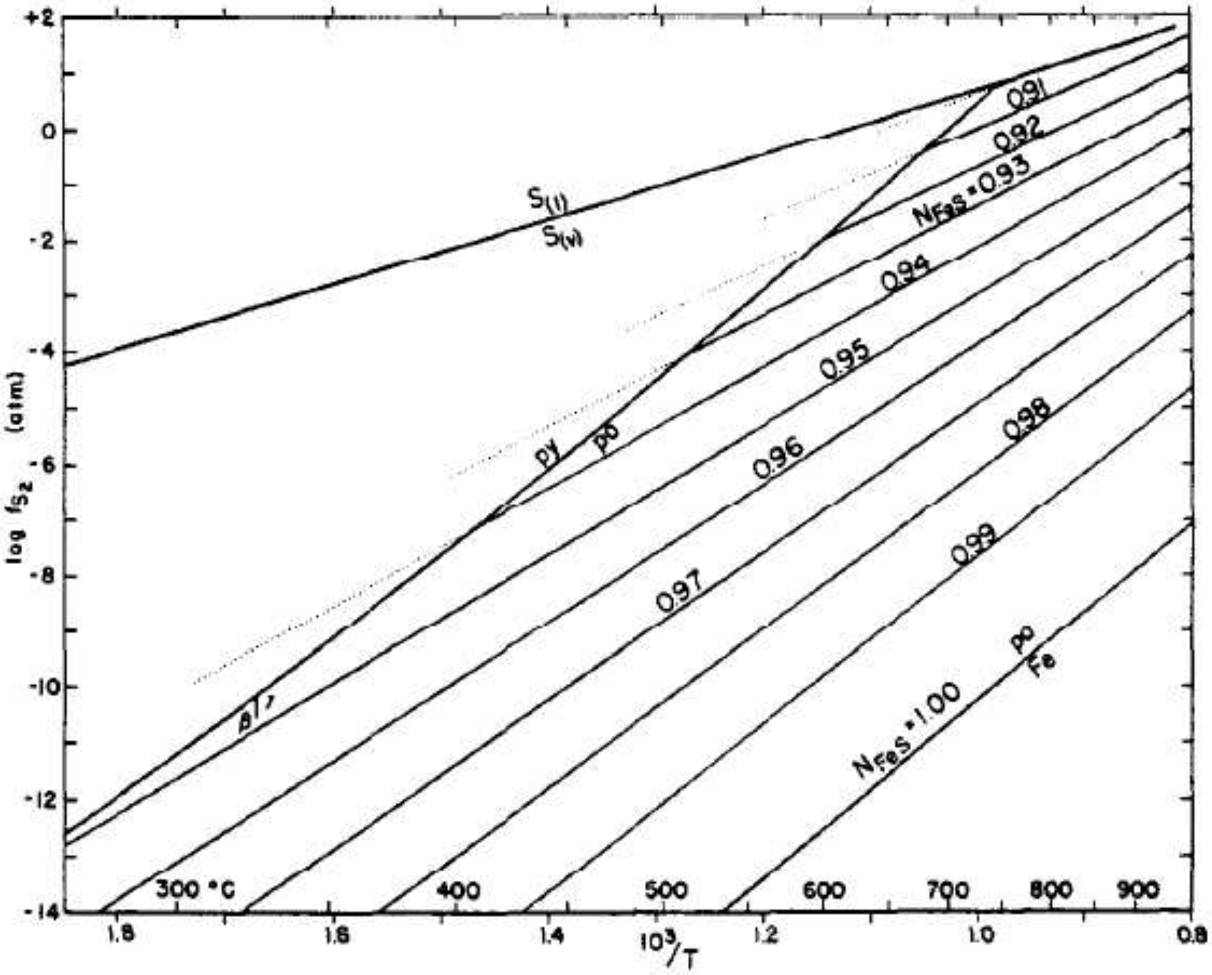

Fig. 2.5: Sulfur fugacity x temperature diagram for iron sulfides. The Py/Po line represent the equilibrium condition for the decomposition reaction of pyrite described by eq. 2.1. The different values of N represent different compositions of the formed pyrrhotite layer, and the Po/Fe represent the equilibrium condition of the decomposition of pyrrhotite in elemental iron [13].

The phase diagram of the Fe:S system for a wide range of temperatures is shown below, in Fig. 2.6 [15].

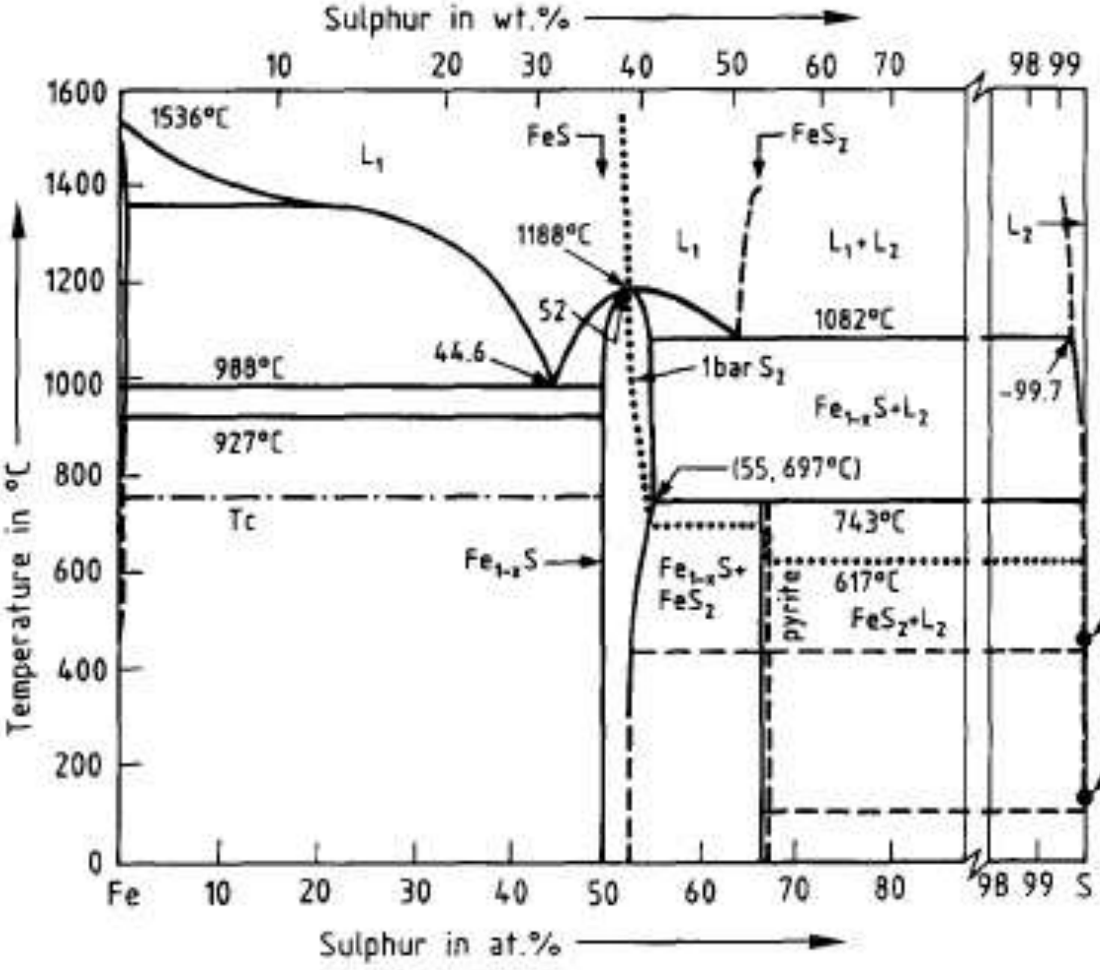

Fig. 2.6: Phase diagram of the Fe:S system [15].

2.3 STATE OF THE ART: SYNTHESIS AND DEVICES

In 1984, Tributsch *et al* reported the first attempt to use FeS_2 as semiconducting material in solar cells. Even though they obtained promising results on photocurrent generation, they obtained V_{OC} values lower than expected based on the energy gap value of the material (approximately 0.95) and negligible efficiencies [1]. Nevertheless, the authors stressed that the devices tested were made with only fairly clean synthetic material and no work on the optimization of electronic properties and surface defects was carried out. Following such pioneer works, other groups began to study the electrical properties of FeS_2, and to investigate novel synthesis processes, in order to obtain films with better quality, without the presence of secondary iron rich phases, such as pyrrhotite, and without defects such as elemental vacancies, especially sulfur. Many techniques were used to produce FeS_2 films with different degrees of purity, such as spray pyrolysis [16], Metal Organic Chemical Vapor Deposition (MOCVD) [17,18,19,20], Aerosol Assisted Chemical Vapor Deposition (AACVD) [21], Chemical Vapor Deposition (CVD) [22,2324,25,26], hydrothermal growth [27], chemical vapor transport (CVT) [6,28,29,30], and sulfurization of iron [4,14,31,32,33,34,35,36,37] and iron oxides [38,39,40,41].

CVD has been vastly used to produce FeS_2 films with different compositions and physical properties. As reported by Matt Law *et al.* [42], three main groups have been working with CVD to synthesize pyrite films. The Tributsch group at the Hahn-Meitner Institut in Berlim used iron pentacarbonyl (IPC) as iron precursor and different sulfur precursors, including, H_2S, sulfur, *tert-butyl* sulfide (TBS), and *tert-butyl* disulfide (TBDS) [17,18,43,44,45,46,47,48]. The films were grown on different temperatures (130 °C – 600 °C) and pressures, and presented **p**-type conductivity when non-intentionally doped. It was observed that temperatures higher than 450 °C were needed to avoid the presence of the polymorph marcasite. However, at temperatures higher than or equal to 550 °C, high sulfur pressures were also needed to prevent the decomposition of pyrite which causes the formation of the iron rich sulfide pyrrhotite and the release of S_2 gas. The presence of the pyrrhotite phase is particularly problematic, as it may deteriorate the optoelectronic properties of pyrite films. The Nakamura group in Japan presented remarkable results on the growth of thick pyrite films using iron (III) chloride, $FeCl_3$, as iron precursor and thioacetamide, CH_3CSNH_2, as sulfur precursor [22,23]. The use of $FeCl_3$ as iron precursor represents a major advantage due to the low cost of the reactant when compared to the more expensive IPC used by the Tributsch group. In contrast to the results obtained by the previous group, the films obtained by the Nakamura group presented **n**-type conductivity, possibly from chlorine doping [41]. Despite the promising results, including the deposition of single crystalline films in refs 21, 22, there were no further works reported by the Nakarmura group nor has any other groups reproduced their work. Finally, the group of Schoonman *et al* used iron (III) acetylacetonate, $[Fe(acac)_3]$ as iron precursor and TBDS as sulfur precursor mixed with H_2 [20,49].

The authors reported that H_2 aided the film growth. In addition, the results obtained with [Fe(acac)$_3$] were very similar to the ones obtained by the Tributsch group with IPC, and the films also presented **p**-type conductivity. The apparent inconsistence regarding the conductivity behavior of pyrite, whether it is a **p**-type or **n**-type semiconductor, even for phase pure materials, suggests that the electronic properties of the semiconductor play an important role on the cause of the low V_{OC} observed in pyrite based devices.

In 2012, O'Brien *et al* reported for the first time the use of AACVD to deposit pyrite thin films [20]. The authors had already explored the use of carbamate molecules as single source precursors to deposit other metal chalcogenides, in a homemade setup [50,51,52,53,54,55]. It was observed that the phase composition of the resulting films varied not only with synthesis parameters, such as time and temperature, but also with the precursor molecule used. The authors obtained mixed phases (pyrite + marcasite, pyrite + pyrrhotite, or pyrite + mackinawite, $Fe_{1+x}S_x$), for all precursors used and at every temperatures tested, namely from 350 ^oC to 450 ^oC, except for tris(dialkyldithiocarbamato)iron(III), which resulted in pure phase pyrrhotite for 400 ^oC and 450 ^oC . Although the presence of pyrrhotite at temperatures lower than or equal to 450 ^oC does not reflect the equilibrium conditions of the decomposition reaction of pyrite [12,13], marcasite is commonly observed along with pyrite for the temperature range used in that work. Even though the authors could not produce pure phase pyrite, they obtained promising results in the production of FeS_2 with single source precursors, by means of the AACVD technique.

In 1990, Smestad *et al* reported the advantages of preparing pyrite films from iron oxides, by means of sulfurization [37]. According to the authors, when one prepares FeS_2 films from the elements Fe and S, the reaction must firstly produce iron rich layers containing $Fe_{1-x}S$ (pyrrhotite). This argument is illustrated in the ternary phase diagram shown below in Fig. 2.7, extracted from ref 37. Thus, when preparing pyrite by reacting S with Fe, in the absence of oxygen, the reaction must pass through the Fe-S phase field, which may result in undesirable secondary iron sulfide phases. On the other hand, when preparing pyrite by adding sulfur to iron oxides, one produces only pyrite and either SO_2 gas – in the case of hematite (Fe_2O_3) precursor – or Fe_2O_3 – in the case of magnetite (Fe_3O_4) precursor. Moreover, the authors stated that more sulfur is necessary to cross the FeS_2-SO_2 tie line from Fe_2O_3 than to cross the FeS_2-Fe_2O_3 line from Fe_3O_4, meaning that more sulfur is necessary to produce pyrite when sulfurizing Fe_2O_3 in comparison with when Fe_3O_4 is used. Accordingly, this explains why in some cases it was observed traces of the precursor Fe_2O_3, indicating that the reaction was not completed. However, the authors used short times, much shorter than the ones reported for other techniques, which contributes for the non-completeness of the reaction. The sulfurization of Fe_2O_3 to FeS_2 follows a simple exothermic reaction, described below [37]:

$$2Fe_2O_{3(s)} + 11S \leftrightarrow 4FeS_{2(s)} + 3SO_{2(g)}, \quad \Delta G = -334.23\,kJ/mol\,(673\,K, 1\,atm) \quad [2.2]$$

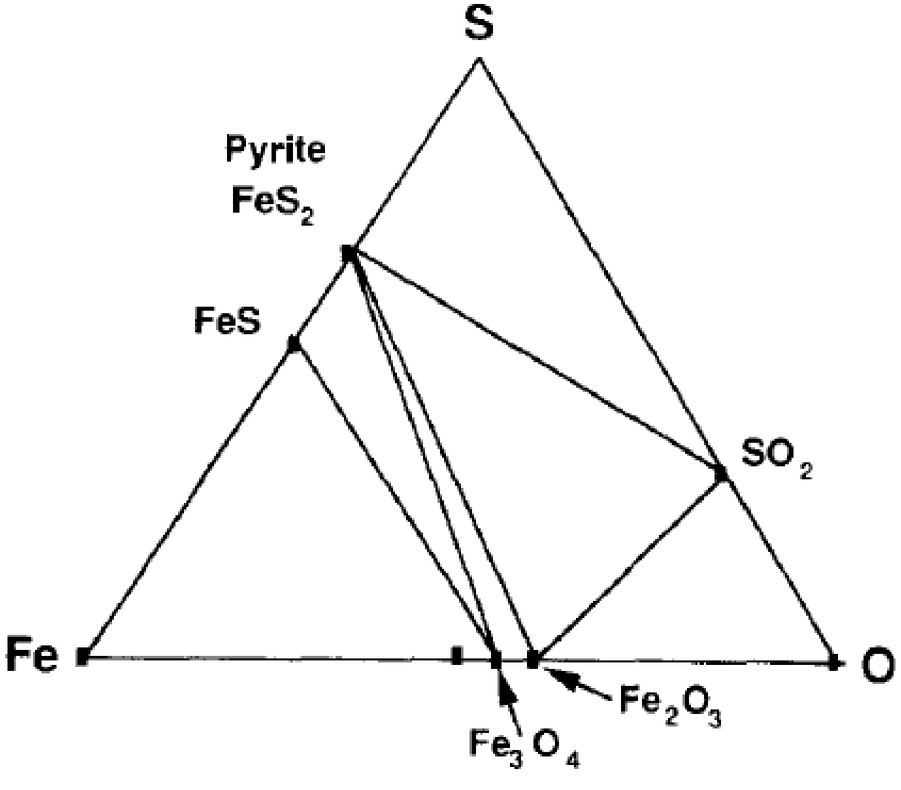

Fig. 2.7: Ternary Fe-S-O phase diagram extracted from G. Smestad *et al*, Sol. En. Mater, 20 (1990) 149. Note that the reaction between the elements Fe and S must pass through the Fe-S phase field,

As listed before, other groups reported the synthesis of FeS_2 by sulfurization of iron oxides, typically using Fe_2O_3 as precursor. We highlight the works of Bessaïs *et al* and Fangyang Liu *et al*. The first group produced good quality films with high absorption coefficient ($\alpha \sim 10^4$ cm $^{-1}$) and **p**-

type doping, by sulfurizing Fe_2O_3 films deposited by spray pyrolysis. Whereas the former sulfurized amorphous (evidenced by the lack of XRD peaks) Fe_2O_3 films deposited via successive ionic layer deposition (SILAR) and obtained pyrite films with **p**-type doping and high absorption coefficient (> 10^{5} cm^{-1}) as well.

Similar to CVD, CVT has been vastly used to produce FeS_2 with great quality. In 1986, the first report on the growth of pyrite crystals by CVT presented a polycrystalline material produced from elemental iron and sulfur lumps heated in evacuated and sealed quartz ampoules with small amounts of different halogens, halides and ammonium halides as transporting agents [56]. The transporting agents were shown to influence on the transport rate, as expected, but also on the electronic properties of the crystals, as both **n**-type and **p**-type doping conductivity were observed. The differences in the doping type were attributed to differences in the incorporation of impurities during the process, with Cl and Br resulting in **n**-type and I_2 resulting in **p**-type.

Chlorine doping in pyrite has also been suggested to result in films with electron as major carriers, as discussed earlier regarding CVD grown films with $FeCl_3$ [41]. Although other elements have been used to intentionally dope pyrite films, such as Co, Cu, Ni (**n**-doping) [57,58,59,60,61,62], and As (**p**-doping) [47,48], the intrinsic electronic character of synthetic pyrite presented complications. Typically, pyrite isolated single crystals were reported as naturally **n**-doped, whereas polycrystalline pyrite films presented **p**-type conductivity [6,8]. Nevertheless, the reasons for the dependence of electronic behavior of FeS_2 with the structure of the sample, meaning, whether is a single crystal or films, were not clear. The situation became even more cumbersome after the works of I.J. Ferrer *et al*, who reported **n**-type FeS_2 film produced by sulfurization of FeS [63]; Liang Meng *et al*, who reported films produced by sulfurization of Fe_2O_3 with both **n**-type (at $T \leq 450$ °C) and **p**-type (at $T > 450$ °C) character [40]; and C. Leighton *et al*, who produced pyrite films by sulfurizing sputtered iron films and observed a crossover between **p**-type doping to **n**-type doping as the sulfurization temperature increased [4].

The crossover effect observed in the later work was correlated with changes in the microstructure and stoichiometry of the films. The authors observed that, as the sulfurization temperature increased, the grain size and the intensity of the XRD peak of the pyrite (002) plane increased as well. In addition, the Fe:S ratio of the films also increased, starting with an excess of sulfur and later presenting stoichiometric pyrite composition, *i.*e, Fe:S = 1:2. These changes in composition and microstructure of the films with the sulfurization temperature followed changes in the conduction features of the films. For lower temperatures, – ergo, corresponding to small grain, excess sulfur and low intensity of the (002) peak films – the Hall data dependence with temperature was best described by means of a variable hopping model. The authors presented two possible variable hopping mechanisms to describe the data, the Efros-Shklovskii variable-range hopping (ES VRH) and the Inter-granular hopping (IGH), but decided in favor of the IGH, due to the fact that the synthesis method used was diffusion-limited. Such diffusion process may easily generate a nanoscale inhomogeneity which could then explain a conduction by means of IGH. At temperatures higher than 400 ^{o}C, as the grains size and the intensity of the (200) plane peak intensity increased substantially, conduction changes from a variable-hopping mechanism to a more conventional semiconductor interband conduction. Moreover, the Hall coefficient switched to negative values indicating electrons became the majority carriers. In light of the causes suggested by the authors to explain a conduction by IGH, one may interpret that, as the sulfurization temperature increased and the grains coalesced, the films became also more homogeneous (as evidenced by the approximation to a stoichiometric composition of FeS_2), eliminating the hopping hole-like conduction. However, the authors could not further explain the **n**-type conductivity and rather attributed the switch to external factors such as doping by diffusion from the substrate. Nevertheless, the results obtained by the group of C. Leighton not only raised new questions upon the electric properties of pyrite, but also cast doubt upon previous works reporting **p**-type conductivity of FeS_2 films. Even though, neither of the previous works had ever performed Hall measurements with variable temperature. Table I depicts a detailed list of the results obtained so far regarding characterization of conductivity in FeS_2 system, with the types of doping observed, associated with the method and reactants used to produce the material and whether the material was an isolated single structure (S.C) or a polycrystalline film (film).

At last, in 2014, Matt Law *et al* grew FeS_2 single crystals of a few micrometers large with CVT by using sodium sulfide (Na_2S) as transporting agent [6]. According to the authors, Na_2S acts as an efficient flux for pyrite crystal growth because it is liquid over a wide range of temperatures, which improves the coalescence of grains during pyrite crystallization, and the fact that Na does not incorporate in the pyrite structure in significant levels. The authors investigated the composition of the crystals and observed a high degree of purity – the highest ever achieved by the time, according to the authors – with a total lattice impurity content of approximately 80 ppm. Amongst the detected elements, hydrogen represented the major lattice impurity, whereas carbon and oxygen were dominants at the surface, which was attributed to particle contamination after growth. Sodium was also found more concentrated at the surface of the crystals, indicating that Na did not dope the crystal during the CVT process, as intended. Slabs of the crystals were cut to perform Hall measurements. The authors investigated, for the first time, the electrical conductivity of FeS_2 crystals at different temperatures ($40K \leq T \leq 700K$) and they observed a crossover at $T \sim 80$ K between **p**-type to **n**-type conductivity. A numerical fitting of the Hall data using a multi-layer model unveiled the existence of a hole-rich inversion layer at the surface of the **n**-type crystals. Accordingly, as the temperature decreases, the electrons of the bulk are frozen out and the holes at the surface dominate the electrical transport, as observed by the positive value of the Hall coefficient. The existence of the surface layer was also corroborated UPS measurements, which showed a difference between the Fermi level (E_F) and the edge of the valence band (E_V) of about 0.1 eV, which characterizes a **p**-type semiconductor. Moreover, the existence of such hole-rich surface, explains both the low V_{OC} observed in pyrite solar cells, caused by tunneling across the surface layer, and the **p**-type conductivity of FeS_2 thin films, often reported, since, in such structures, surface conductivity prevails due to the high surface-to-volume ratio. In fact, the surface hole-rich layer explains the results of C. Leighton, which observed FeS_2 with larger particles (sulfurized at increasingly higher temperatures) presented **n**-type conductivity, as opposed to films with smaller particles (sulfurized at low temperatures) which showed **p**-type conductivity. It also corroborates the results of the Nakamura group who obtained **n**-type conductivity for single crystal pyrite films. Therefore, in order to obtain FeS_2 solar cells with considerable efficiency, one must first dominate the growth of large particle pyrite films, thus minimizing the influence of the surface inversion layer.

Table I: Details of the reported types of doping observed in synthetic FeS_2 over the years.

Year	Authors	Method	Reactants	doping	structure
1983	Tributsch *et al*	Natural CVT	-------------	**n**-type	S.C
				n-type	
1986	Tributsch *et al*	CVT	I_2	**p**-type	S.C
			Cl, Br	**n**-type	
1990	Tributsch *et al*	Sulf. of iron oxides	Sulfur vapor	**p**-type	Film
1990	E. Buscher *et al*	Sulf. of iron	S	**p**-type	Film
1990	Tributsch *et al*	MOCVD	IPC and S or H_2S	**p**-type	Film
1993	I.J. Ferrrer *et al*	Sulf. of iron	S	Not defined*	Film
1994	I.J. Ferrrer *et al*	Sulf. of iron	S	Not defined*	Film
1999	Tributsch *et al*	MOCVD	IPC and TBDS	**p**-type	Film
2003	Nakamura	Spray Pyrolisis	$FeSO_4$, and $(NH_4)_2S_x$	**p**-type	Film
2003	N. Hamdadou *et al*	Sulf. of iron	S	**p**-type	Film
2003	I.J. Ferrer *et al*	Sulf. of FeS	S	**n**-type	Film
2005	B. Bessaïs *et al*	Sulf. or Fe_2O_3	S	**p**-type	Film
2011	Jinsong Huang *et al*	Surfactan assisted hot injection + dip coating		**p**-type	NC film
2012	M. Law *et al*	APCVD	$Fe(acac)_3$ and TBDS	**p**-type	Film
2012	Liang Meng *et al*	Sulf. of Fe_2O_3	S	**p**-type ($T >$ 450 ^{o}C) **n**-type ($T \leq$ 450 ^{o}C)	Film
2013	Fangyang Liu *et al*	Sulf. of Fe_2O_3	S	p-type	Film
2013	C. Leighton *et al*	Sulf. of iron	S	**p**-type ($T <$ 400 ^{o}C) **n**-type ($T >$ 400 ^{o}C)	Film
2013	Song Jin *et al*		$FeCl_2$ or $FeBr_2$ and S	**p**-type	Film
2013	M.T.S. Nair *et al*	CBD and sulfur annealing	TEA, $Fe(NO_3)_3$, $Na_2S_2O_3$	**p**-type	Film
2014	M. Law et al	CVT	Fe, S, and Na2S	**p**-type (at $T <$ 80 K) **n**-type (at $T >$ 80 K)	S.C

References

---

1 A. Ennaoui, H. Tributsch, Solar Cells **13** (1984) 197
2 A. Ennaoui, A.S. Fiechter, C. Pettenkofer, N. Alonso-Vante, K. Büker, M. Bronold, C. Höpfner, H. Tributsch, Sol. Energy Mater. Sol. Cells **29** (1993) 289
3 C. Wadia, A.P Allivisatos, D.M. Kammen, Environ. Sci. Technol. **43** (2009) 2072
4 X. Zhang, M. Manno, A. Baruth, M. Johnson, E.S. Aydil, C. Leighton, ACS Nano **7** (2013) 2781
5 J. Puthussery, S. Seefeld, N. Berry, M. Gibbs, M. Law, J. Am. Chem. Soc. **133** (2011) 716
6 M. Limpinsel, N. Farhi, N. Berry, J. Lindemuth, C.L. Perkins, Q. Linf, M. Law, Energy Environ. Sci. **7** (2014) 1974
7 C. Steinhagen, T.B. Harvey, C.J. Stolle, J. Harris, B.A. Korgel, J. Phys. Chem. Lett. **3** (2012) 2352
8 M. Cabán-Acevedo, N.S. Kaiser, C.R. English, D. Liang, B.J. Thompson, H. Chen, K.J. Czech, J.C. Wright, R.J. Hamers, S. Jin, J. Am. Chem. Soc. **136** (2014) 17163
9 M.E. Fleet, Canadiam Mineralogist, **10** (1970) 225
10 J.A. Leiro, S.S. Mattila, K. Laajalehto, Surface Science **547** (2003) 157
11 F. Grønvold, E.F. Westrum Jr, J. Chem. Thermodynamics **8** (1976) 1039
12 A.R. Lennie, D.J. Vaughan, Americ. Miner. **77** (1992) 1166
13 P. Toulmin III, P.B. Barton Jr, Geochim Cosmochim Acta **28** (1964) 641
14 G. Hu, K. Dam-Johansen, S. Wedel, J.P Hansen, Progr. En Combust. **32** (2006) 295
15 G. Pimenta, W. Kautek, Thin Solid Films, **219** (1992) 37
16 A. Yamamoto, M. Nakamura, A. Seki, E.L. Li, A. Hashimoto, S. Nakamura, Sol. En. Mater. **75** (2003) 451
17 C. Höpfner, K. Ellmer, A. Ennaoui, C. Pettenkofer, S. Fiechter, H. Tributsch, J. Cryst Growth **151** (1995) 325
18 B. Thomas, T. Cibik, C. Höpfner, K. Diesner, G. Ehlers, S. Fiechter, K. Ellmer, J. Mater. Sci. Mater. El. **9** (1998) 61
19 J. Oertel, K. Ellmer, W. Bohne, J. Röhrich, H. Tributsch, J. Cryst Growth **198/199** (1999) 1205
20 B. Meester, l. Reijnen, A. Goossens, J. Schoonman, Chem. Vap. Deposition **6** (2000) 121
21 M. Akhtar, A.L. Abdelhady, M.A. Malik, P.O`Brien, J. Cryst. Growth **346** (2012) 106
22 B. Meester, R.A. du Bois, A. Goossens, J. Schoonman, J. Phys. IV **9** (1999) 425
23 N. Takahashi, T. Sawada, T. Nakamura, T. Nakamura, J. Mater. Chem. **10** (2000) 2346
24 N. Takahashi, Y. Nakatani, T. Yatomi, T. Nakamura, Chem. Mater. **15** (2003) 1763
25 N. Berry, M. Cheng, C.L. Perkins, M. Limpinsel, J.C. Hemminger, M. Law, Adv. Energy Mater. **2** (2012) 1124
26 L. Samad, M. Cabán-Acevedo, M.J. Shearer, K. Park, R.J. Hamers, S. Jin, Chem. Mater. **27** (2015) 3108
27 J. Xia, X. Lu, W. Gao, J. Jiao, H. Feng, L. Chen, Electrochim Acta **56** (2011) 6932
28 J. Zavašnik, A. Rečnik, J. Cryst. Growth **367** (2013) 18
29 S.W. Lehner, K.S. Savage, J.C. Ayers, J. Cryst Growth **286** (2006) 306
30 C.H. Ho, C.E. Huang, C.C. Wu, J. Cryst Growth **270** (2004) 535
31 Y. Hu, Z. Zheng, H. Jia, Y. Tang, L. Zhang, J. Phys. Chem. C **112** (2008) 13037
32 P. Díaz-Chao, I.J. Ferrer, C. Sánchez, Thin Solid Films **516** (2008) 7116
33 J.M. LaForge, B. Gyenes, S. Xu, L.K. Haynes, L.V. Titova, F.A. Hegmann, M.J. Brett, Sol En. Mat. Sol Cells **117** (2013) 306
34 X.F. Li, Y. Wang, L. Meng, Mater. Res. Bull. **44** (2009) 462
35 Z.J. Luan, Y. Wang, L.Y. Huang, F. Wang, L. Meng, Mater. Res. Innov. **15** (2011) 349
36 N. Hamdadoua, A. Khelil, J.C. Bernède, Mater. Chem. Phys. **78** (2003) 591
37 D. Wana, B. Wanga, Y. Wanga, H. Sunb, R. Zhanga, L. Wei, J. Cryst Growth **257** (2003) 286
38 G. Smestad, A. Ennaoui, S. Fiechter, H. Tributsch, W.K. Hofmann, M. Birkholz, W. Kautek, Sol. Energy Mater. **20** (1990) 149
39 K. Sun, Z. Su, J. Yang, Z. Ha, F. Liu, Y. Lai, J. Li, Y. Liu, Thin Solid Films **542** (2013) 123
40 B. Ouertani, J. Ouerfelli, M. Saadoun, B. Bessaïs, M. Hajji, M. Kanzari, H. Ezzaouia, N. Hamdadou, J.C. Bernède, Mater. Lett **59** (2005) 734
41 F. Wang, L. Huang, Z. Luan, J. Huang, L. Meng, Mater. Chem. Phys. **132** (2012) 505

---

42 N. Berry, M. Cheng, C.L. Perkins, M. Limpinsel, J.C. Hemminger, M. Law, Adv. Energy Mater. **2012** (2) 1124

43 G. Chatzitheodorou , S. Fiechter , R. Könenkamp , M. Kunst, W. Jaegermann , H. Tributsch , Mater. Res. Bull. **21** (1986) 1481

44 D.M. Schleich, H.S.W. Chang, J. Cryst. Growth **112** (1991) 737

45 A. Ennaoui, S. Schroetter, S. Fiechter, H. Tributsch, J. Mater. Sci. Lett. **11** (1992) 1131

46 K.L. Ellmer, D. Lichtenberger, A. Ennaoui, C. Hopfner, S. Fiechter, H. Tributsch , Proc. 23rd Photovoltaics Spec. Conf. (1993) 535

47 B. Thomas, C. Höpfner, K. Ellmer, S. Fiechter, H. Tributsch, J. Cryst. Growth **146** (1995) 630

48 B. Thomas, K. Ellmer, M. Müller, C. Höpfner, S. Fiechter, H. Tributsch, J. Cryst. Growth **170** (1997) 808

49 L. Reijnen, B. Meester, A. Goossens, J. Schoonman, J. Electrochem. Soc. **147** (2000) 1803

50 M. Kemmler, M. Lazell, P. O'Brien, D.J. Otway, J. Park, J.R Walsh, J. Mater. Sci. Mater El **13** (2002) 531

51 J. Park, M. Afzaal, M. Kemmler, P. O'Brien, D.J. Otway, J. Raftery, J. Waters, J. Mater. Chem. **13** (2003) 1942

52 M. Afzaal, D. Crouch, P. O'Brien, J. Park, J. Mater. Sci. Mater El **14** (2003) 555

53 A. Adeogun, M. Afzaal, P. O'Brien, Chem. Vap. Deposition **12** (2006) 597

54 J. Akhtar, M.A. Malik, P. O'Brien, M. Helliwell, J. Mater. Chem. **20** (2010) 6116

55 K. Ramasamy, M.A. Malik, M. Helliwell, J. Raftery, P. O'Brien, Chem. Mater. **23** (2011) 1471

56 S. Fiechter, J. Mat, A. Ennaoui, J. Cryst. Growth, **78** (1986) 438

57 I.J. Ferrer, C. De las Heras, C. Sánchez, Appl. Surf. Sci. **70/71** (1993) 588

58 I.J. Ferrer, F. Caballero, C. De las Heras, C. Sanchez, Solid State Commun, **89** (1994) 349

59 A.M. Abd El Halim, S. Fiechter, H. Tributsch, Electrochimica Acta **47** (2002) 2615

60 C.H. Ho, C.E. Huang, C.C. Wu, J. Cryst Growth **270** (2004) 535

61 S.W. Lehner, K.S. Savage_, J.C. Ayers, J. Cryst. Growth **286** (2006) 306

62 S. W. Lehner, N. Newman, M. van Schilfgaarde, S. Bandyopadhyay, K. Savage, P.R. Buseck, J. Appl. Phys **111** (2012) 083717

63 A. Gomes, J.R. Ares, I.J. Ferrer, M.I. da Silva Pereira, C. Sánchez, MRS Bulletin, **38** (2003) 1123

3 Pyrite: Experimental Methods

In this chapter, we present the methods of sample preparation and characterization techniques. First, we detail the techniques used to characterize the samples produced throughout the work. Then, we demonstrate the construction of an Aerosol Assisted Chemical Vapor Deposition (AACVD) reactor that was used to produce iron sulfide films along with the results obtained using the equipment. Then, we demonstrate the need to increase the sulfur content in the produced films, since we obtained mainly the pyrrhotite phase of iron sulfide, by means of a sulfurization treatment. We demonstrate a few apparatuses used for sulfurization, which were optimized and resulted in a final and novel apparatus, which we named Russian Doll. The process of sulfurization was further used to produce pyrite films from iron oxide (hematite) films produced by spin coating, which became the main process studied in this work and described with further details in the subsequent chapter.

3.1 CHARACTERIZATION TECHNIQUES

X-Ray Diffraction (XRD):

We used XRD in this work to determine the phase composition of the films. The measurements were carried out in the Crystallography Laboratory (LabCri) of UFMG, with a PANalytical EMPYREAN diffractometer using Cu Kα radiation (λ = 1.540598 Å), working in continuous scan mode with grazing incidence. The peaks were indexed using the Crystallography Open Database (COD) to compare with reference data. We used grazing incidence because of the small thickness of our films. This feature commonly results (because X-Rays have high penetration depths) in a low signal from the films material and a high signal from the substrate, when conventional θ/2θ scan modes are used. Fig. 3.1 illustrates the difference in using grazing incidence (Fig. 3.1a) and conventional (Fig. 3.1b) scan modes to analyze a thin sample of CdSeS deposited on graphite [1]. When using conventional scan, only the signal of the substrate is detected, whereas for grazing incidence, the film is also noticeable.

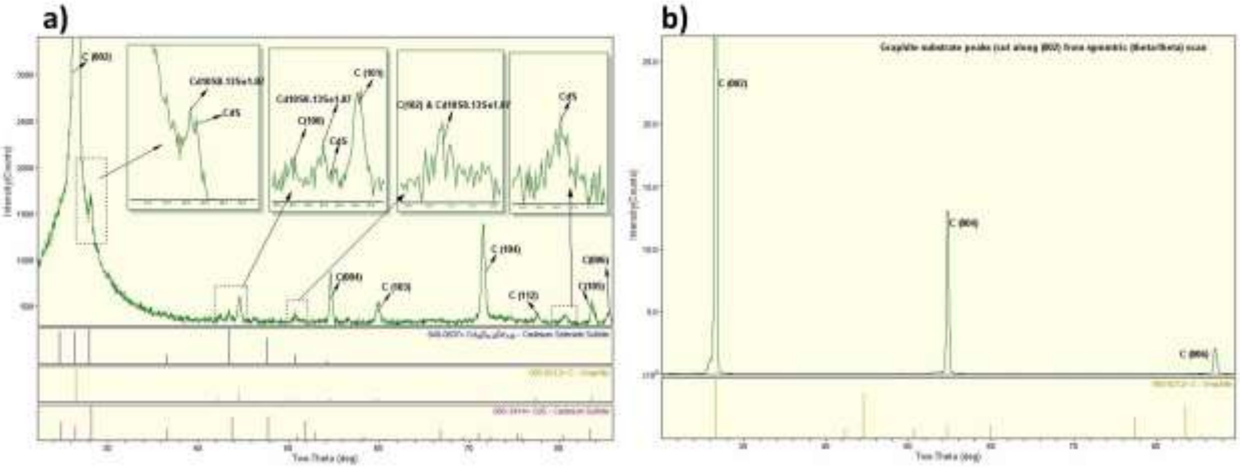

Fig. 3.1: Example of the difference in using **a)** grazing incidence and **b)** conventional θ/2θ scan modes to analyze a thin film.

Scanning and transmission electron microscopies (SEM/TEM)

We used SEM and TEM to determine phase composition and to analyze the microstructure of the films. We also used Scanning Electron Microscopy (SEM) imaging to infer the phase composition by analyzing the crystal habits present in the films, and, we used TEM to determine the crystallinity of different regions of some samples. All, the SEM experiments were performed at the Microscopy Center of UFMG in a FEI Quanta 3D FEG FEI electron microscope. All the samples were grounded to the holder with conductive carbon tape, to prevent charging effect. The samples analyzed by TEM were scratched into a flask containing isopropanol and dropped into a holey carbon holder.

Spectroscopic Ellipsometry (SE)

Ellipsometry is an indirect optical technique that analyzed the change in the polarization of light due to the interaction of light with matter. By comparing the initial with the final polarization state of light, it is possible to determine microstructure characteristics – such as roughness and thickness – as well as optical functions – ($\varepsilon_1, \varepsilon_2$) or (n,k) – of the material [2]. The technique consists on irrradiating a sample with a light beam with a known polarization state – typically linear – and measuring the final polarization state of the reflected light. The change in the polarization state is usually related to the complex number ρ, which is given by the ratio of the components – perpendicular (r_S) and parallel (r_P) to the incidence plane – of the electric field:

$$\rho = \frac{r_S}{r_P} = tan(\psi) e^{i\Delta}, \quad [3.1]$$

where *tan (ψ)* represents the ratio of the reflection coefficient amplitudes, and *Δ* is the phase difference in both components r_S and r_P. For spectroscopic ellipsometry, we measure the angles (*ψ, Δ*) for a range of wavelengths. In this work, we spanned the energy range of 0.7 – 5.0 eV. A typical ellipsometry experiment is illustrated in Fig. 3.2.

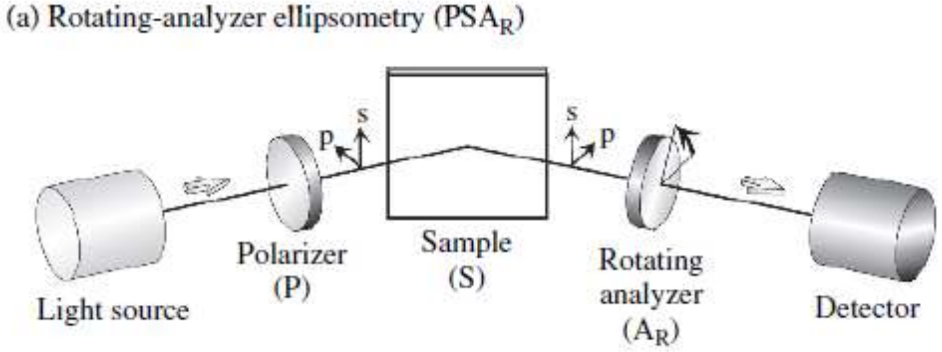

Fig. 3.2: Typical set up of an ellipsometry experiment.

Hall effect and Van der Pauw method

The Hall effect is characterized by the appearance of off diagonal terms in the resistivity of materials, when current flows in the presence of a transversal magnetic field. The appearance of such terms are related to the Lorentz force, **F** = q(**v** x **B**), which deflects and accumulates charge carriers on the sides of the material. The deflection occurs until the electric field produced by the accumulated charges balances the Lorentz force, *i.e*, the equilibrium condition is achieved when:

$$q v_x B_z = q E_y, \quad [3.2]$$

where v_x is the drift velocity of the carriers, and the directions of the vectors are expressed according to Fig. 3.3. Since the current density $j_x = -nev_x$, the equilibrium conditions lead to:

$$E_y = -\left({}^{1}\!/_{ne}\right) j_x B_z = R_h B_z, \qquad [3.3]$$

where the quantity $R_h = -(1/ne)$ is known as the Hall coefficient [3].

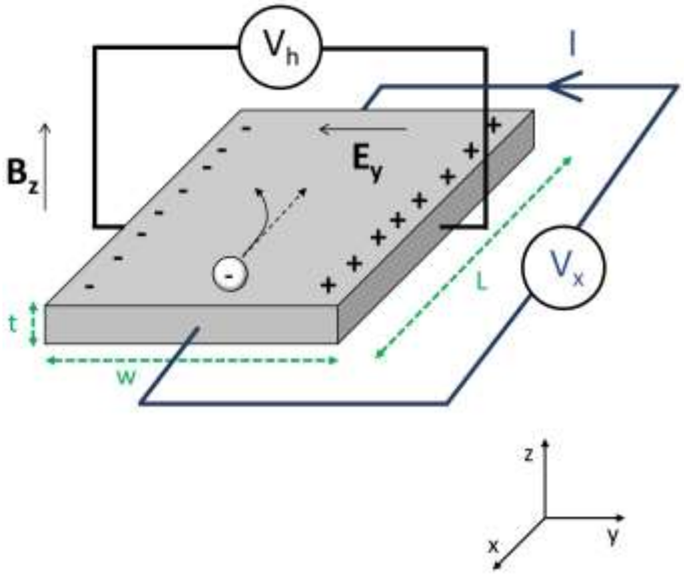

Fig. 3.3: Scheme illustrating an experiment measuring the Hall effect. We apply a voltage V_X and measure a voltage V_h, established in the equilibrium condition of eq. 3.3. I represents the direction of the ideal current.

Fig. 3.3 illustrates well the case of a metal, however, in a semiconductor, both holes and electrons commonly contribute to the current. Since they usually have different concentrations and have different mobilities (μ), eq. 3.3 becomes more complex and the Hall coefficient becomes:

$$R_h = \frac{p\mu_h^2 - n\mu_e^2}{e(p\mu_h + n\mu_e)^2} = \frac{p - nb^2}{e(p + nb)^2}, \qquad [3.4]$$

where, p and n are the concentrations of holes and electrons, respectively, μ_h and μ_e represent the mobilities of holes and electrons, respectively, and $b = \mu_e / \mu_h$. Therefore, by performing Hall effect experiments in a material, one may obtain valuable properties such as carrier signal and concentration, and mobility.

Every Hall effect experiment conducted in this work, was performed with the Van der Pauw method, which is widely used to study samples with arbitrary shapes [4].

3.2 AACVD AND SINGLE SOURCE PRECURSORS

AACVD consists on a CVD process where the reactants are contained within small droplets, usually produced by ultrasound, and carried out by a carrying gas, such as Argon, to a hot zone where solvent evaporation, reaction and deposition on a substrate occur. The main advantages of this technique is the form of transport, which enables the use of precursors with low vapor pressure, since they are carried inside a micro droplet, and not in the gas phase as it happens in more conventional CVD processes. The aerosol is usually generated by an ultrasound source that sonicates the solution containing the reactants.

Recently, the group of Professor de Lima of the Chemistry Department of UFMG started to research the synthesis of carbamate molecules, depicted in Fig. 3.4, to be used as single source precursors in the growth of metal sulfide nanoparticles. The group of Prof. de Lima has successfully produced dithiocarbamate (DTC) of several different metals, such as, Sn, Zn, Cu, Bi, etc [5,6,7,8]. Furthermore, de Lima *et al* have successfully produced nanoparticles of several metal sulfides by decomposition reaction of the produced carbamate molecules, such as SnS, ZnS, and Bi_2S_3 [2,3,9,10,11,]. The use of carbamate molecules in the synthesis of pyrite films was reported for the first time by O'Brien *et al* in 2012 [12]. The authors reported iron sulfide films with different compositions depending on both the temperature and the precursor used. Four different single source precursors were tested and growth conditions spanned a short temperature range, between 350 ^{o}C and 450 ^{o}C. As mentioned in the previous chapter, even though, the authors did not succeed in obtaining pure phase pyrite, they did obtain, in some cases, a mixture of both FeS_2 polymorphs, with no trace of other iron sulfides, showing promising results.

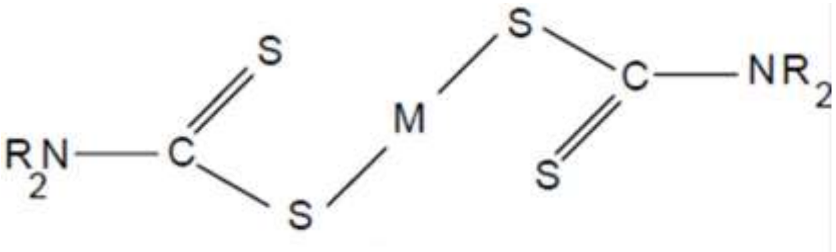

Fig. 3.4: Generic carbamate molecule of a given metal, M. R represents an organic radical.

The use of single source precursors in AACVD processes have also been reported regarding the deposition of controlled doped materials, and ceramic alloys [13,14,15,16,17,18,19,20]. The growth of controlled doped materials is of particular interest for photovoltaic applications, in order to fabricate good quality junctions (**p**-**n**, or Schottky junctions) which gives better efficiency devices. Therefore, giving the advantages and potential of AACVD to grow films with different compositions, the promising results already obtained by the group of O'Brien, and the expertise of the chemistry department regarding the synthesis of carbamate molecules, a partnership was established with Prof. de Lima and the authors of this work, in order to deposit films of metal sulfides, especially FeS_2, using the single source precursors Prof de Limas`s group was producing. The AACVD processes was carried out in a homemade reactor, presented in the next section along with preliminary results obtained.

3.3 HOMEMADE AACVD REACTOR AND PRELIMINARY RESULTS

3.3.1 – CONSTRUCTION OF THE REACTOR

Fig. 3.5 depicts the AACVD home-made reactor, built with the purpose of depositing metal sulfide films using carbamate molecules. It is a cold wall reactor, where a graphite susceptor (1) is placed inside a fused silica tube and heated by high power infrared lamps (Bravoluz, 1600 W, 2600 K color temperature). The aerosol droplets are generated by an ultrasound humidifier (2) – NS, Humid Air Plus® – that sonicates the solution inside a customized Erlenmeyer flask with three attachments: the first (3) is connected to the carrier gas (in this case, argon); the second one (4) is attached to a separating funnel (6) used to refill the solution during the process; and the third one (5) is connected to a customized glass tube (8) with an oval extremity that goes inside the fused silica tube carrying the mist (mixture of the generated aerosol and argon) onto the surface of the graphite susceptor, where decomposition and reaction occurs. The system composed by the ultrasound generator, the customized Erlenmeyer flask and the separating funnel is responsible for feeding the reactants into the reactor at an approximately constant mass rate. Just before the fused silica tube, we placed a laser with light dependent resistors (LDRs), used to monitor the density of the mist during the process (7). The laser passes through an inbuilt beam splitter, which directs one beam into the region where the mist flows, being further scattered in the direction of one of the LDRs, and the other is directed straight to another identical LDR. The system composed by the laser, beam splitter and LDRs, is responsible to monitor the density of the mist during the process, by monitoring the potential difference in the LDR that is radiated with the beam scattered by the mist and comparing the value obtained with the reference value given by the other LDR. As the mist becomes more or less dense, the scattering also varies, increasing or decreasing the intensity of the beam that radiates the LDR, affecting the value of the potential difference in the sensor. To increase the density of the mist back to the starting conditions, more solution is added to the Erlenmeyer flask, by opening the knob of the separating funnel, as the variation of the density of the mist in time stems, mainly, to the decrease in the volume of the solution. If the mist, for some reason, becomes thicker, we simply diminish the intensity of the ultrasound generator. The later situation was rarely observed in our experiments. The variation of the density of the mist was observed to affect the deposition – as expected, for it also varies the mass transport to the substrate – hence the monitoring system was built to improve both reproducibility and control of the deposition parameters.

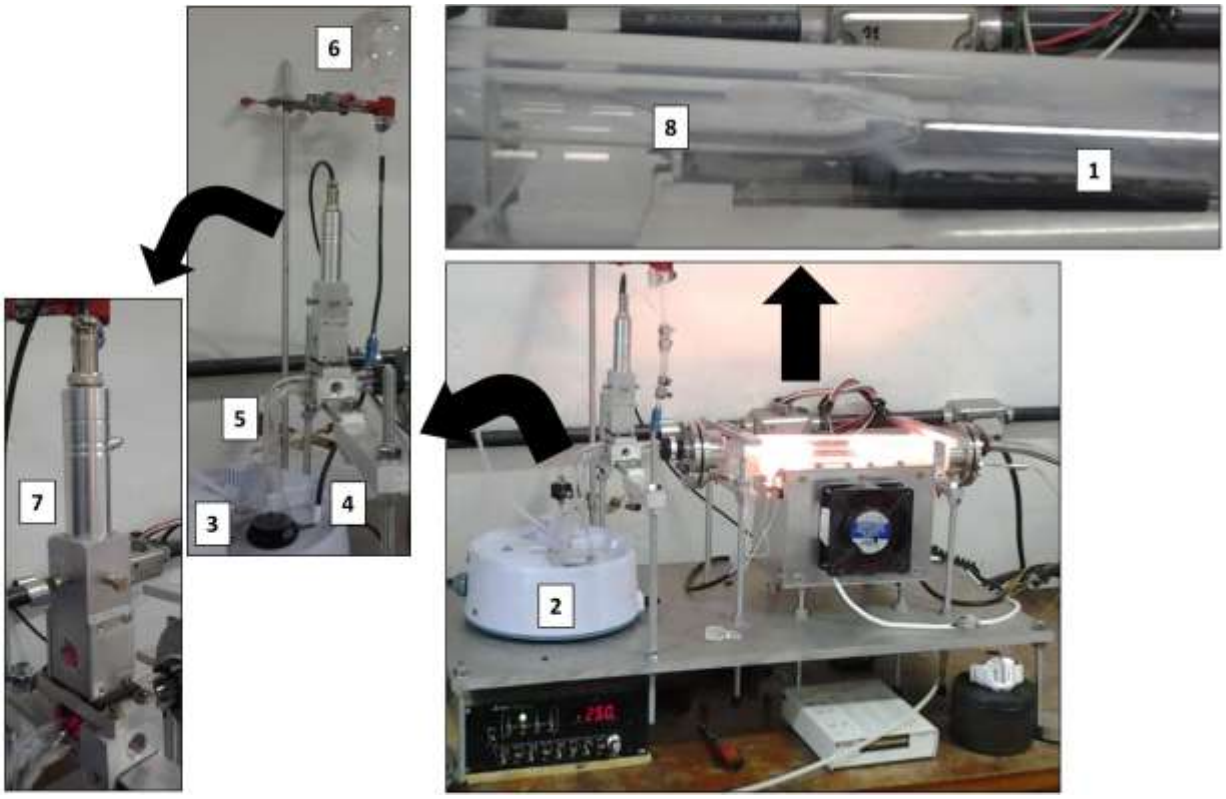

Fig. 3.5: Photograph of the home-made AACVD reactor. **1)** Graphite block used as both substrate holder and heater, by absorption of the light emitted by halogen lamps; **2)** Home humidifier used as ultrasound generator; **3, 4, 5)** attachments on the customized Erlenmeyer flask that are connected to the carrier gas, separating funnel and transporting customized glass tube that carries the mist onto the surface of the holder, respectively; **6)** separating funnel used as reservoir of solution to keep the volume of solution inside the Erlenmeyer flask constant; **7)** system (highlighted) to monitor the density of the mist by means of a laser, beam splitter and LDRs connected to a computer; **8)** customized glass tube that carries the mist onto the surface of the holder.

Generally, a deposition reaction with the homemade reactor occurs in the sequential steps: solution preparation, aerosol generation followed by mist flow, decomposition and reaction of the aerosol succeeded by film deposition on the substrate which is placed at the surface of the holder. Therefore, typical parameters of deposition are: concentration of the solution, carrier gas (argon) flow, – set in a MKS flow controller – mist density, – defined by the intensity of the ultrasound and monitored by the system inbuilt shown in Fig. 3.5 – temperature of the graphite holder, – set and controlled by a Contemp process controller and thermocouple inserted in the holder – and deposition time. A set of initial parameters were chosen based on preliminary tests and on the work of O'Brien.

3.3.2 – PRELIMINARY RESULTS

All the films produced by AACVD in the homemade reactor depicted in Fig. 3.5 were black colored and presented poor adhesion to the substrate. Fig. 3.6 shows the XRD pattern of a film deposited at 350 °C for 60 minutes, using a 2.67 mg/ml solution of iron di-tiocarbamate (FeDTC) and toluene and carried by 250 sccm argon flow. The film has pyrrhotite structure (pyrrhotite reference peaks also shown for comparison) composed by small crystallites, as evidenced by the large peaks. No other iron sulfide phases could be detected with XRD measurements.

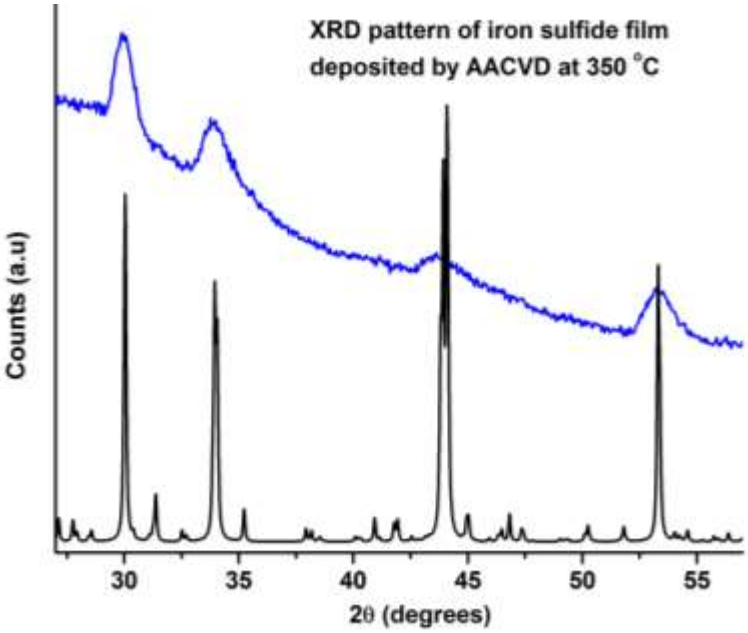

Fig. 3.6: XRD pattern of the film deposited by AACVD in homemade reactor at 350 °C. Also shown, the pyrrhotite reference XRD data.

SEM depicts large tabular particles (Fig. 3.7 **a**), apparently randomly oriented and disconnected with each other. In Fig. 3.7 **b** we also show the measured lengths of some particles, whose values are of the order of 1 µm. The large size of the particles and the results shown in Fig. 3.6 clearly contrast. The disparity in both values suggests that the particles observed in the SEM images are polycrystalline and composed of several small crystallites. SEM images with higher magnifications (Fig. 3.7 **b**) show no evidence of small grain boundaries to justify the assumption; however, the large width of the XRD peaks suggests that the crystallites are too small too small compared with the scale of the picture, in the order of a few tens of nanometers.

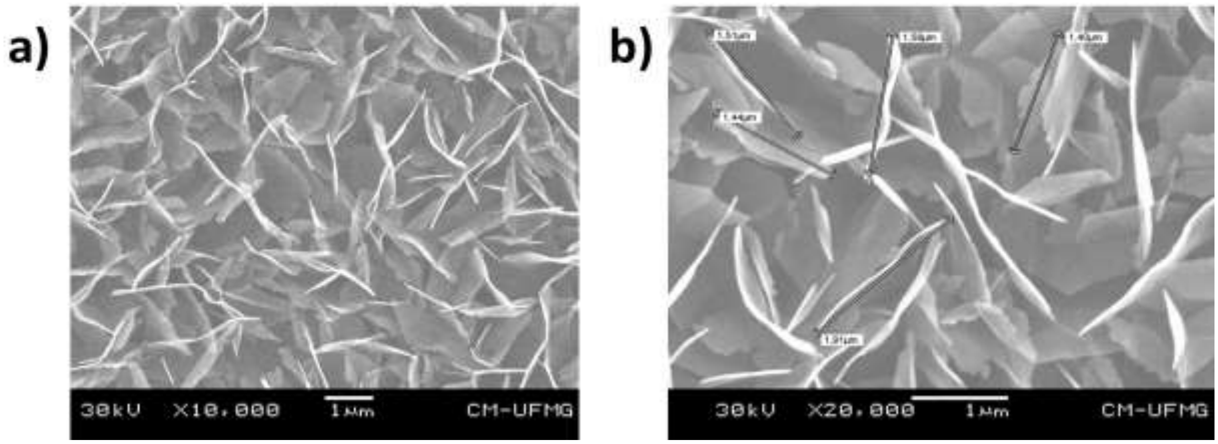

Fig. 3.7: **a)** SEM image of an iron sulfide film prepared by AACVD at 350 °C for 60 minutes, under 250 sccm of argon flow carrying an aerosol with a 2.67 mg/mL solution of FeDTC and Toluene; and **b)** SEM with the measure lengths of some tabular particles.

In order to study the reaction mechanism as well as pursue a single phase pyrite film, we deposited films at different temperatures. Higher temperatures increase the sulfur equilibrium fugacity of eq. 2.1, which would bias the reaction towards the formation of pyrrhotite, but also increase the decomposition of the FeDTC molecule. Lower temperatures favor pyrite formation, according to eq. 2.1, on the other hand, they diminish the kinetics of the decomposition of the reactant. Fig. 3.8 reveals, however, only pyrrhotite XRD peaks for samples prepared at 325 °C, 375 °C and 400 °C. At temperatures lower than 325 °C we did not observe any film growth, possibly due to lack of or minimal decomposition of the FeDTC molecule, which decomposes at temperatures close to 250 °C. The films presented the same microstructure of the film deposited at 350 °C, with big tabular particles randomly oriented with no significant changes other than the edges of the particles (Fig. 3.9), which became more irregular (circled areas) as the temperature increased.

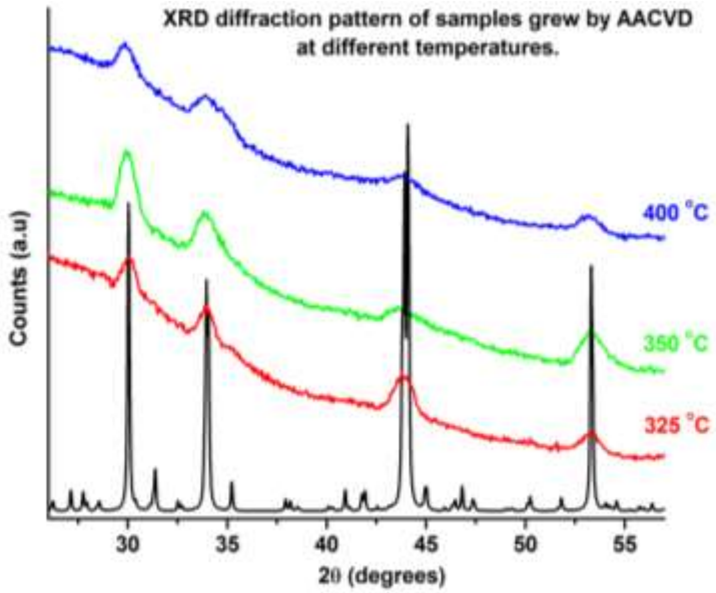

Fig. 3.8: XRD patterns of iron sulfide films deposited by AACVD in homemade reactor at different temperatures. Also shown the pyrrhotite reference data.

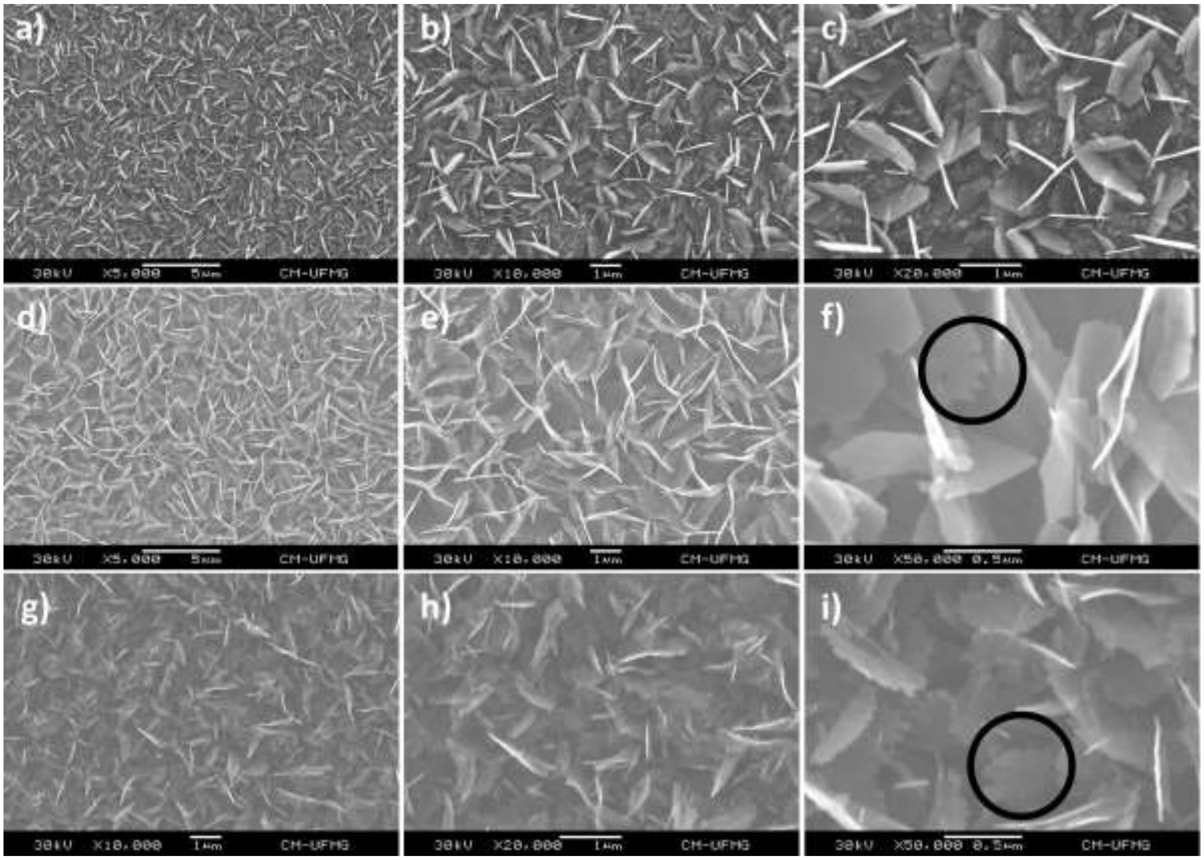

Fig. 3.9: SEM images of iron sulfide films deposited by AACVD at **a), b), c)** 325 °C, **d), e), f)** 350 °C, and **g), h), i)** 400 °C. The circles highlight the edges of the particles which became more irregular for increasingly temperature.

The value of the sulfur partial pressure achieved in our system was clearly lower than the equilibrium one, consequently favoring the formation of pyrrhotite. Thus, we attempted to increase the sulfur partial pressure above the substrates, in order to bias eq. 2.1 toward the formation of FeS_2, by using a more concentrated solution of the precursor. We prepared a solution with a concentration up to five times the starting value of 2.67 mg/ml, generating excess sulfur, due to the fact that the FeDTC molecule used in our work had an atomic ratio of Fe:S = 1:6. With the new and more concentrated solution, we deposited another series of samples varying the reaction temperature. The more concentrated solution resulted, as shown in Fig. 3.10, in a mix phase of pyrrhotite, pyrite and marcasite for the film deposited at the lowest temperature studied, 325 °C. At 350 °C and 400 °C, we obtained only pure phase pyrrhotite, with increasingly peak width, indicating a decrease in the particles size.

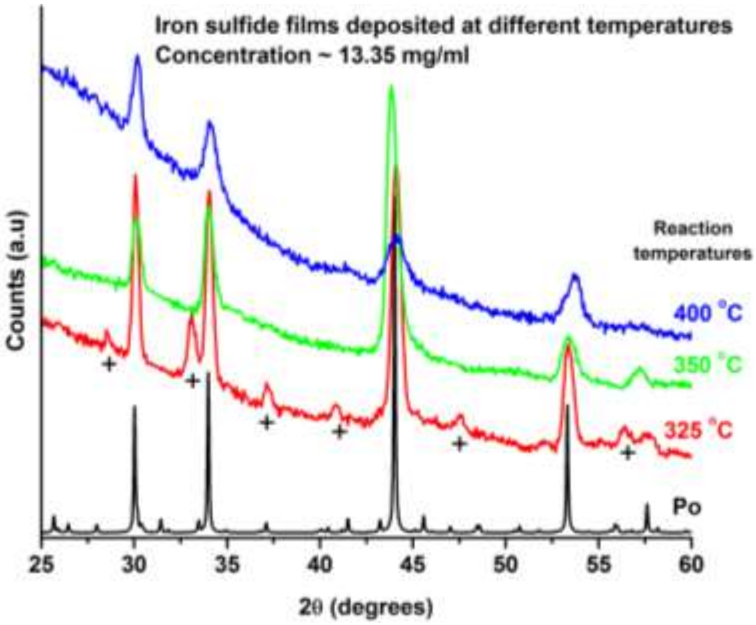

Fig. 3.10: XRD patterns of iron sulfide films prepared with a solution five times more concentrated, at different temperatures. Po represents the reference data for pyrrhotite, and the crosses index pyrite XRD peaks. The other peaks are related to marcasite. We observed a mix phase of pyrrhotite, pyrite, with traces of marcasite is observed at 325 °C; pyrrhotite with traces of marcasite at 350 °C; and a phase pure pyrrhotite film at 400 °C.

SEM images (Fig. 3.11) of the samples reveal different microstructures with a clear evolution trend, following the increase in the reaction temperature. The lowest temperature sample presented a dense agglomeration of thick plates, sometimes twinned at right angles, which became thinner as the temperature rose. In addition, the agglomeration of the plates became less dense and the plates became more transparent to the electron beam. The shrinkage of the plates thickness and consequent increase in their transparency indicate a possible decomposition reaction, which corroborates the idea stated earlier in this chapter, that the large plates observed at the surface of the films prepared by AACVD have, actually, FeS_2 composition, and, as the temperature rose, started to decompose into pyrrhotite. The comparison of the trend observed in the images depicted in Fig. 3.11 with the XRD composition analysis, also adds up to such idea regarding the real nature of the observed plates, although more profound chemical and structural analysis are needed. Nevertheless, the increase in the concentration of the solution was partially successful in obtaining pyrite films from AACVD, using our homemade reactor.

We attempted to further increase the concentration of the solution, however, we could not produce pure phase pyrite films with AACVD. Neither did we succeed in eliminating the pyrrhotite phase by varying other synthesis parameters, such as argon flow or reaction times. Therefore, we were forced to pursue an alternative method to increase the sulfur content in the produced films. We tested a few variations of sulfurization treatment on the iron sulfide films produced by AACVD, and, later, on spin-coated iron oxide films. In the next section we demonstrate the results obtained by each variation, and finally, we present the optimized apparatus implemented in the Laboratory of Nanomaterials of the Physics Department, reported for the first time in [21].

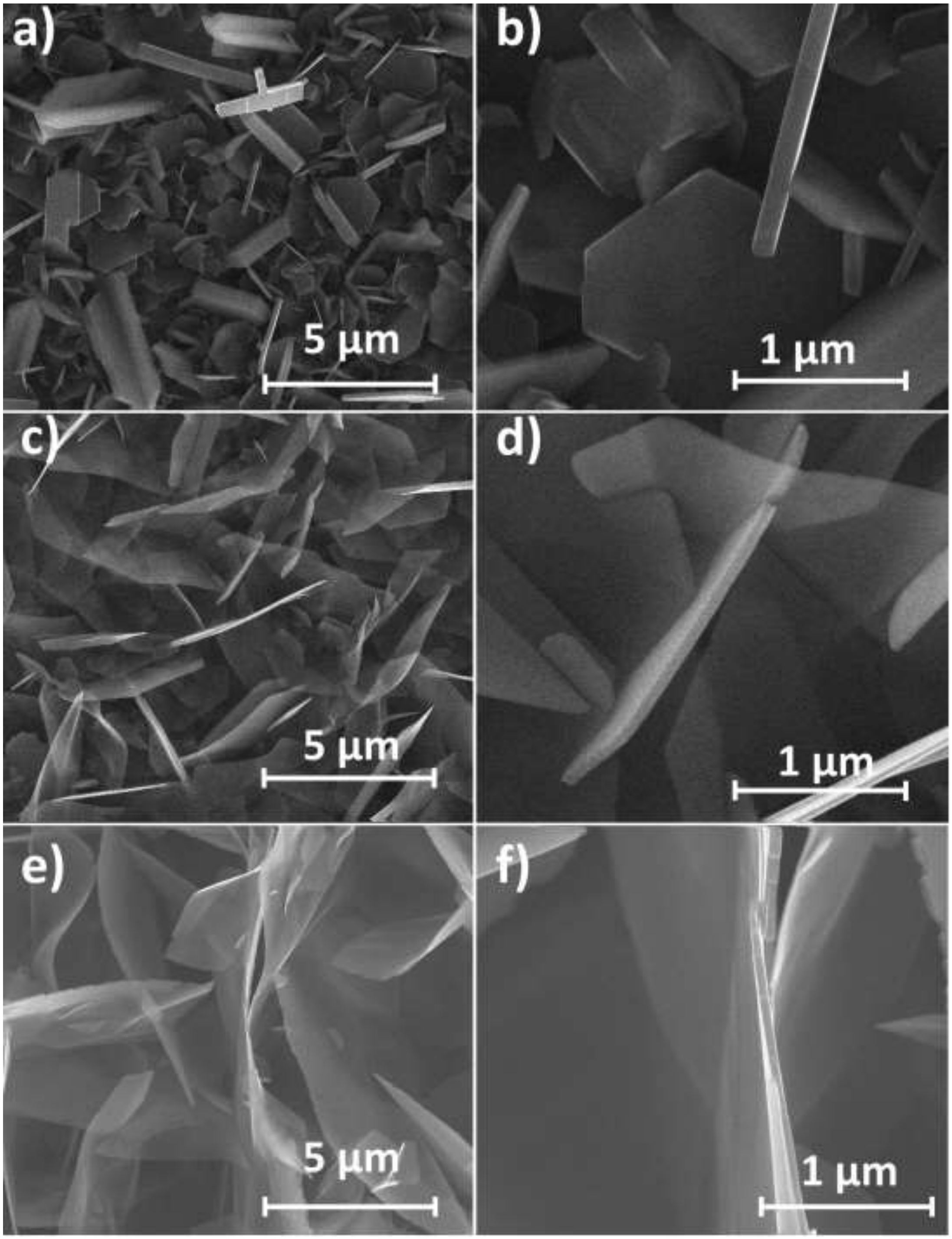

Fig. 3.11: SEM images of iron sulfide films prepared with a more concentrated solution of FeDTC at different temperatures. **a)**, **b)** At 325 °C, the films presented a dense agglomeration of thick plates, sometimes twinned at right angles; **c)**, **d)** at 350 °C, the agglomeration of plates became less dense as the plates became thinner, and more transparent to the electron beam; **e)**, **f)** At 400 °C, the agglomeration and the plates became even less dense, thinner and more transparent, suggesting the occurrence of a decomposition reaction.

3.3.3 – SULFURIZATION

According to eq. 2.1, when heated in a sulfur rich atmosphere, pyrrhotite (FeS_x) transforms into FeS_2. Such process of sulfur incorporation and phase transformation is identified in the literature as sulfurization [22,23,24,25], sulfidation [26,27] or even sulfuration [28,29,30]. There are two main methods used for sulfurization: ampoules and continuous low sulfur vapor flow. The use of ampoules, although advantageous because of the perfect sealing of the sulfur vapor, preventing exterior contamination and sulfur loss during the process, and the small amount of sulfur powder needed (typically, close to 1 mg), it cannot be reused, as the ampoules must be broken down after the process, in order to extract the sulfurized film. In addition, a special care must be taken in order to avoid sulfur condensation on the surface of the films during cooling [26,31]. The other method consists on heating the film on a tubular furnace with continuous sulfur flow, produced either by hydrogen disulfide, H_2S, which is highly toxic, or by heating sulfur powder at a temperature close to the melting point of sulfur. This later process usually involves greater amounts of sulfur powder and generates reasonable sulfur residuum. In order to overcome these drawbacks, we implemented an alternative sulfurization apparatus, which will be described in the following.

Firstly, we heated iron sulfide films, produced by AACVD, inside a stainless steel autoclave, filled with sulfur powder. The autoclave was placed open, with the films and sulfur powder inside, in a glove box, deoxygenated, and later sealed. Finally, it was transferred to a furnace and heated at 450 ^{o}C for three hours at a heating rate of 10 ^{o}C/min, in air. Fig. 3.12 shows the XRD patterns of the same films shown in Fig. 3.10, after being sulfurized in the autoclave. We noted that the pyrrhotite peaks have completely vanished in all samples, and intense pyrite (Pyr) and marcasite peaks (represented by crosses in the graph) have appeared. After the sulfurization process, when we withdrew the autoclave from the furnace, we noted that the copper O-ring, which seals the autoclave, had decomposed during the process. As a result of exterior oxygen contamination, magnetite peaks also appeared in the XRD pattern of Fig. 3.12, indicated by daggers in the graph. We also believe that the copper reacted with the inner sulfur vapor, producing copper sulfide and enhancing the decomposition of the O-ring.

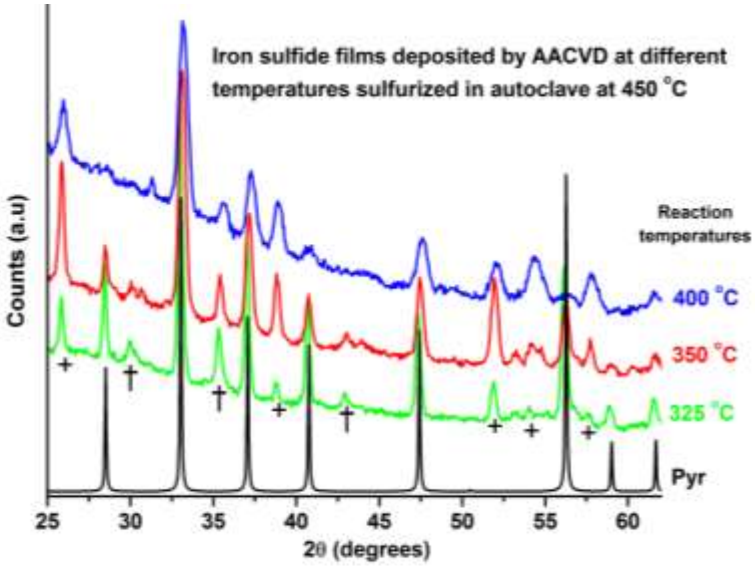

Fig. 3.12: XRD patterns of iron sulfide films deposited at different temperatures by AACVD and sulfurized in an autoclave at 450 °C. Every pyrrhotite signal from the precursor films vanished and intense pyrite and marcasite peaks (represented by crosses) were observed. We also observed peaks related to the iron oxide magnetite (indexed by daggers), which is commonly formed in environments with low oxygen concentration, due to the breaking seal of the autoclave as a result from the decomposition of the copper O-ring during the sulfurization process.

Fig. 3.13 reveals distinct microstructures of the sulfurized films, when compared with the precursor iron sulfide films (which are also depicted in Fig. 3.11) deposited by AACVD. After sulfurization, the plates previously observed in the iron sulfide films became filled with cuboid particles, roughening their otherwise smooth surface. Correlating with the XRD results, such particles are associated with the formation of pyrite during sulfurization. The assumption stem from the similar behavior regarding the decline of the pyrite XRD peaks for increasingly AACVD reaction temperature, and the also diminishing concentration of particles on the surface of the plates for higher reaction temperatures. The morphology of the plates, though, remained roughly unchanged, however, their composition, may also have changed into FeS_2, since the marcasite phase is widely present in the films (Fig. 3.12), and whose symmetry commonly results in tabular shaped crystals.

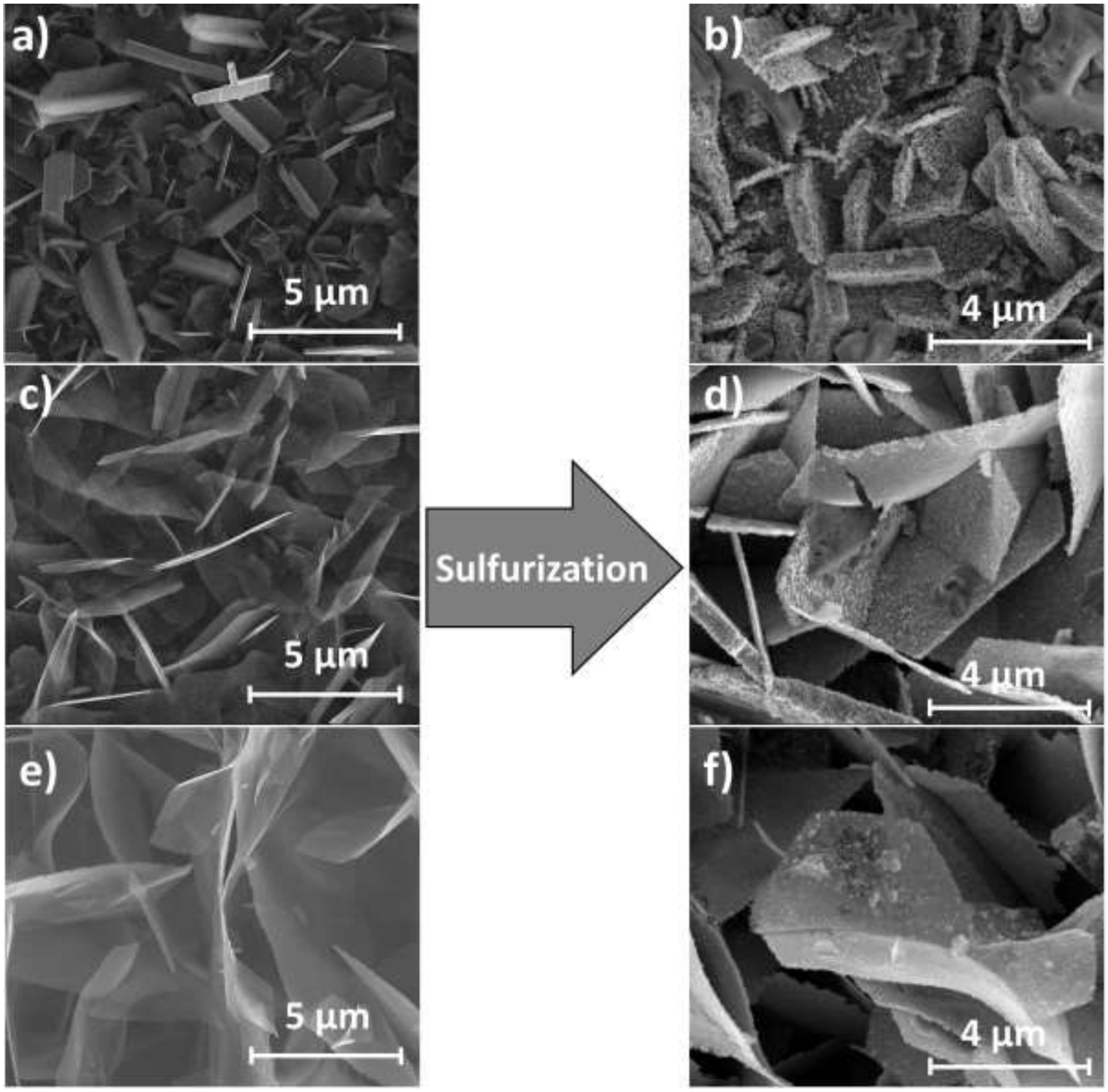

Fig. 3.13: SEM images of iron sulfide films deposited by AACVD at different temperatures: **a)** 325 °C, **b)** 350 °C, and **c)** 400 °C; and sulfurized in an autoclave at 450 °C.

Although we obtained promising results sulfurizing films inside an autoclave, we could not prevent the copper O-ring from reacting with either the exterior oxygen, nor with the inner sulfur. Neither did we find a good replacement material to seal the autoclave, thus we decided to try a different approach, consisting in the use of small glass tubes to enclose sulfur vapor produced from heating sulfur powder.

Primarily, the apparatus consisted on a single glass tube loaded with a pyrrhotite film and sulfur powder, placed inside a conventional fused silica tube, rinsed with argon, and heated on a tubular furnace, under constant argon flow. In the first tests, we place the sulfur powder on the surface of the pyrrhotite films, and heated the system in a two stage process: **i)** first at a temperature close to the melting point of S (~ 115 ^{o}C) for 20 min to allow the material to melt and uniformly coat the surface of the films; **ii)** then, at temperatures close to the boiling point of S (~445^{o}C) to trigger a phase transformation of pyrrhotite into pyrite. We sulfurized different samples deposited by AACVD in the same conditions, varying only the reaction time of the second stage. Fig. 3.14 shows that, although the pyrrhotite films were successfully transformed into FeS_2, the composition of the films presented both polymorphs, marcasite and pyrite, with a dominance of the first one. Moreover, for the sample with the longest reaction time (1 hour), the reverse reaction started to occur, as pyrrhotite was once again observed, mixed with the marcasite phase. Therefore, there was an urge to enclose the system to assure a sulfur rich environment for reasonable periods of time, and prevent sulfur vapor pressure from dropping down to values below the equilibrium of eq. 2.1. We also tested placing the sulfur powder freely on the inner tube to sulfurize an iron oxide film, prepared by spin coating. The iron oxide films was heated at 450 ^{o}C in a one stage process only for 40 min. The XRD result depicted in Fig. 3.15 corroborates the first findings – regarding the sulfurization with sulfur on the surface of the films – which indicated a significant sulfur loss during the process, as no trace of FeS_2, or any other iron sulfide was observed. Ergo, the sulfur vapor decreased rapidly during the process, biasing eq. 2.1 to the left towards de formation of iron oxide. The presence of the magnetite Fe_3O_4 indicates the presence of a low oxygen pressure inside the system, leading to the oxidation of the recently formed FeS_2 particles. Therefore, we needed to improve the enclosing of the system in order to assure a sulfur rich environment for longer times, and completely transform pyrrhotite or iron oxide into pure phase pyrite (FeS_2), and preventing the occurrence of the inverse reaction.

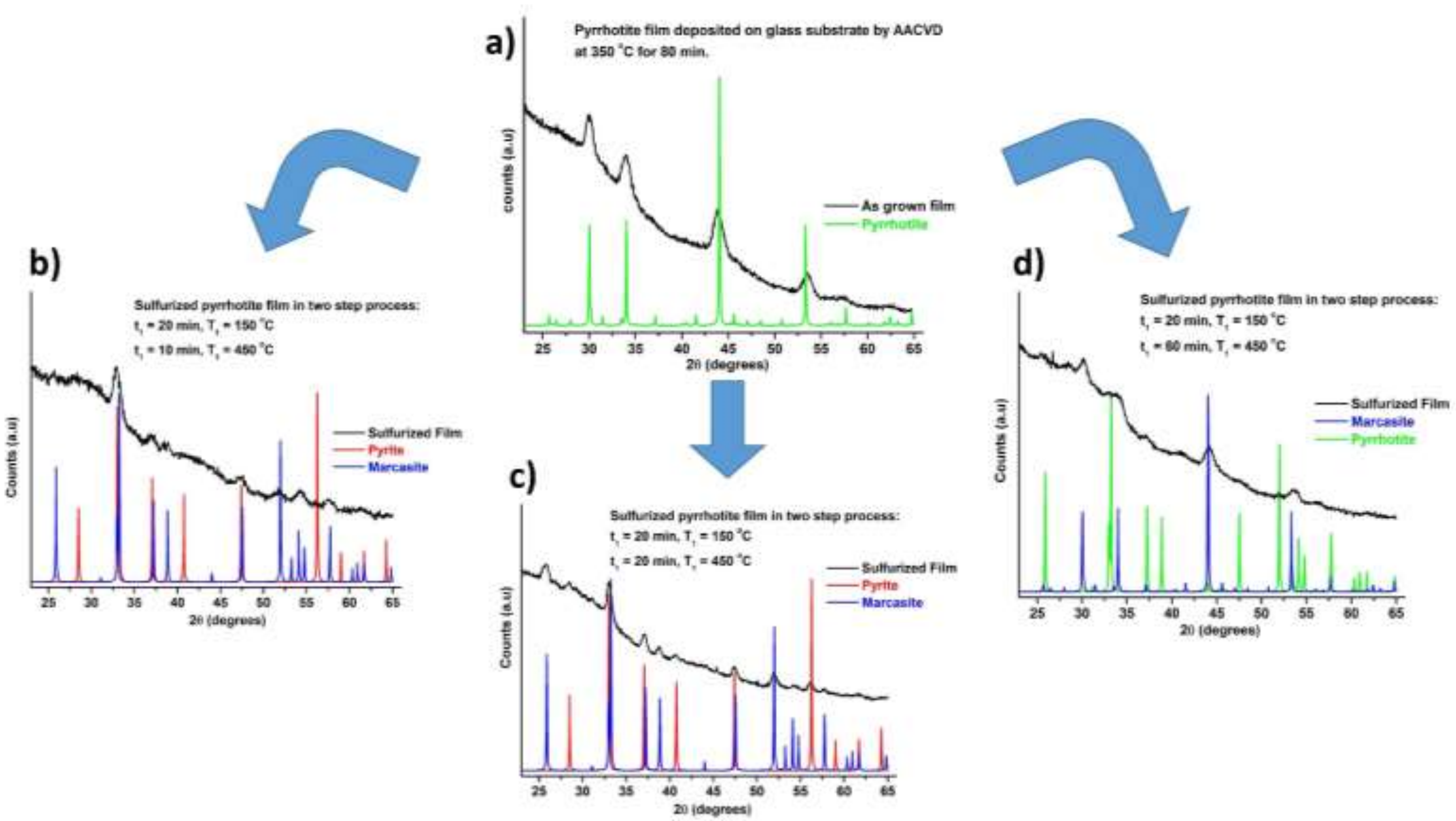

Fig. 3.14: XRD pattern of pyrrhotite films prepared at the same conditions in the homemade AACVD reactor, and sulfurized in a two stage process. The first stage was kept constant for all samples, whereas in the second stage, the samples were annealed at 450 ºC for a) 10 min, b) 20 min, and c) 60 min.

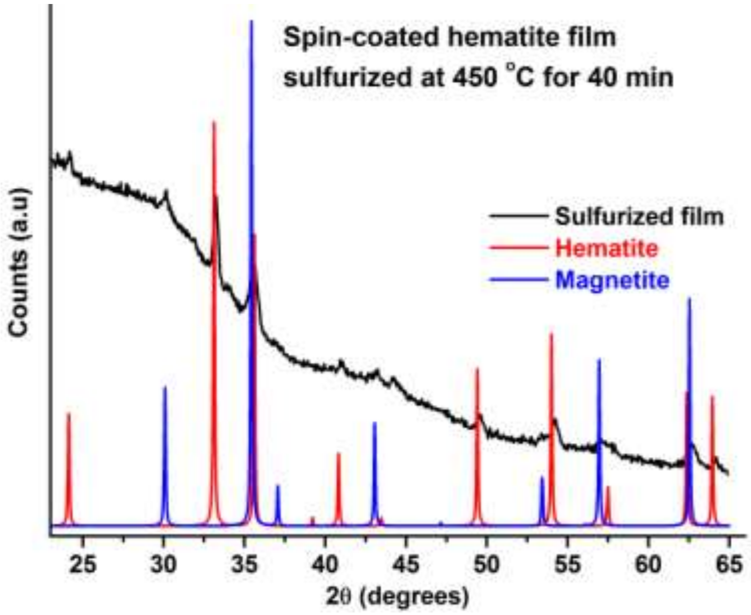

Fig. 3.15: XRD pattern of a spin coated hematite (Fe_2O_3) film sulfurized at 450 °C for 40 min. No trace of FeS_2 was observed, indicating the rapid decrease in the sulfur vapor pressure in the system. The presence of the magnetite (Fe_3O_4) indicates a low oxygen pressure in the system.

3.4 – NEW RUSSIAN DOLL SULFURIZATION APPARATUS

In order to prevent the observed rapid decrease in sulfur vapor partial pressure in our sulfurization apparatus, we added 3 more tubes, each slightly larger than the other. The sulfurization process occurred, thus, as follows. First, we place sulfur powder inside a glass tube (tube 1) and a pyrrhotite or hematite thin film inside another slightly larger glass tube (tube 2) [Fig. 3.16(A)]. Both tubes are placed inside a deoxygenating chamber[1] with a third and fourth tubes (tubes 3 and 4, respectively), each slightly larger than the previous ones. The dimensions of the tubes are displayed on the right side of Fig. 3.16. The third and fourth tubes increase the enclosing of the system, providing a quasi-stationary sulfur environment during the sulfurization process.

---

[1] The deoxygenating chamber consists on a plastic bag with two hose connections. The first one is connected to a N_2 gas line, which inflates the plastic bag, whereas the other one is left open. Thus, after being inflated, one may gently press the bag in order to evacuate the air inside.

Then, the system is rinsed with a continuous nitrogen flow for approximately 10 minutes in order to assure an inert atmosphere inside the Russian Doll tube set. After that, the tubes are nested yet inside the deoxygenating chamber [Fig. 3.16(B)] and transferred to a fused silica tubular furnace under 1000 sccm of argon flow [Fig. 3.16 (C)]. The tube set is heated up to different sulfurization temperatures (T_S) for different times (t_S) under a constant argon flow of 500 sccm (note that the argon flow is used here only to prevent oxygen from outside the furnace to enter the tube set, and contaminate the films, hence, there is no argon flow inside the Russian Doll apparatus), and then allowed to cool down naturally.

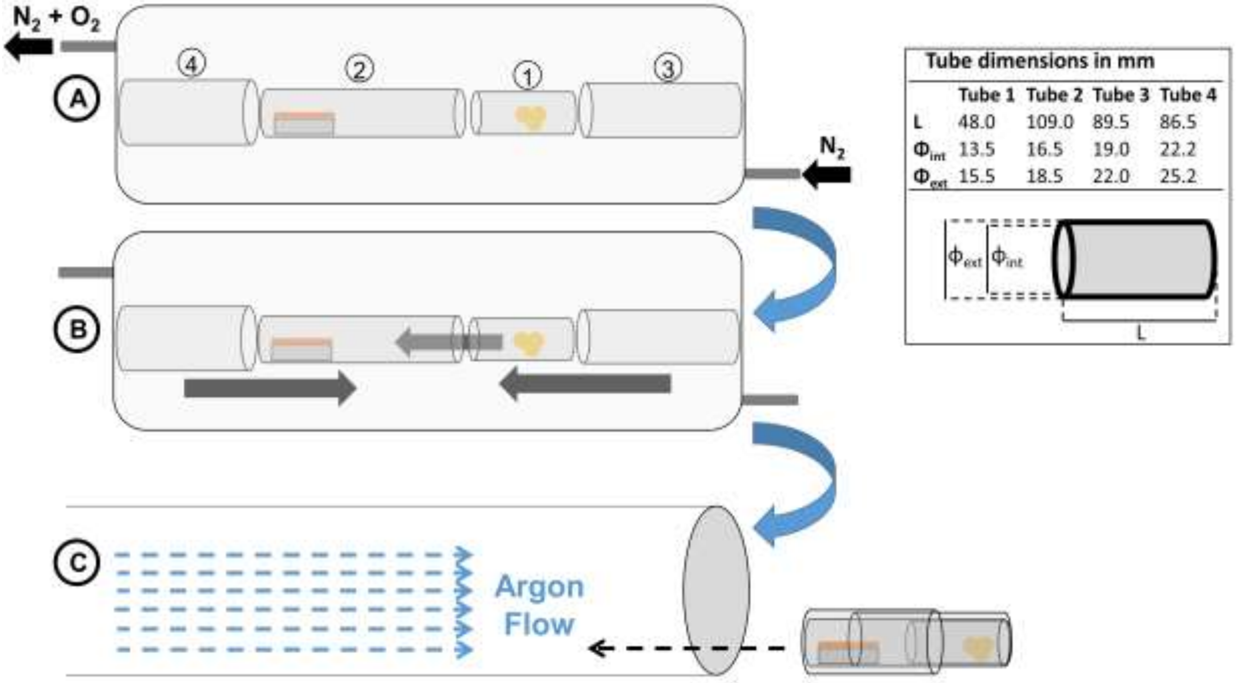

Tube dimensions in mm

	Tube 1	Tube 2	Tube 3	Tube 4
L	48.0	109.0	89.5	86.5
Φ_{int}	13.5	16.5	19.0	22.2
Φ_{ext}	15.5	18.5	22.0	25.2

Fig. 3.16: Scheme illustrating the procedure to sulfurize films with the Russian Doll set up. Details are discussed in the text.

The first test using the new Russian Doll apparatus was performed on a spin-coated hematite film, oxidized at 500 °C and later sulfurized at 550 °C, for 60 minutes, with 15 mg of sulfur powder. As shown in Fig. 3.17, only pyrite XRD peaks, with no traces of iron oxides, were observed after sulfurization, indicating that the transformation reaction (eq. 2.1) was successfully completed. Moreover, no traces of any other iron sulfide phases were observed, not even the FeS_2 polymorph, marcasite.

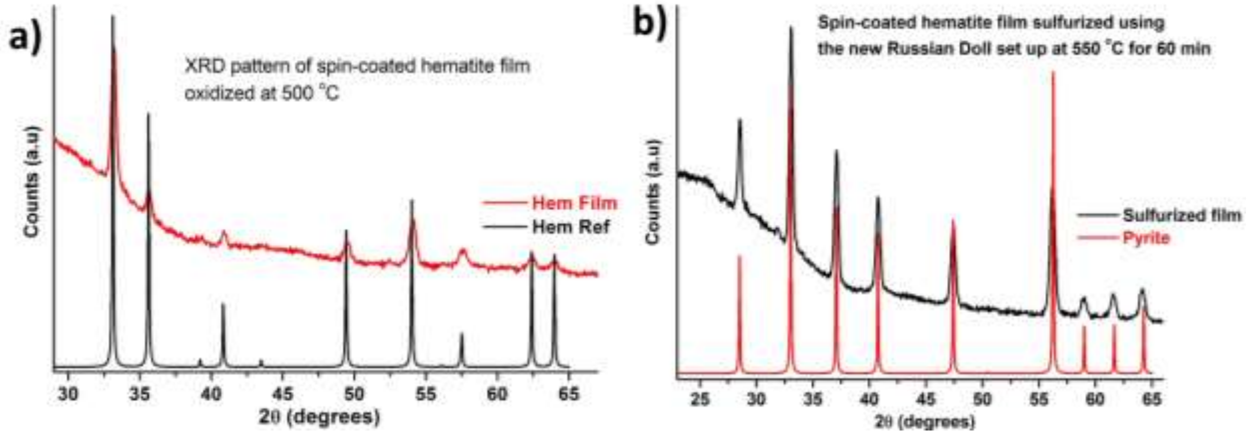

Fig. 3.17: XRD pattern of a spin-coated hematite film **a)** before and **b)** after sulfurization with the Russian Doll set up. Only pyrite peaks are observed. “Hem Ref” and “Pyrite” refer to the reference XRD data from hematite and pyrite, respectively.

Following the success obtained with the Russian Doll apparatus, we prepared a study regarding the synthesis of pyrite films by sulfurization of hematite films prepared by spin coating. Fig. 3.18 illustrates the three-step process evidencing the synthesis parameters that were explored during the work, whose results regarding the properties of the resulting films will be presented in the following chapter. First, a 0.5 M solution of iron (III) nitrate nonahydrate – $(FeNO_3)_3.9H_2O$ – and ethanolamine [$H_2N(CH_2)_2OH$, Sigma Aldrich] in 2-methoxyethanol [$HO(CH_2)_2OCH_3$] is spin coated on a glass (quartz) substrate and heated at 300 ^oC for 10 min, following a procedure adapted from the literature regarding the production of zinc oxide films [32]. Then, the resulting amorphous film (a-hydroxide) is oxidized at a temperature T_O, for a time t_O. Finally, the Fe_2O_3 film is sulfurized with the Russian Doll apparatus, using different amounts of sulfur m_S, at different sulfurization temperatures T_S, for different times t_S. The first step (spin coating) had been already optimized for the deposition of Fe_2O_3 and was not analyzed in this work.

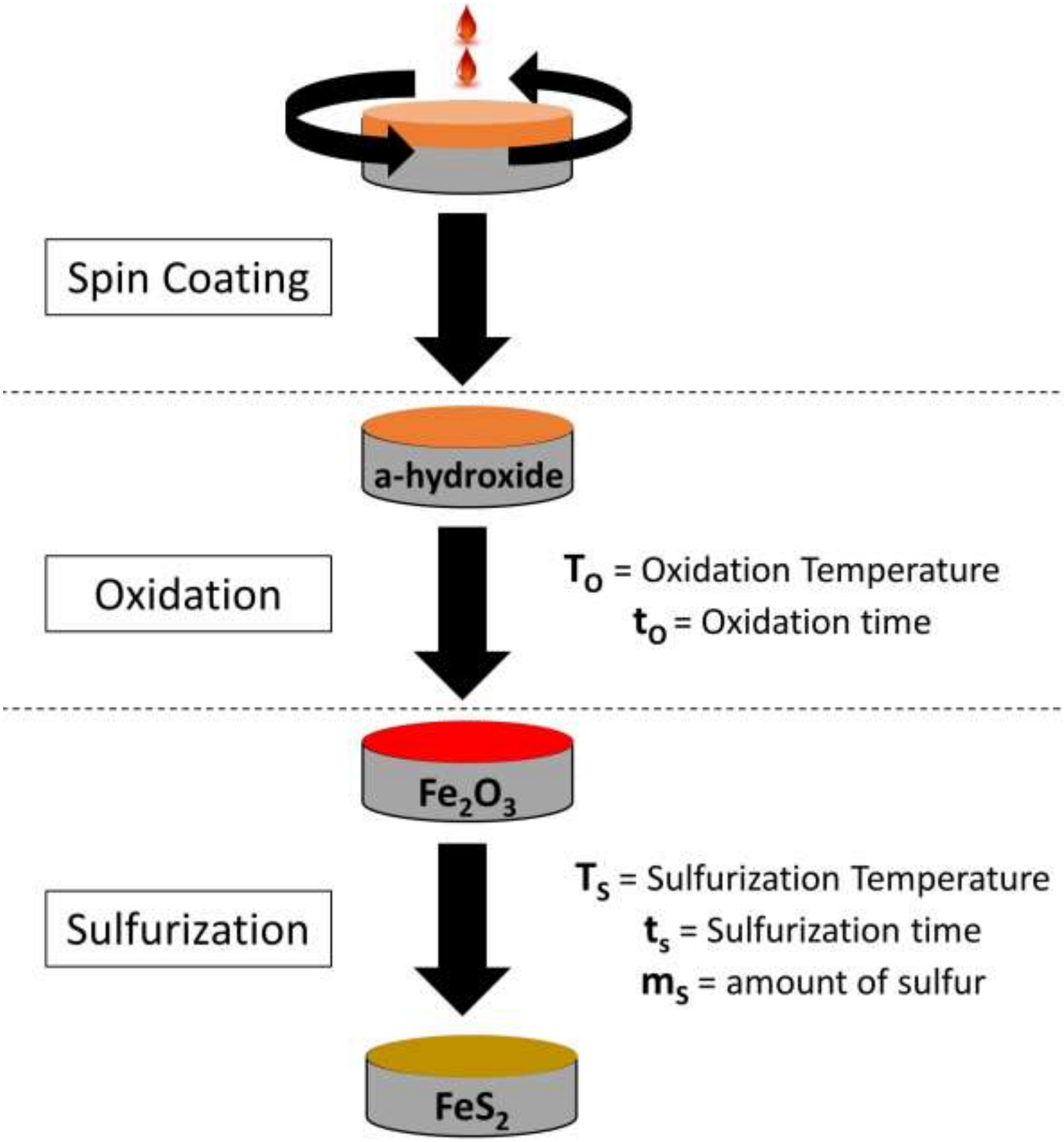

Fig. 3.18: Scheme illustrating the three-step process used in the work to study the growth of iron pyrite films, evidencing the synthesis parameters studied. The spin coating parameters were optimized prior to this work.

The sulfurized films – prepared by the method illustrated in Fig. 3.18 – presented great adhesion, specular reflectivity and dark golden color, in contrast with the films produced by AACVD, which had poor adhesion, were opaque and had black color. Moreover, the SEM images displayed in this chapter evidence that the AACVD deposited films are not continuous, and, consequently, will not have favorable electric properties. Therefore, we did not produce further films by AACVD in this work.

References

---

1 http://www.rigaku.com.
2 H. Fujiwara, Spectroscopic Ellipsometry: Principles and Applications, (2007) Tokyo, Japan: John Wiley & Sons
3 J.M.D. Coey, Magnetism and Magnetic Materials, (2010) Cambridge, UK: Cambridge University Press
4 L.J. Pauw, Philips Research Report **20** (1958) 220
5 G.M. de Lima, D.C. Menezes, C.A. Cavalcanti, J.A.F. dos Santos, I.P. Ferreira, E.B. Paniago, J.L. Wardell, S.M.S.V. Wardell, K.Krambrock, I.C. Mendes, H. Beraldo, J. Mol. Struct. **988** (2011) 1
6 G.O. Siqueira, A.O. Porto, M.M. Viana, H.V. da Silva, Y.G. de Souza, H.W.A. da Silva, G.M. de Lima, T. Matencio, Phys. Chem. Chem. Phys. **15** (2013) 16236
7 G.O. Siqueira, T. Matencio, H.V. da Silva, Y.G. de Souza, J.D. Ardisson, G.M. de Lima, A.O. Porto, Phys. Chem. Chem. Phys. **15** (2013) 6796
8 I.P. Ferreira, G.M. de Lima, E.B. Paniago, C.B. Pinheiro, J.L. Wardell, S.M.S.V. Wardell, Inorg. Chim. Acta **441** (2016) 137
9 G.A.A. Costa, M.C. Silva, A.C.B. Silva, G.M. de Lima, R.M. Lago, M.T.C. Sansiviero, Phys. Chem. Chem. Phys. **2** (2000) 5708
10 D.C. Menezes, G.M. de Lima, F.A. Carvalho, M.G. Coelho, A.O. Portob, R. Augusti, J.D. Ardisson, Appl. Organometal. Chem. **24** (2010) 650
11 D.C. Menezes, G.M. de Lima, A.O. Porto, C.L. Donnici, J.D. Ardisson, A.C. Doriguetto, J. Ellena, Polyhedron **23** (2004) 2103
12 M. Akhtar, A.L. Abdelhady, M.A. Malik, P.O`Brien, J. Cryst. Growth **346** (2012) 106
13 Q. Tang, H. Albers, A. Driessen, L.T.H. Hilderink, P.V. Lambeck, TH.J.A. Popma, J. Aerosol Sci. **21** (1990) 737
14 K.V. Salazar, K.C. Ott, R.C. Dye, K.M. Hubbard, E.J. Peterson, J.Y. Coulter, Physica C **198** (1992) 303
15 B. Kim, S.G. Ansari, Y. Kim, G. Kim, S. Hwang, H. Lee, H. Shin, Korean J. Chem. Eng. **20** (2003) 772
16 C. Piccirillo, R. Binions, I.P. Parkin, Eur. J. Inorg. Chem. **2007** (2007) 4050
17 G. Walters, I.P. Parkin, Appl. Surf. Sci, **255** (2009) 6555
18 T. Stoycheva, S. Vallejos, J. Calderer, I. Parkin, C. Blackman, X. Correig, Procedia Engineering **5** (2010) 131
19 M.G. Nolan, J.A. Hamilton, S. O'Brien, G. Bruno, L. Pereira, E. Fortunato, R. Martins, I.M. Povey, M.E. Pemble, J. Photoch. Photobio A **219** (2011) 10
20 M.A. Ehsan, A.A. Tahir, M. Hamid, M. Mazhar, K.G.U. Wijayantha, M. Zeller, Inorg. Chim Acta **376** (2011) 189
21 M.F.O. Silva, L.P. Souza, S. de Oliveira, A.S. Ferlauto, W.N. Rodrigues, Thin Solid FIlms 616 (2016) 303
22 S. Bausch, B. Sailer, H. Keppner, G. Willeke, E. Bucher, G. Frommeye, Appl. Phys. Lett. **57** (1990) 25
23 G. Smestad, A. Ennaoui, S. Fiechter, H. Tributsch, W.K. Hofmann, M. Birkholz, W. Kautek, Sol. Energy Mater. **20** (1990) 149
24 F. Wang, L. Huang, Z. Luan, J. Huang, L. Meng, Mater. Chem. Phys. **132** (2012) 505
25 J.M. LaForge, B. Gyenes, S. Xu, L.K. Haynes, L.V. Titova, F.A. Hegmann, M.J. Brett, Sol. En. Mater. **117** (2013) 306
26 X. Zhang, M. Manno, A. Baruth, M. Johnson, E.S. Aydil, C. Leighton, ACS Nano **7** (2013) 2781
27 M. Cabán-Acevedo, D. Liang, K.S. Chew, J.P. DeGrave, N.S. Kaiser, S. Jin, ACS Nano **7** (2013) 1731
28 I.J. Ferrer, C. De las Heras, C. Sánchez, Appl. Surf. Sci. **70/71** (1993) 588
29 D. Wan, B. Wang, Y. Wang, H. Sun, R. Zhang, L. We, J. Cryst. Growth **257** (2003) 286
30 N. Hamdadou, A. Khelil, J.C. Bernède, Mater. Chem. Phys. **78** (2003) 591
31 X. Zhang, M. Manno, A. Baruth, M. Johnson, E.S. Aydil, C. Leighton, ACS Nano **7** (2013) 2781
32 J. Downing, M.P. Ryan, N. Stingelin, M.A. McLachlan, J. Photonics for Energy **1** (2011) 011117-1

4 Pyrite: Results and Discussion

In this chapter, we present the results regarding the synthesis of FeS_2 by means of the Russian Doll sulfurization method implemented in the lab. First, we present the results on the deposition of FeS_2 films prepared with different synthesis parameters, and analyze the influence of the synthesis parameters on the phase composition and microstructure of the resulting iron pyrite films. Then we analyze the influence of the properties of the precursor iron oxide films in the resulting FeS_2 films. Later, we discuss the results based on reaction models for iron pyrite, presented briefly in chapter 2.

4.1 RESULTS

As mentioned in the previous chapter, we prepared films of FeS_2 via a three-step process, by sulfurizing spin-coated hematite films. The sulfurization process was carried out using the Russian Doll apparatus (illustrated in Fig. 3.16) implemented in the lab, and the phase composition and microstructure of the pyrite films were correlated with the different synthesis parameters, listed in Fig. 3.18. In the following sections, we detail every series of samples we prepared varying synthesis parameters.

Series with varying sulfurization temperature

Firstly, we prepared spin-coated hematite films, annealed at 500 ^{o}C for 30 minutes, and sulfurized at 450 ^{o}C, 500 ^{o}C, and 550 ^{o}C, for 60 minutes with 15 mg of sulfur powder. All films were grown on soda lime glass substrates, and the heating rate was kept at 10.5 ^{o}C/min. XRD patterns of the films, depicted in Fig. 4.1, unveil the presence of both FeS_2 polymorphs, pyrite and marcasite (indexed by “M” in the graphs), with an increasing dominance of pyrite, for increasing T_S. The presence of the marcasite polymorph is commonly observed amongst pyrite films as reported by other authors [1,2]. The peaks indicated by asterisks are artifacts produced by the diffractometer, and no traces of iron oxides or other iron sulfides were observed.

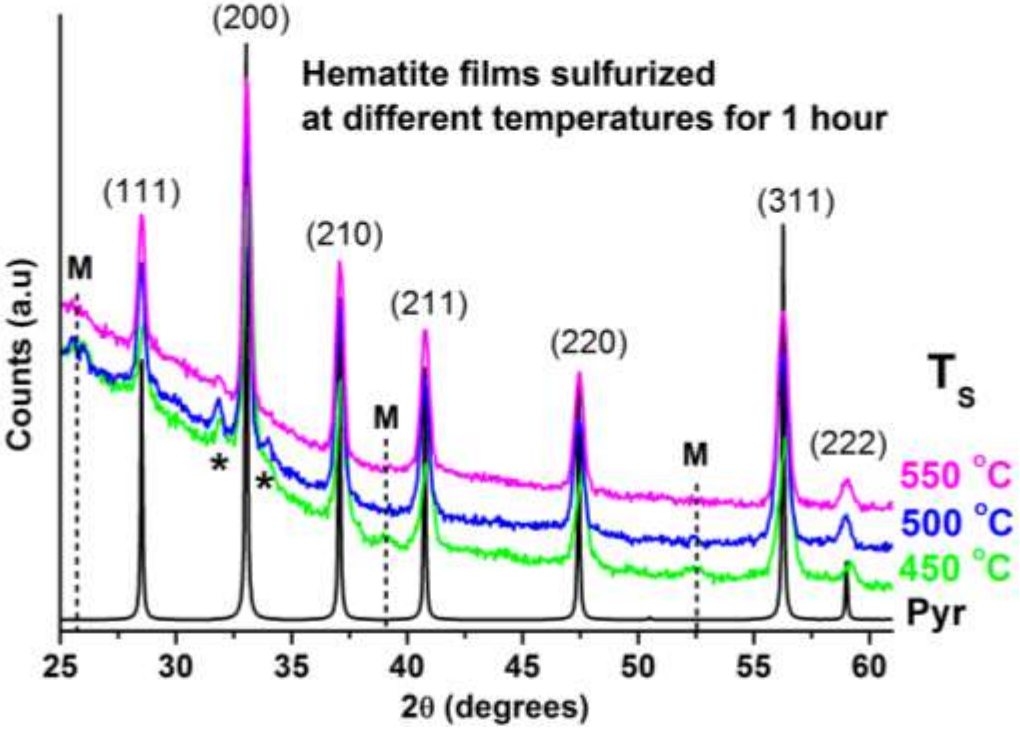

Fig. 4.1: XRD patterns of pyrite films sulfurized at 450 °C, 500 °C, and 550 °C. The "M" represents peak positions of the marcasite polymorph and the asterisks represent artifacts generated by the equipment.

SEM images (Fig. 4.2) clearly show two distinct crystal habits present in the samples: tabular and cuboid, which are associated with the two different FeS_2 phases. The first crystal habit (tabular) is typical of the orthorhombic marcasite, whereas the second one (cuboid) is typical of the cubic pyrite [3]. Hence, the SEM images complement the XRD results, indicating the presence of both polymorphs in all the samples, whereas XRD was not capable of detecting marcasite in the highest T_S sample. Moreover, SEM indicates that the presence of marcasite is more pronounced than suggested by the intensities of the XRD peaks, and that it decreases for higher T_S, given by the decrease in the concentration of the tabular particles. The last observation is in accordance with the XRD results.

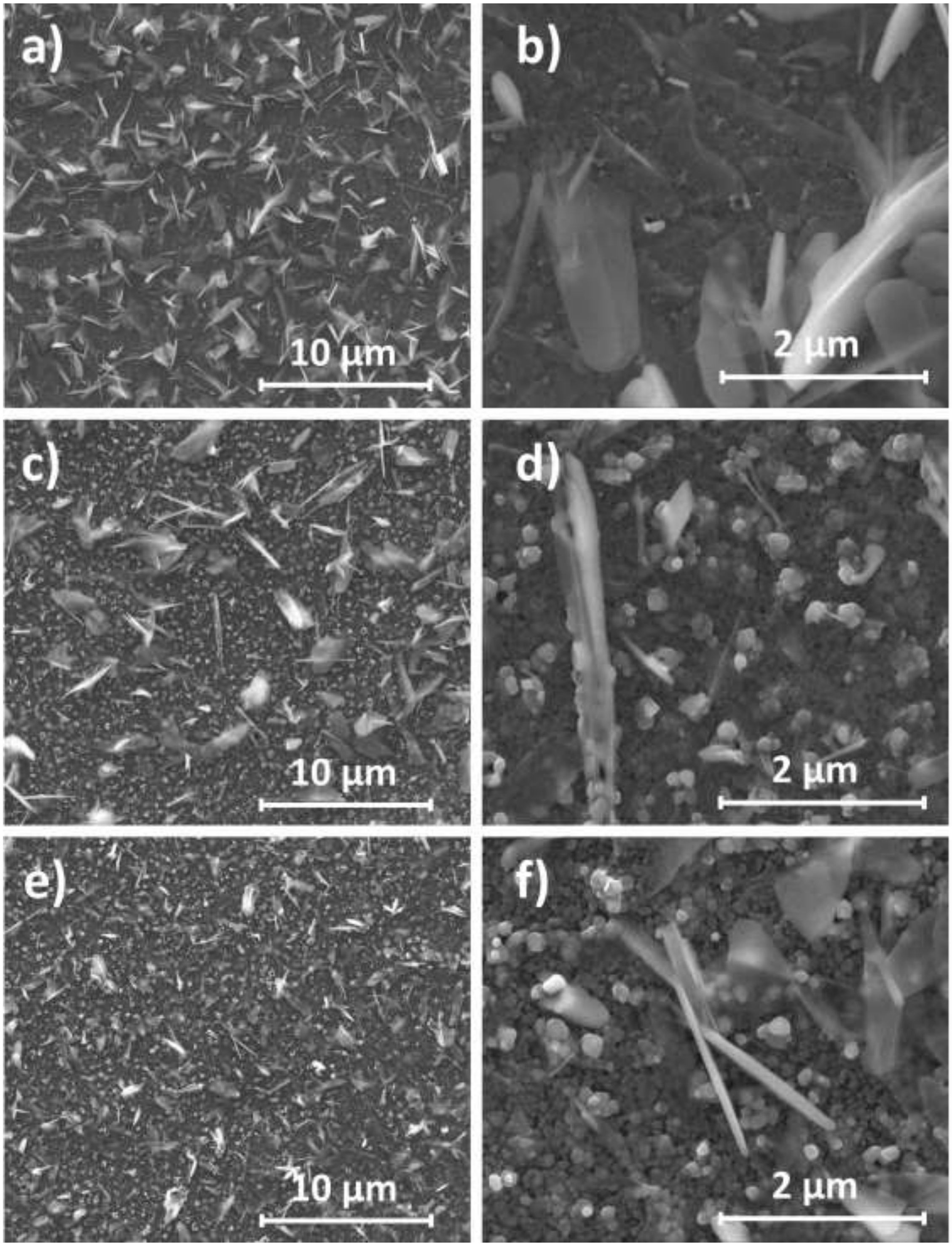

Fig. 4.2: SEM images of films sulfurized at **a)**, **b)** 450 °C; **c)**, **d)** 500 °C; and **e)**, **f)** 550 °C. We see two distinct crystal habits associated with the two FeS_2 polymorphs pyrite (cuboid, smaller particles) and marcasite (tabular, larger particles). The presence of marcasite seems do diminish as T_S increases, as observed in XRD.

Series with varying sulfurization time

We could not obtain a phase pure pyrite film by varying the sulfurization temperature only. However, the film prepared at 550 °C showed no marcasite peaks and the least concentration of tabular particles. Therefore, another series of samples was prepared at the optimum temperature 550 °C, and varying the sulfurization time, in order to transform the remaining marcasite structures into pyrite. This transformation reaction was presented in chapter 2 and follows eq. 2.1. Hematite films, prepared in the same conditions as before (annealed at 500 °C for 30 min) were, then, sulfurized at 550 °C for 30 min, 60 min, 120 min, and 240 min. Fig. 4.3, depicts the XRD patterns of all the samples. All the patterns show the same peaks identified as the planes (111), (200), (210), (211), (220), and (311) of pyrite. The patterns of all the films are equal except for minor, and not significant, differences in intensities. Although we observed little effect of increasing t_S with XRD, the SEM images on Fig. 4.4 unveils distinct microstructures.

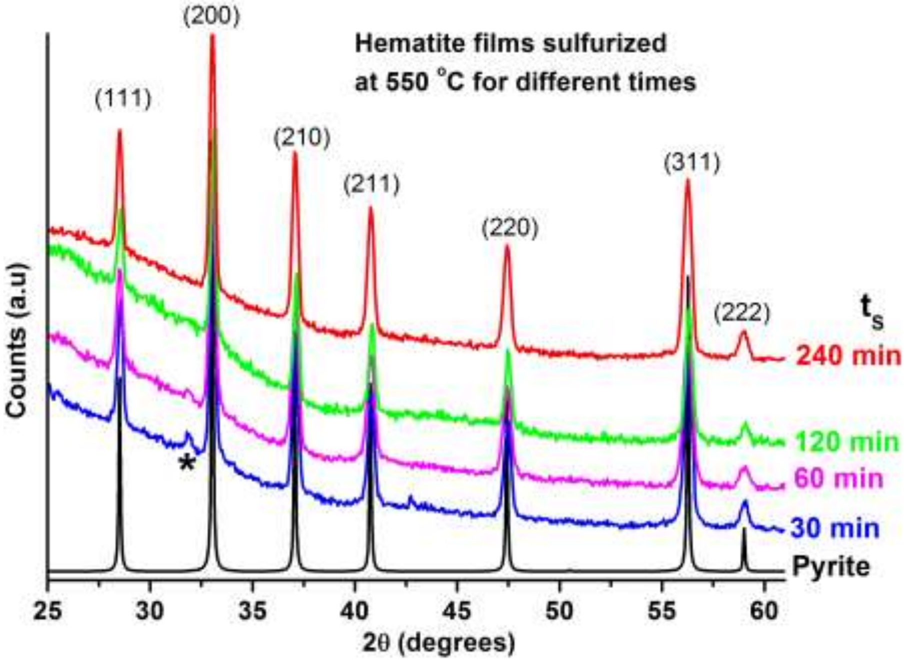

Fig. 4.3: XRD patterns of samples sulfurized for different times. We did not verify the presence of different phases.

As shown in the SEM images, there is an evolution in the microstructure of the films, from a mix of the two crystal habits previously seen in the low T_S series – tabular and cuboid – to a pure single phased cuboid structure for the longest t_S sample (240 min). This suggests that, even though we could not identify the presence of marcasite by XRD, both FeS_2 polymorphs are indeed present in every sample, except in the one sulfurized for 4 hours, and that the tabular particles are, most likely, amorphous.

The t_S series established, thus, a set of parameters to obtain phase pure pyrite films, ergo, T_S = 550 °C and t_S = 240 min. Moreover, such phase pure pyrite film presented **n**-type conductivity, with a resistivity of 1,04 Ωcm and a carrier concentration of $7{,}0 \times 10^{19}$ cm^{-3}, as determined by hall effect measurements performed using the Van der Pauw method.

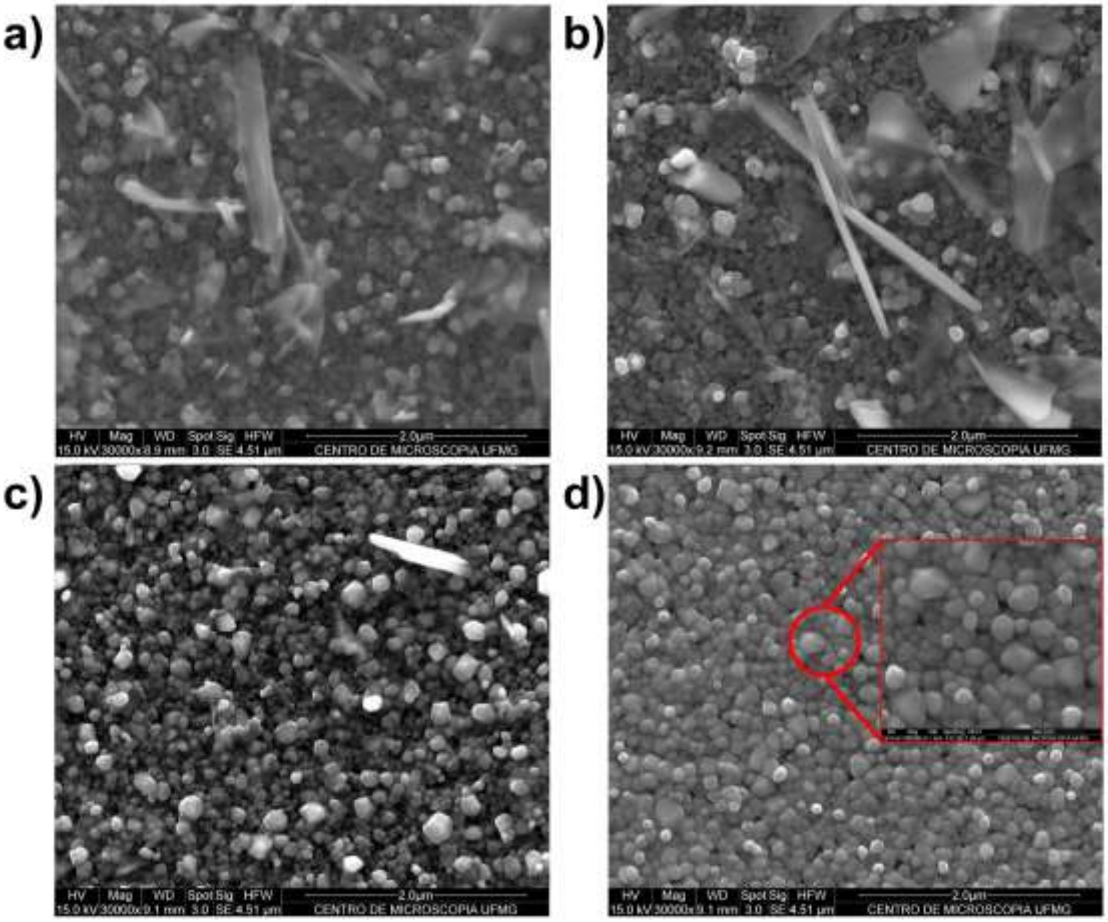

Fig. 4.4: SEM images of samples sulfurized at 550 °C for a) 30 min, b) 60 min, c) 120 min, and d) 240 min. The presence of the tabular crystal habit, associated with the marcasite polymorph, decreases for increasing t_S, untill it vanishes for t_S = 240 min.

Having established a route to obtain phase pure pyrite films, we attempted to increase the grain size of the films, by further increasing the sulfurization temperature and times. Moreover, we also investigated the influence of the microstructure of the precursor iron oxide films in the microstructure of the resulting FeS_2 films, by varying the oxidation temperatures and times, T_O, and t_O, respectively. Due to the high temperatures used during some processes, the films were deposited on fused silica substrates, and a new set of tubes, made of fused silica, was used for sulfurization. First, we will present the results for longer t_S and higher T_S.

Longer sulfurization times and higher sulfurization temperatures

We succeeded in obtaining a phase pure pyrite film, sulfurizing hematite films at 550 ^oC for 4 hours. In an attempt to promote crystal growth, we produced samples at temperatures higher than 550 ^oC, namely, 700 ^oC and 850 ^oC, and for longer periods of time, namely, 8 and 16 hours. The samples produced with longer sulfurization times were also used to determine an enclosing limit for our Russian Doll system, *i.e*, gave an estimate for how long our system was able to withhold the sulfur vapor inside the tubes.

Fig. 4.5 shows the XRD patterns of iron oxide films (annealed at 550 ^oC for 30 minutes), sulfurized at 700 ^oC and 850 ^oC for 4 hours. Both samples present XRD peaks of marcasite, the orthorhombic phase of FeS_2, represented by dotted lines. Moreover, the pattern of the sample sulfurized at 850 ^oC showed traces of pyrrhotite – indicated by crosses – and the intensity of the marcasite peaks decreased.

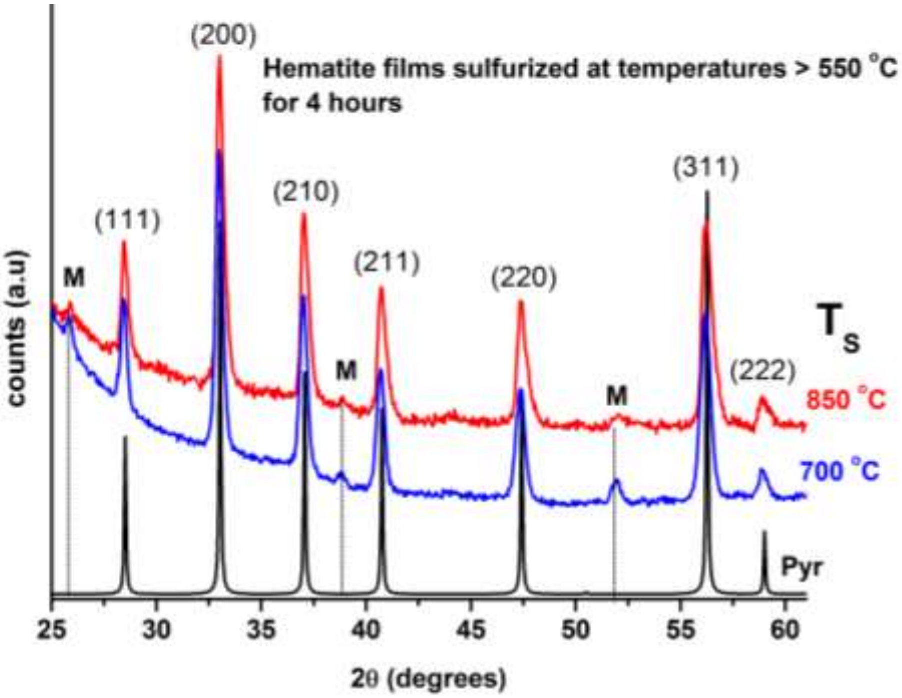

Fig. 4.5: XRD pattern of hematite films sulfurized at 700 °C and 850 °C for 4 hours. Dotted line represent marcasite peaks, whereas crosses indicate pyrrhotite peaks.

SEM images of the samples sulfurized at temperatures higher than 550 °C show a completely different microstructure than what had been observed in the previous series of samples sulfurized at lower temperatures (Fig. 4.6). The cuboid particles observed in the sample sulfurized at 550 °C for 4 hours coalesced into large clusters, hundreds of nanometers wide. In addition, the surface of some clusters of the sample prepared at 700 °C are covered with a cockscomb like structure. Such structure is, in fact, a typical crystal habit of marcasite, which, thus, corroborates the XRD results [3]. Moreover, such coverage vanished as the temperature was further increased to 850 °C, which is also in accordance with the XRD results, given by the decrease of the intensity of marcasite XRD peaks, shown in Fig. 4.5. The coalescence of the particles created gaps in between, where little or no material was left. The gaps resulted in the charging of the films during SEM imaging, which is associated with regions of poorer electric conductivity. The coalescence of the particles into isolated large clusters is more evident in the SEM images of the sample prepared at 850 °C [Fig. 4.6 **c** and **d**], where, even with low magnification, it is possible to delimit the boundaries of each cluster.

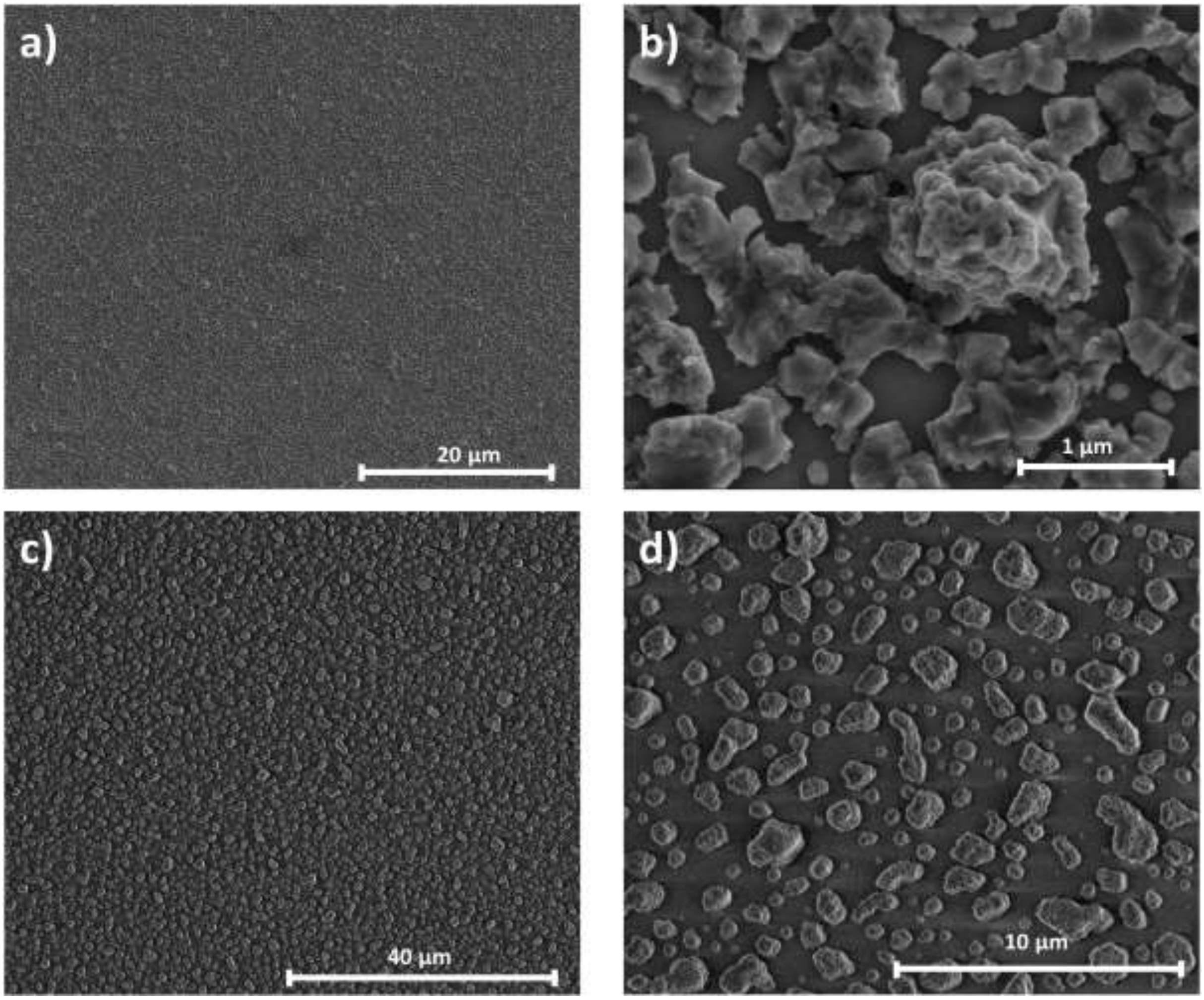

Fig. 4.6: SEM images of films sulfurized for 4 hours at **a)**, **b)** 700 ^{o}C, and **c)**, **d)** 850 ^{o}C. Large clusters were formed because of particle coalescence, generating gaps where little or no material was left. These regions were responsible for charging the films during the imaging, since the substrate (fused silica) is insulator.

The presence of marcasite as a cockscomb surface structure, shown in Fig. 4.6 **b**, is more pronounced as suggested by the intensity of the XRD peaks. The same behavior was found in the films sulfurized at lower sulfurization temperatures, where large tabular particles – associated with the marcasite phase – were observed, in contrast with minimum intensity peaks in the XRD patterns. As discussed before, the orthorhombic phase of FeS_2 may be essentially amorphous, which could simultaneously explain the XRD and SEM results. In order to test the hypothesis above, we investigated the profile of both the clusters and the superficial cockscomb coverage with TEM, and found that, in fact, the surface of the clusters is essentially amorphous (Fig. 4.7). The insets of the figure represent zoomed in images across the circled area of the particle, moving from regions closer to the bulk (right side) to the outer surface (left side). In the region nearest to the bulk, it is possible to observe atomic planes, which are not devised in regions closer to the surface.

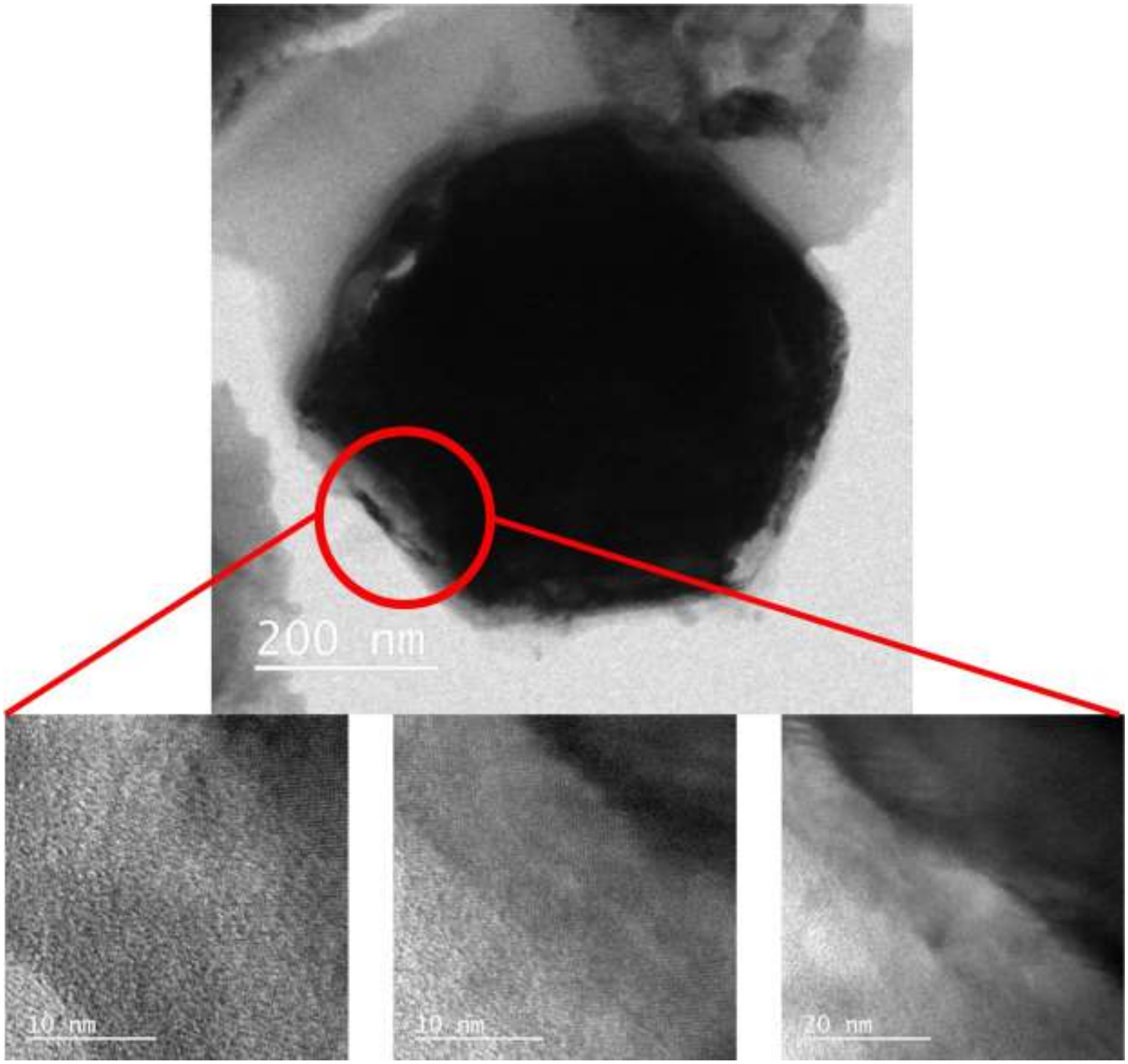

Fig. 4.7: TEM images of a FeS_2 film sulfurized at 700 °C. The insets show zoomed in images of the circled are, which clearly shows an evolution from crystalline to amorphous material, from bulk to surface areas.

We also attempted to increase the size of the film particles, by increasing the sulfurization time. Moreover, longer sulfurization times could give us an estimate of the enclosing capacity of the sulfur vapor in the Russian Doll system. Fig. 4.8 depicts the XRD patterns of the samples sulfurized at 550 °C for 4, 8, and 16 hours. The sample prepared for 4 hours was used for comparison. After 8 hours, it is clear that the sulfur fugacity inside the Russian Doll system has dropped below the equilibrium fugacity of the reaction given by eq. 2.1, given by the presence of the sulfur deficient phase, pyrrhotite (dotted lines). The lack of the polymorphic FeS_2 phase, marcasite corroborates the observation concerning the low value of the sulfur fugacity, which will be further discussed in the next section. Whereas after 8 hours the films still present pyrite in its composition, after 16 hours, the transformation reaction given by eq. 2.1 is fully completed, for pyrrhotite was the only iron sulfide phase detected.

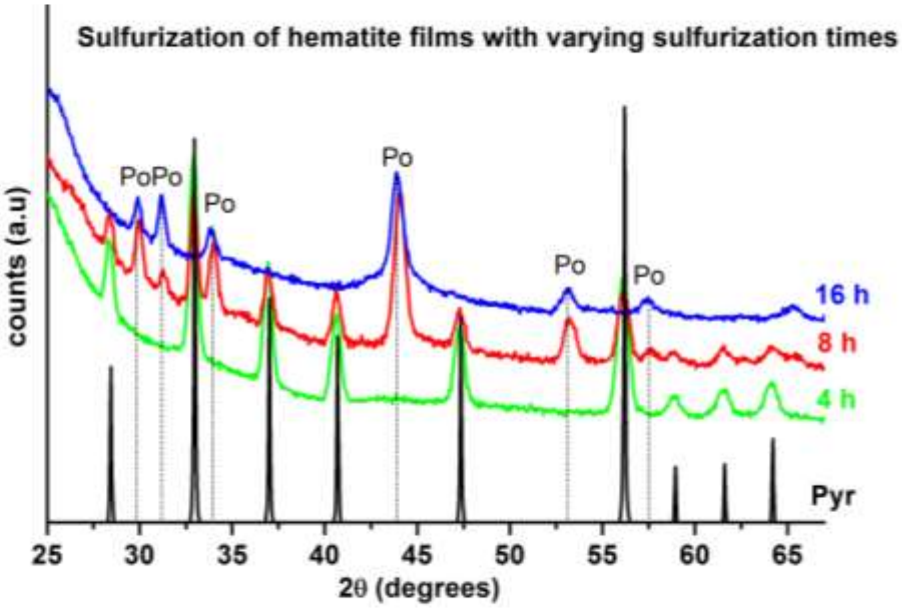

Fig. 4.8: XRD pattern of samples sulfurized at 550 °C for 4, 8, and 16 hours. Pyr represent the reference data for pyrite, whereas the dotted lines indexed by Po represent the peak positions of pyrrhotite (Fe_7S_8). Note that after 8 hours there is a mix structure of pyrite and pyrrhotite, whereas after 16 hours, the decomposition of pyrite is fully completed, and only pyrrhotite XRD peaks are observed.

SEM images (Fig. 4.9) of the samples sulfurized for times longer than 4 hours shows the process of decomposition that pyrite undergoes, as the sulfur fugacity drops inside our system. As mentioned in chapter 4, even though the series of tubes used in our system manage to enclose a sulfur rich atmosphere long enough for the completion of the sulfurization reaction – evidenced by previous results – they do not seal the sulfur vapor, as opposed to an ampoule system, which is perfectly hermetic. Consequently, there is a continuous outward flow of sulfur and N_2 (starting atmosphere inside the Russian Doll tubes), which causes the balance of the reaction 2.1 to shift towards the formation of pyrrhotite. We note that, after 8 hours, pyrite cuboid particles are still present in the film, as circled in Fig. 4.9 **b**. Pyrite decomposition begins at the surface and move towards the center [4], then, as the surface of pyrite transforms into pyrrhotite, the pyrrhotite layers also start to coalesce and to become shapeless, resulting in the structure observed in Fig. 4.9 **c** and **d**.

Conversely to the phenomenon observed in the samples sulfurized at higher T_S, marcasite was not formed – in that series of experiments, we stated that the marcasite phase was formed during the cooling stage. During cooling, the equilibrium fugacity dropps at least two orders of magnitude, shifting the reaction back towards the formation of FeS_2. However, when we increased the sulfurization time at 550 ^oC, the continuous outward flow eventually caused the sulfur partial pressure inside our Russian Doll apparatus to decrease irreversibly to low values, shifting the equilibrium towards the pyrrhotite side of the reaction. Moreover, such values of sulfur partial pressure became so low, that FeS_2 could not be formed during the cooling stage, for, even though the equilibrium fugacity of the reaction drops as the temperature decreases, it still continued higher than the sulfur vapor pressure, preventing any FeS_2 formation.

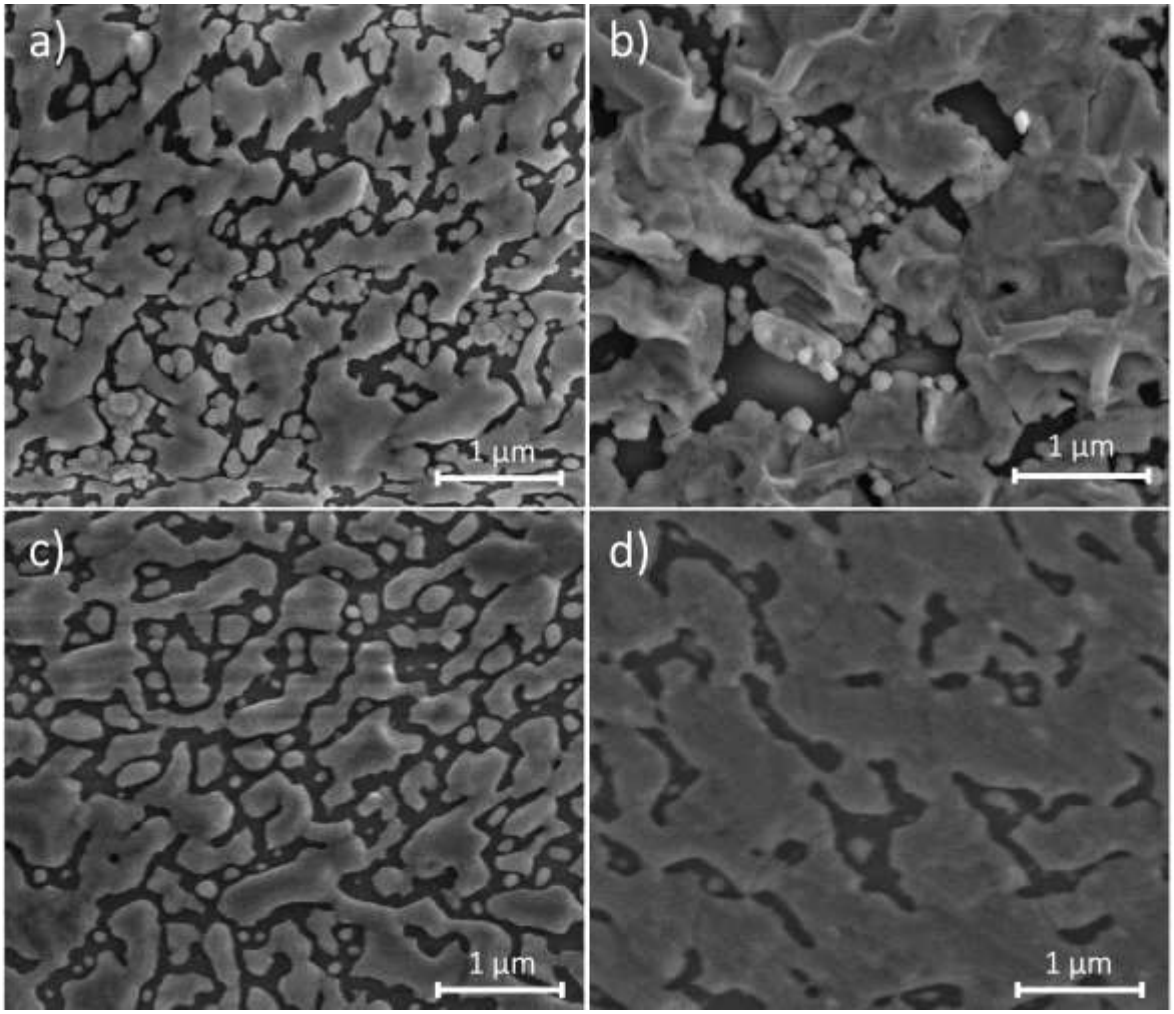

Fig. 4.9: SEM images of films sulfurized at 550 °C for **a)**, **b)** 8 hours and **c)**, **d)** 16 hours. After 8 hours, pyrite cuboid particles are still present, as highlighted in **b)**, whereas after 16 hours, only the pyrrhotite shapeless structure is left.

The partial and complete decomposition of the formed pyrite particles after 8 and 16 hours, respectively, have determined that our apparatus is capable of enclosing the sulfur rich atmosphere for not much longer than 4 hours. We then investigated the influence of the properties of the precursor Fe_2O_3 film in the resulting FeS_2, by varying the parameters of the oxidation process.

Influence of the precursor iron oxide properties on the properties of the resulting FeS_2 films

Studies have shown that the microstructure and the optical properties of spin coated hematite films change according to the oxidation temperature [5]. Thus, we analyzed the influence of the microstructure and optical properties of the precursor iron oxide films on the morphology and optical properties of the FeS_2 films, by varying the temperature of the oxidation process performed right after the spin coating. We sulfurized, at 550 ^oC, 700 ^oC and 850 ^oC, a precursor film that was not subjected to oxidation (as grown) as well as fully formed iron oxide films previously oxidized at 850 ^oC and 500 ^oC. These series of experiments are hereafter referred to as the $T_O(550)$, $T_O(700)$, and $T_O(850)$ series. In every series, the sulfurization process was performed in the same conditions – 4 hours, with 15 mg of sulfur powder and with the same heating rate of 10.5 ^oC/min. As mentioned before, due to the high temperatures used in the processes, we used a set of fused silica tubes and also prepared the films on fused silica substrates.

Fig. 4.10 **a** shows the XRD results for the $T_O(550)$ series, which unveils no presence of marcasite, as observed in previous series with prepared at 550 ^oC for 4 hours. We analyzed the degree of preferential growth of the more intense peaks, f_{hkl}, determined as: [6]

$$f_{hkl} = \frac{P(hkl) - P_0(hkl)}{1 - P_0(hkl)}, \qquad [4.1]$$

where $P(hkl)$ and $P_o(hkl)$ represent the intensity of a given XRD peak divided by the sum of intensities of all the peaks of the measured sample and the reference powder XRD (therefore with no preferential growth), respectively.

$$P(hkl) = \frac{I(hkl)}{\sum I(hkl)}, \qquad [4.2]$$

$$P_0(hkl) = \frac{I_0(hkl)}{\sum I_0(hkl)}, \qquad [4.3]$$

However, as shown in Fig. 4.10 **b**, the value of f_{hkl} is close to zero (maximum around 0.02) indicating that the samples do not possess any preferential growth orientation. Thus, we found no significant change in the samples when analyzing XRD patterns only.

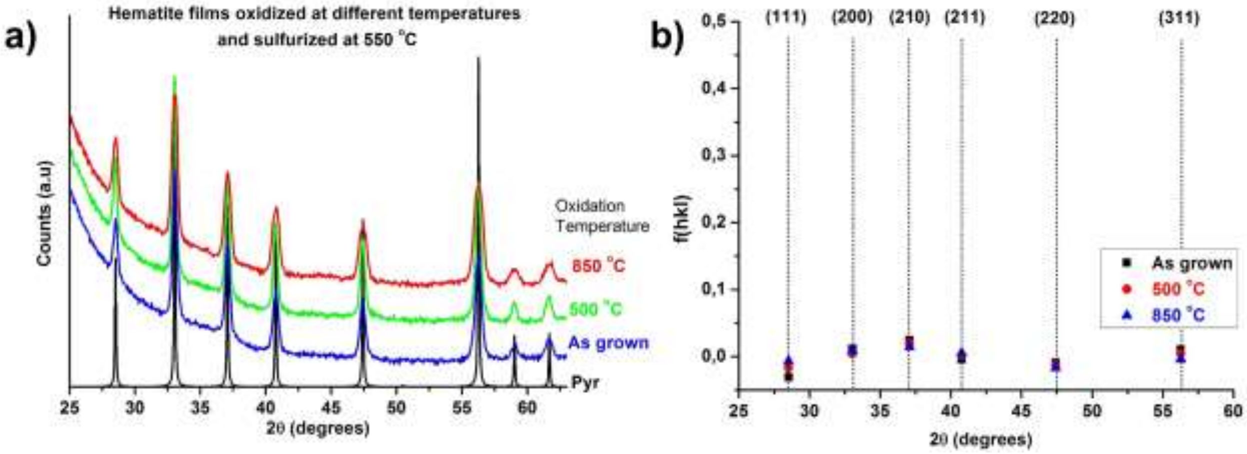

Fig. 4.10: **a)** XRD of the $T_O(550)$ series. We observed no clear difference from the samples; **b)** degree of preferential growth. Note that the values of f_{hkl} are all close to zero.

SEM images (Fig. 4.11) also show no evidence of the presence of marcasite, given by the lack of tabular particles and cockscomb structures. Nevertheless, we do observe evidence of particle growth as the oxidation temperature, T_O, increased. This result is more evident in the right side of Fig. 4.11, which shows the size distribution of the particles for each sample. We measured the size of the particles with the software ImageJ and found that the distribution broadens for increasing T_O, resulting in larger mean particle sizes for samples annealed at higher temperatures. The mean values (x_C) were obtained using a LogNormal function distribution fit.

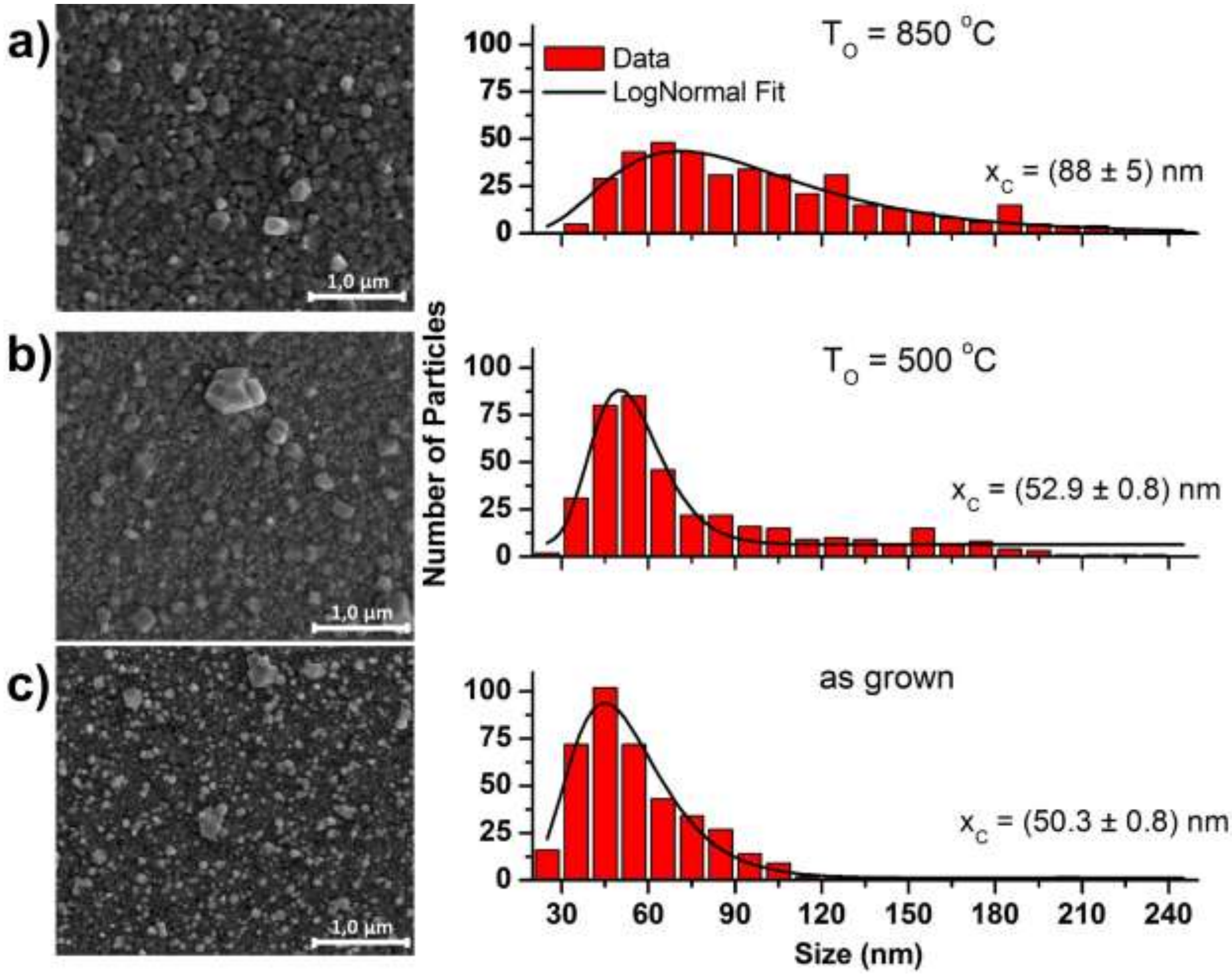

Fig. 4.11: SEM images of pyrite films produced by sulfurization of iron oxide films oxidized at **a)** 850 °C, **b)** 500 °C, and **c)** as grown. As shown in the images, and corroborated by the histogram on the right side, precursor oxide films oxidized at higher temperatures resulted in sulfide films with larger particles.

As we increased the sulfurization temperature up to 700 °C, we observed, once again, the presence of marcasite peaks in the XRD pattern (Fig. 4.12 **a**). The intensity of the marcasite peaks increased a little as the oxidation temperature increased, as evidenced by the most intense peak at $2\theta \sim 52$ °. We also calculated f_{hkl} for the T_O(700) series following similar procedure described above. The results depicted in Fig. 4.12 **b** show that all the samples have similar behavior, showing no preferential growth orientation.

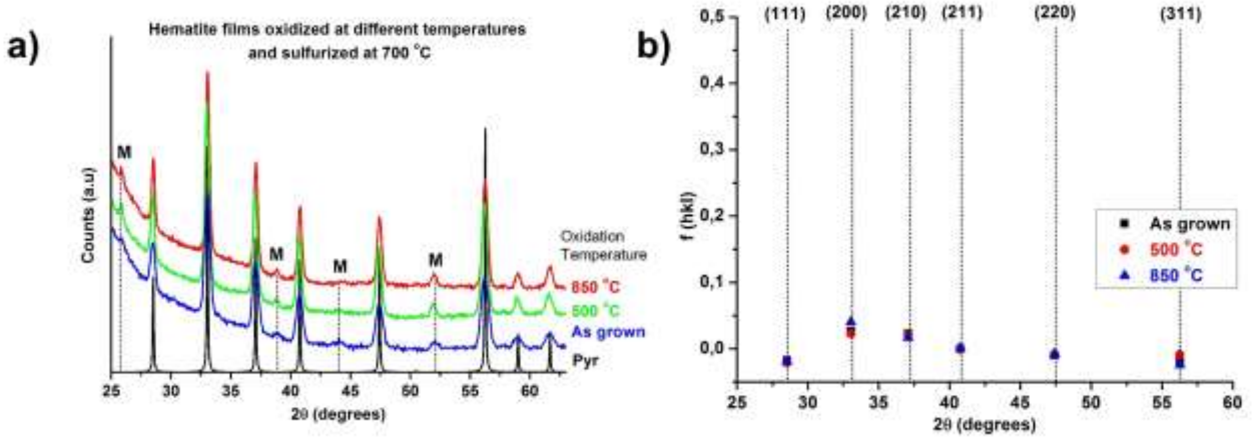

Fig. 4.12: **a)** XRD patterns of the T_O(700) series. Marcasite peaks are indexed by "M". **b)** Values of f_{hkl} evidencing the samples have no preferential growth orientation.

Analyzing the SEM images of the samples sulfurized at 700 °C (Fig. 4.13), we observed that, once again, the films have coalesced in large clusters, a few hundreds of nanometers wide, and the surface of each particle is covered with features having a cockscomb morphology, as displayed by the circled area. As mentioned early in the chapter, such morphology is a common crystal habit associated with the marcasite phase, which corroborates the XRD results [3]. In addition, we have already shown that the cockscomb coverage is essentially amorphous, which explains the low intensity of the marcasite XRD peaks. Concluding, sulfurizing iron oxides with different properties had little effect on the resulting FeS_2 when the sulfurization process occurred at 700 °C.

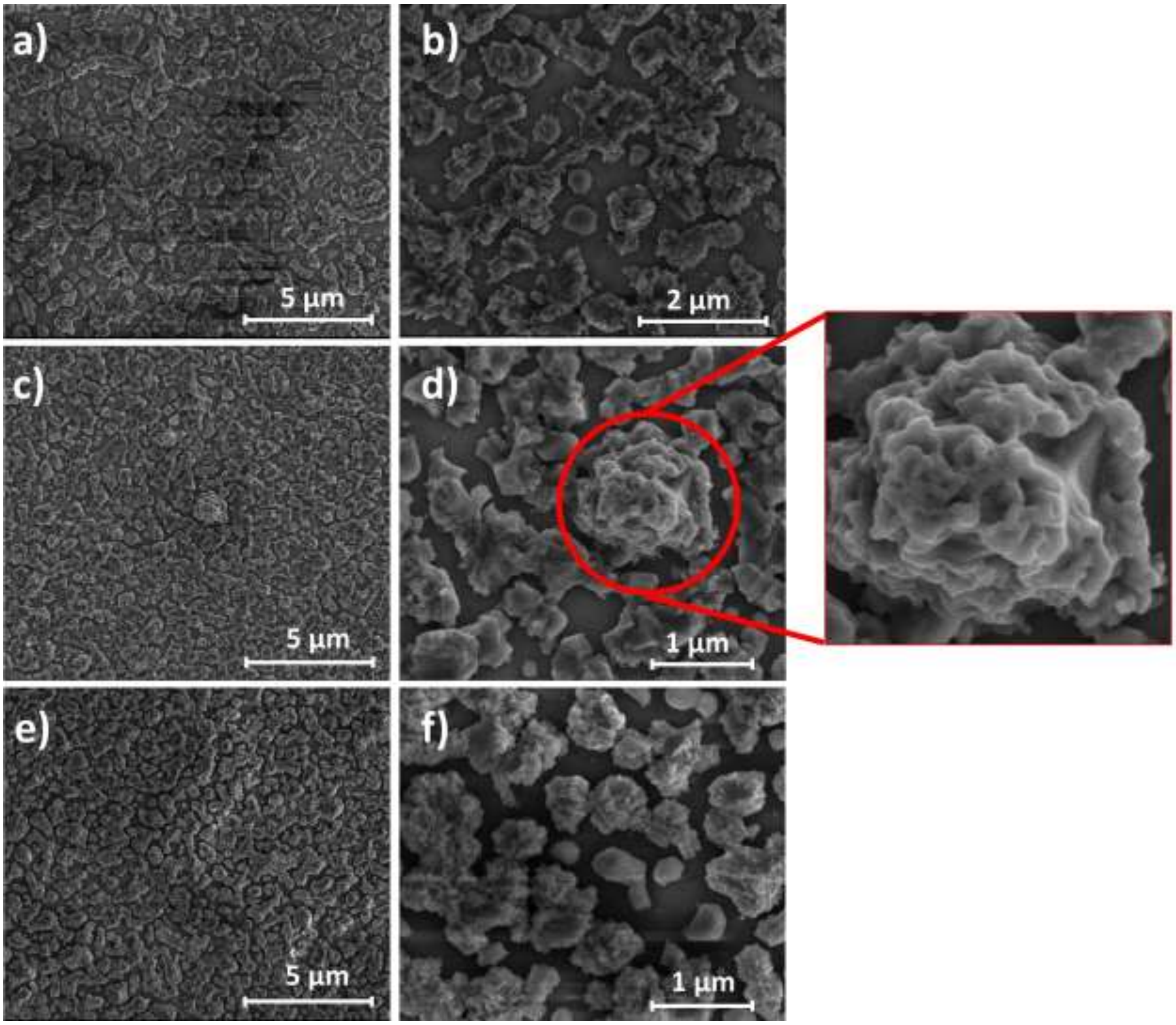

Fig. 4.13: SEM images of pyrite films produced by sulfurization at 700 ^{o}C of **a)**, **b)** as grown iron oxide films, and iron oxide films annealed at **c)**, **d)** 500 ^{o}C, and **e)**, **f)** 850 ^{o}C, respectively. Two crystal habits are again observed: cuboid particles a few hundreds of nanometers wide and a cockscomb coverage on the surface of the cuboid particles, as evidenced by the inset.

Finally, Fig. 4.14 shows the XRD patterns of an as grown iron oxide film and a fully formed iron oxide film oxidized at 500 ^{o}C, both sulfurized at 850 ^{o}C for 4 hours. The oxidized iron oxide result has been presented earlier in the chapter, and, as mentioned, is composed essentially of pyrite with traces of marcasite (dotted lines) and pyrrhotite (crosses). On the other hand, the amorphous as grown film, resulted in a mix phase of pyrite, pyrrhotite and marcasite, with a significant increase in the intensity of the pyrrhotite peaks.

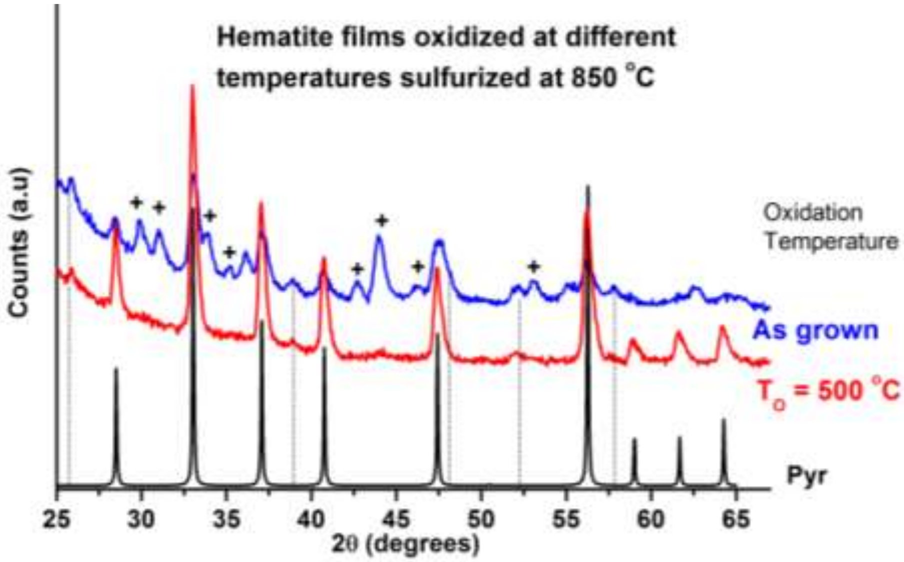

Fig. 4.14: XRD patterns of hematite films annealed at different temperatures and sulfurized at 850 °C. The film oxidized at 500 °C is composed essentially of pyrite (indicated by crosses), with traces of marcasite (dotted lines) and pyrrhotite, whereas the as grown film resulted in a mix phase film of pyrite, marcasite and pyrrhotite.

Therefore, pyrite films produced from amorphous iron oxide films have decomposed more than the ones produced from fully formed iron oxide films, which suggests that the crystallinity of the pyrite films is also directly related to the crystallinity of the precursor iron oxide. Moreover, fully formed hematite films oxidized at 500 °C, resulted in larger isolated clusters when compared to amorphous oxide, after sulfurization at 850 °C, as evidenced in Fig. 4.15. The dependence of the size of the clusters with the oxidation temperature corroborates the results depicted in Fig. 4.11, which shows that FeS_2 particle grow for higher oxidation temperatures.

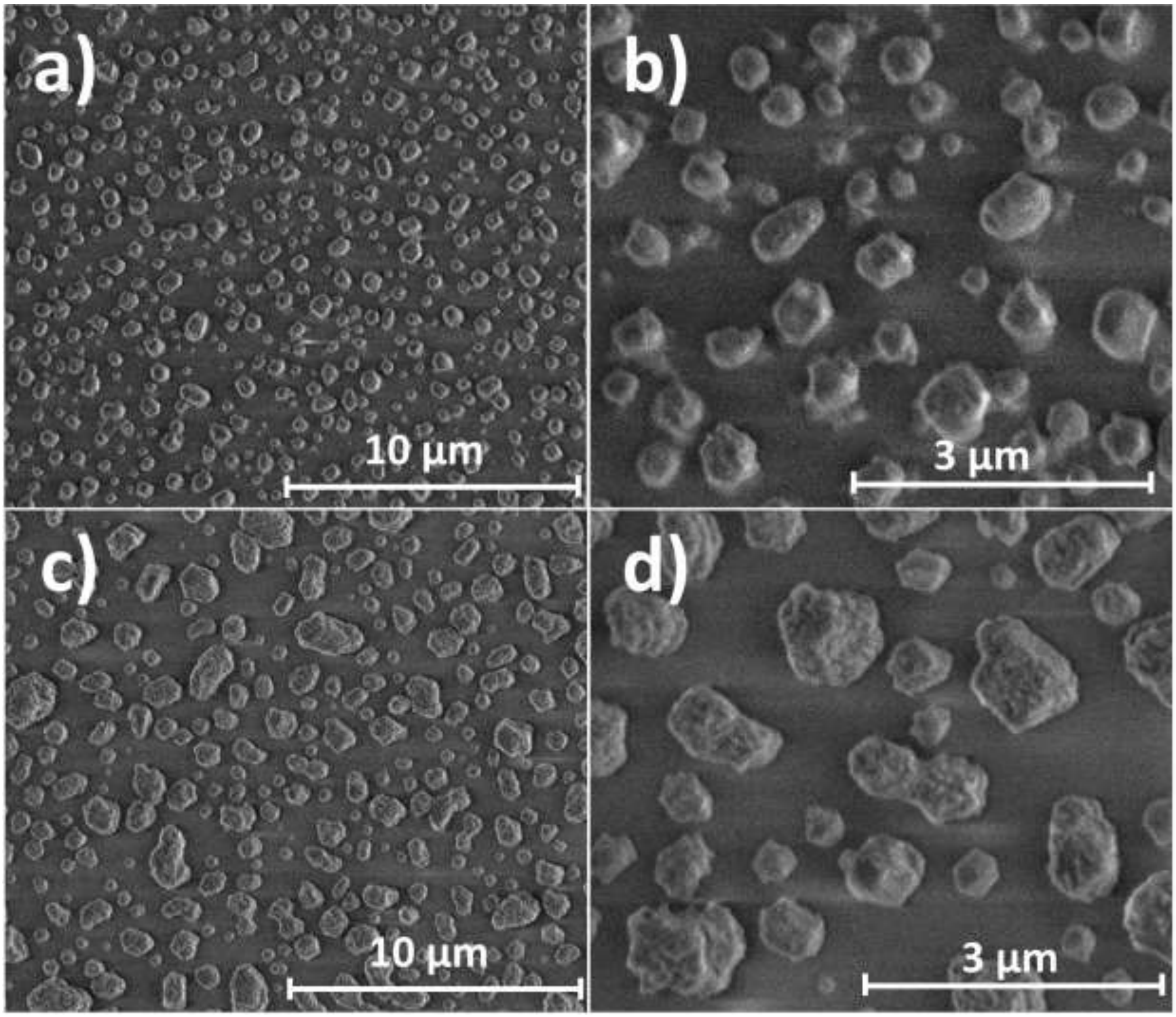

Fig. 4.15: SEM images of pyrite films produced by sulfurization at 850 ^oC of **a)**, **b)** as grown iron oxide films, and **c)**, **d)** iron oxide films oxidized at 500 ^oC, respectively. We note that in both cases, the coalescence of the particles due to the temperature formed isolated clusters, and the size of the clusters increased for increasing oxidation temperature.

We also increased the duration of the oxidation process, and prepared samples oxidized at 500 ^oC for 30 minutes and 6 h, later sulfurized at the standard optimum conditions – 550 ^oC for 4 hours. However, we observed no significant variations in the composition and microstructure of the resulting FeS_2 films.

4.2 – DISCUSSION

The results obtained in the first two series of experiments (low T_S and t_S series) indicate the presence of both FeS_2 polymorphs with a dominance of pyrite. The formation of the two polymorphs is commonly observed under laboratory conditions as well as in nature, as their thermodynamic properties differ only slightly [7]. The dominance of pyrite is also expected at the temperature range analyzed, considering marcasite usually forms in colder environments [7]. Moreover, many authors have reported that for temperatures higher than 400 °C, marcasite undergoes an irreversible transformation reaction into pyrite [7, 8, 9]. Lennie and Vaughan analyzed the kinetics of the marcasite-pyrite transformation and found that the time completion of the reaction decreases for increasing temperature [9]. Fleet observed a similar behavior, reporting partial and essentially complete transformations after 12 h at 425 °C, and after less than 4 hours at 475 °C, respectively [7]. The temperature dependence of the marcasite-pyrite transformation corroborates our observations regarding the decrease in the concentration of marcasite (tabular particles) for increasing sulfurization temperature and time. As shown in the SEM images, the tabular particles essentially disappear after 120 minutes at 550 °C, and completely vanish after 240 minutes, which is in accordance with the values reported by Lennie and Vaughan [9].

Fleet studied the structural aspects of such polymorph transformation using XRD and discovered that there is little structural reorganization involved [10]. According to the author, the structure of pyrite is readily obtained by rotation of half the disulfide groups in marcasite. In addition, Lennie and Vaughan analyzed the kinetics of the transformation by means of the Johnson-Mehl equation, which follows:

$$\alpha = 1 - e^{[(-k.t)^m]}\ , \qquad [4.4]$$

where α represents the relative portion of pyrite in the sample, *i.e*:

$$\alpha = \frac{P}{P+M}\ , \qquad [4.5]$$

where *P* and *M* represents the weight percent of pyrite and marcasite respectively in the sample. The authors also discovered when they analyzed the evolution of α in time for samples heated at different temperatures, that the shape of the curves given by eq. 4.4 were the same for every sample. Reactions that have the same reaction curve for a range of experimental temperatures are termed isokinetic and have the same value of *m* in the Johnson-Mehl equation. Additionally, the values obtained in the experiments of Lennie and Vaughan, when compared to the tabulated values by Hancock for several solid-state reactions, are related to nucleation and growth at grain edges mechanisms [8,10]. Thereupon, the authors stated that there must be negligible diffusion in the transformation process of marcasite into pyrite, which is supported by the simplicity of the structural changes occurred during the reaction.

The lack of diffusion during the reaction indicates that the pattern observed in the SEM images of Fig. 4.4 (continuous deconstruction of large particles) may instead be explained by a fragmentation of the tabular particles due to nucleation of pyrite crystals on the edge of marcasite structures. The plates, thus, cracked down to cuboid particles, which is corroborated by Fig. 4.4 **c**, where it is visible a small reminiscent plate, smaller than the ones originally found earlier in the process (Figs. 4.4 **a**,**b**). The cracking mechanism is more evident in Fig. 4.16 below, where a SEM image of a film prepared for 2 h at 550 ^{o}C shows gaps (circled areas) shaped similarly to the marcasite tabular particles presenting cuboid particles within the gap area as well as on the edges.

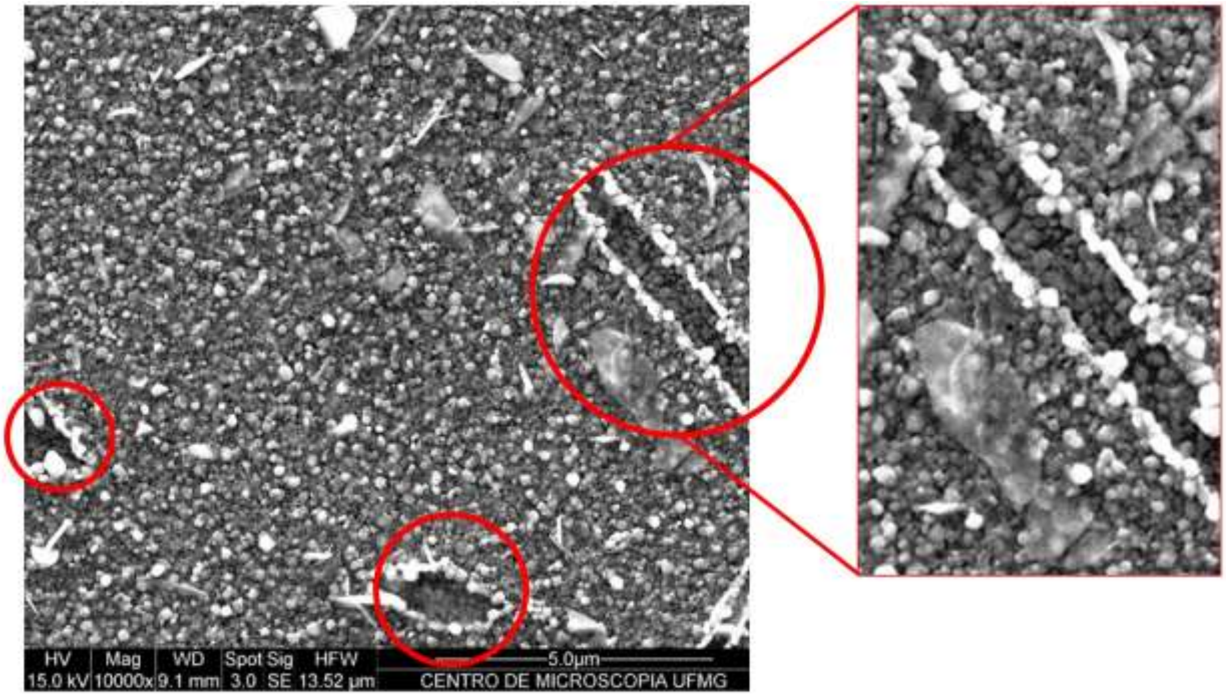

Fig. 4.16: SEM image of a FeS_2 sulfurized at 550 °C for 2 hours. The circled areas display gap regions shaped similarly to the tabular particles associated with the marcasite phase, with cuboid particles filling the voids. This pattern corroborates our statement that the tabular particles cracked down into cuboid particles during the sulfurization process.

As we increased the sulfurization time up to 8 and 16 hours, we observed the decomposition of the cuboid pyrite particles, resulting in shapeless pyrrhotite formation. According to Toulmin and later confirmed by J.P Hansem *et al*, the equilibrium sulfur fugacity of the decomposition reaction (eq. 2.1) increases as the temperature increases (shown in Fig. 2.5) [11]. Therefore, the increasingly presence of pyrrhotite for longer times, up to a phase pure pyrrhotite film after 16 hours, stems from a low value of sulfur vapor pressure inside our Russian Doll apparatus, caused by the continuous outward flow of sulfur + nitrogen (starting atmosphere inside the system). The SEM images of Fig. 4.9 reveals that as the pyrite particles decompose, the superficial pyrrhotite layer coalesces, resulting in a shapeless mass. In Fig. 4. 9 **b**, we see that there were still a few cuboid particles left, which had not decomposed yet. As the sulfurization time increased, the amount of sulfur vapor inside the apparatus was further reduced and, consequently, the remaining pyrite particles completely decomposed into pyrrhotite, as evidenced by the XRD pattern displayed in Fig. 4.8. Therefore, the Russian Doll apparatus is effective and enable us to produce high quality pure phase pyrite films for sulfurization times not much longer than 4 hours. After that, the remaining sulfur vapor inside the system decreases to values too close to the equilibrium value of the reaction 2.1, and will eventually result in the decomposition of the recent formed pyrite film into pyrrhotite.

We further increased the sulfurization temperature in an attempt to promote particle growth. However, as the temperature increased, along with the growth effect – evidenced by the appearance of large clusters, a few hundreds of nanometers, and even micrometers, wide – the films also started to decompose, given by the detection of traces of marcasite and pyrrhotite. The increase in temperature is followed, according to the literature, by an increase in the equilibrium sulfur fugacity of reaction 2.1, as illustrated in Fig. 2.5. Thus, as the equilibrium fugacity increased, the sulfur loss experienced in our Russian Doll apparatus achieved the equilibrium value faster than for lower temperatures. Consequently, the decomposition reaction began sooner, decreasing the 4 hours enclosing time limit established in the previous samples. In addition, along with the increase in the sulfur equilibrium fugacity, the formation of larger allotropic sulfur species at high temperatures, boosts the decomposition process of pyrite particles. As stated in eq. 2.1, the products of the decomposition reaction are pyrrhotite and S_2 gas, hence, the equilibrium sulfur fugacity illustrated in Fig. 2.5 concerns only the S_2 species. However, sulfur may exist in several distinct S_n allotropes, whose formation results in a further decrease of the S_2 partial pressure in the system, favoring the decomposition reaction. Fig. 4.17 shows a curve of the molar fraction in sulfur gas of the different allotropic species with $n \leq 8$, which was constructed by J.P. Hansen *et al* from a combination of the equilibrium constants compiled by Gurvich *et al* and the model proposed by Hong *et al* [4,12,13]. The figure shows that for temperatures lower than 800 K (~527 ^{o}C) S_2 is the dominant species, corresponding to approximately 99% of the sulfur gas. At higher temperatures, though, the molar fraction of larger allotropic species (mainly S_3, S_5, and S_6) increase to significant levels, which sums up to 6% at 900 K (627 ^{o}C) and close to 35% at 1000 K (727 ^{o}C). Concluding, the drop of the actual S_2 partial pressure during the decomposition reaction due to the formation of other sulfur allotropic species, along with the increase in the equilibrium sulfur fugacity of the reaction, favors the decomposition of pyrite. Nevertheless, since the composition of the films sulfurized at both 700 °C and 850 °C were still predominantly pyrite with just traces of the secondary iron sulfide phases, the decomposition reaction did not occur for too long, with the sulfurization process ending not long after the decomposition began, preventing its completion. Finally, as the system began to cool down – which resulted in a drastic drop of two orders of magnitude in the equilibrium sulfur fugacity – the superficial pyrrhotite layer, still in formation, transformed back into FeS_2. On the one hand, that explains the lack of pyrrhotite, but on the other hand, it does not clear out the presence of marcasite.

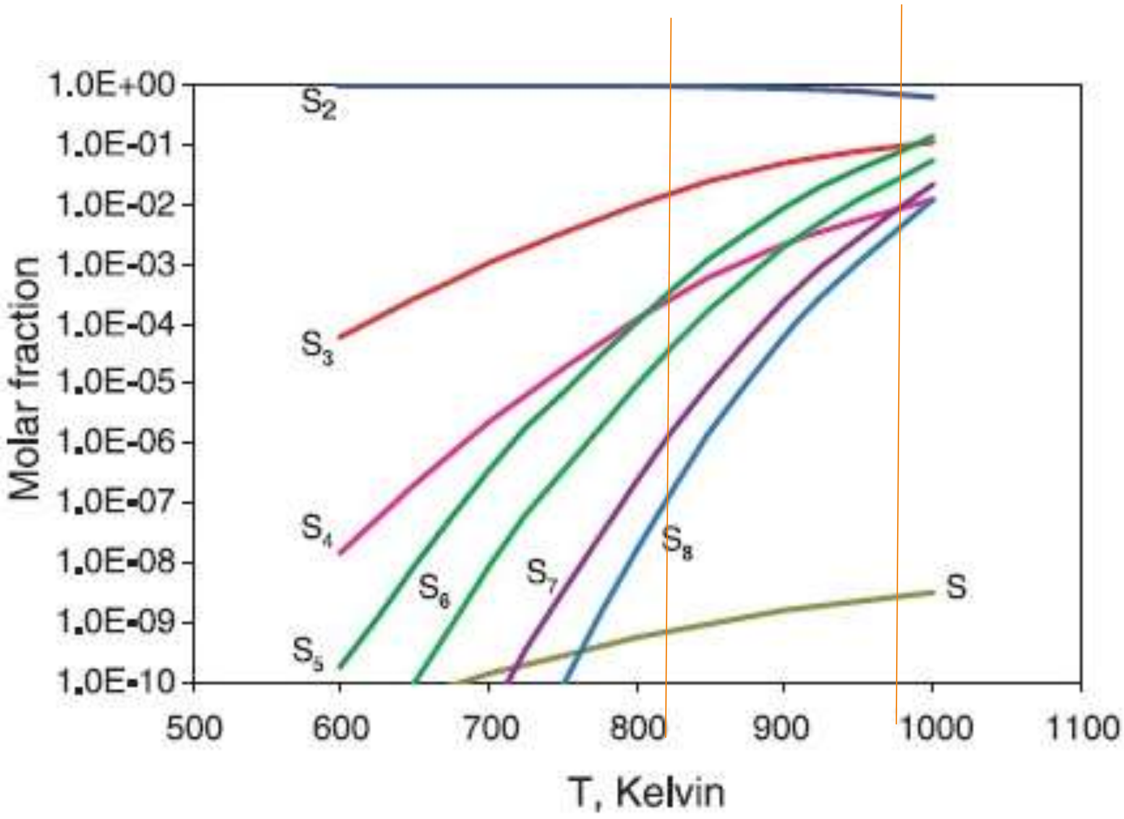

Fig. 4.17: Molar fraction of different allotropic species of sulfur gas over pyrite. The diagram was extracted from ref 4.

We have stated earlier in the chapter that marcasite is commonly observed together with pyrite both in nature and under laboratory conditions. However, marcasite undergoes an irreversible transformation reaction to pyrite and we have already determined that 4 hours was long enough for the completion of the reaction, when the films were prepared at 550 °C.

Additionally, the time for the completion of the transformation reaction decreases for increasing temperature, thus, at temperatures higher than 550 ^oC the marcasite formed along with pyrite in the beginning of the sulfurization process must have been fully transformed to pyrite after even less than 4 hours. Consequently, the marcasite that we observed with XRD (Fig. 4.5) in the films prepared at temperatures higher than 550 ^oC must have been formed some other way in some other time. Finally, the different crystal habits in which marcasite was formed in the films, firstly, as tabular particles spread along with the cuboid particles, and secondly, as a cockscomb structure on the surface of the coalesced cuboid particles, supports our statement.

Studies have shown that marcasite and pyrite are not exactly polymorphs, that they have in fact different chemical compositions, with pyrite being stoichiometric and marcasite being slightly sulfur deficient [14]. As mentioned, the cockscomb marcasite is situated on the surface of the pyrite clusters, where sulfur composition is usually deficient in comparison with the core. In fact, such difference in sulfur composition between the surface and the bulk in pyrite crystals has been attributed as the main source for the formation of the hole-rich inversion layer, which, itself, has been correlated as the reason for the low V_{OC} measured in pyrite based solar cells, as discussed in chapter 2 [15]. Thereby, the presence of marcasite as a cockscomb structure on the surface of the pyrite clusters supports the assumption that marcasite is slightly sulfur deficient in comparison with pyrite. Further, the location and sulfur deficiency of the marcasite are likely to be related with the process of formation of the material.

The high temperature of sulfurization process involved in the production of the given films increased the equilibrium sulfur fugacity of the decomposition reaction (eq. 2.1) up to values close to 1 atm. Such value is close to the starting sulfur partial pressure produced by the sublimation of the sulfur powder inside our Russian Doll apparatus. Consequently, due to the outward flow of the gas ($N_2 + S_2$) inside the apparatus, such value of the sulfur partial pressure must have decreased down to values lower than the equilibrium sulfur fugacity during the process, setting of the decomposition reaction of the coalesced large clusters observed in the SEM images of Fig. 4.6. The fact that pyrrhotite peaks were not detected in the XRD experiments, however, stems from the inverse reaction that occurred during cooling down of the system, transforming the recent formed pyrrhotite back to FeS_2.

According to J.P Hansen *et al*, the decomposition reaction of pyrite follows the unreacted core model, in which the process occurs primarily at the surface of the material and moves toward the unreacted core. Fig. 4.18 shows a SEM image of a partially decomposed pyrite particle, clearly revealing the formed pyrrhotite layer and the unreacted pyrite core.

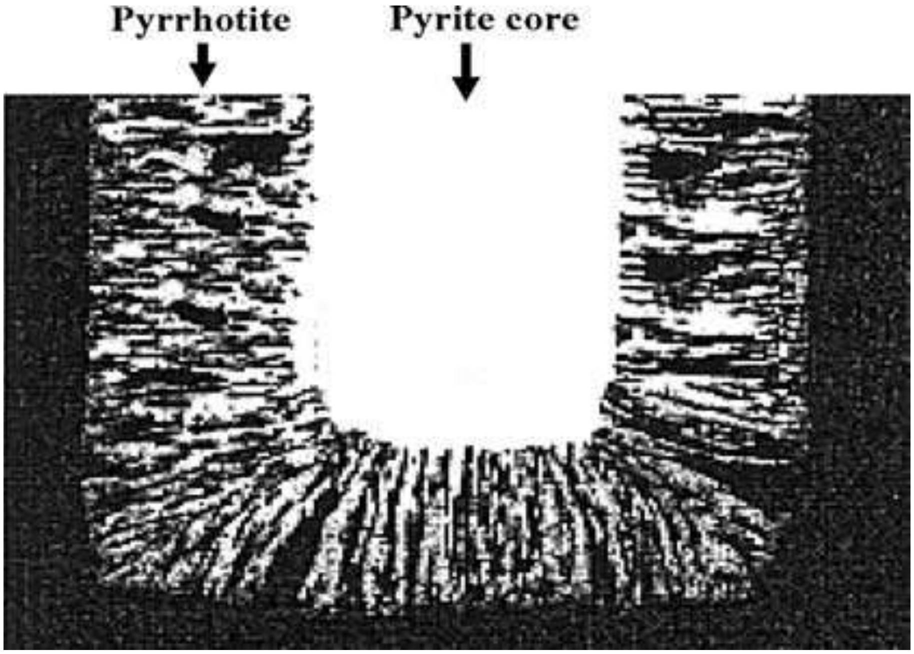

Fig. 4.18: SEM image of a partially decomposed pyrite particle with dimensions of length, width and thickness of 1-2 cm, 1 cm, and 0,05 cm, respectively (extracted from ref 4.

The pyrite-pyrrhotite decomposition occurs, then, when the surface starts to release sulfur to the environment, forming a primary pyrrhotite layer, close to the surface. As the process continues and the interface between the primary pyrrhotite layer and the pyrite core moves further inward the particle, the surface continuously releases sulfur. Eventually, the diffusion of sulfur across the primary pyrrhotite layer is not enough to compensate for the sulfur loss to the surroundings, thus creating a gradient composition of the element across the primary pyrrhotite layer, which, ultimately, forms a secondary, S deficient, pyrrhotite layer, between the primary one and the surface. This polymorphism across the decomposed pyrrhotite layer was verified by Fegley and Lodders, and Lambert *et al*., who were able to identify two different pyrrhotite phases in partially decomposed pyrite particles [16,17]. If the process continues for long enough, the pyrite core will decompose at last, and the result will be a multi-phased pyrrhotite particle. The multi-phase aspect of the particle arises from the variety of pyrrhotite phases associated with different sulfur contents, and the gradient of S content formed across the particle during decomposition. As shown in Fig. 2.5, the decomposition may continue until elemental iron is formed. Fig. 4.19 illustrates the formation of the two pyrrhotite layers and the unreacted pyrite core, during decomposition of a pyrite particle.

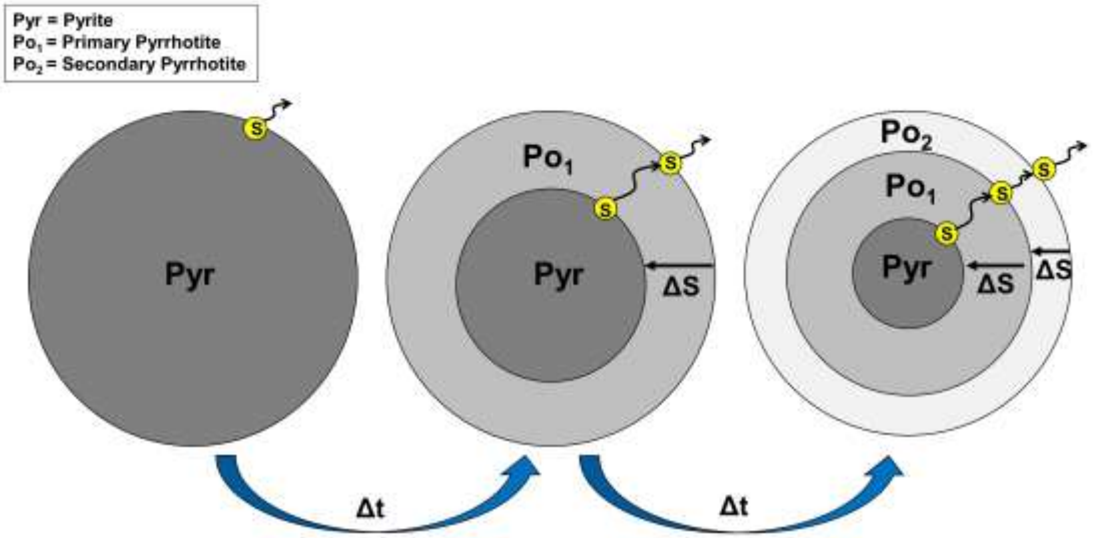

Fig. 4.19: Scheme illustrating the decomposition process of pyrite. First, the surface starts to release sulfur, creating a primary pyrrhotite layer (Po_1), which advances inwards the unreacted pyrite core (Pyr). The continuous release of sulfur at the surface eventually creates a composition gradient of S across the primary pyrrhotite layer, which ultimately forms a secondary, sulfur deficient, pyrrhotite layer (Po_2).

The presence of a sulfur content gradient across the pyrrhotite layer may explain the presence of the cockscomb marcasite on the surface of the pyrite clusters. Even though no pyrrhotite peaks were observed in XRD experiments, during the sulfurization process at temperatures higher than 550 °C, the formation of a pyrrhotite layer for longer sulfurization times is expected as a result of a drop of the sulfur partial pressure below the equilibrium value of the reaction given by eq. 2.1. Such layer must have undergone an inverse reaction during the cooling down of the system, producing FeS_2. Because of the difference in sulfur content across the pyrrhotite layer, the final FeS_2 produced from the inverse reaction must contain a composition gradient, with the surface being slightly S deficient. Considering the reports of Buerger and Gronvøld and Westrum Jr, the formation of FeS_2 during the cooling down of the system, as a result of the inverse reaction given by eq. 2.1, explains the presence of the marcasite phase at the surface, for, this phase, contrarily to the cubic pyrite, is not stoichiometric, but rather, S deficient.

We concluded the study of the sulfurization process alone, defining the best parameters for the production of phase pure pyrite films, which are: sulfurization temperature 550 ^{o}C, and sulfurization time 4 hours. The films produced following such recipe presented **n**-type conductivity, which is abnormal for FeS_2 thin films, according to Table I, but consistent with the results obtained by C. Leighton *et al* [18]. Any variation on the parameters listed above resulted in partial or complete decomposition of the pyrite particles, and/or the presence of the orthorhombic phase of FeS_2, marcasite. On one hand, longer times resulted in a decrease in the sulfur partial pressure inside the Russian Doll apparatus, causing the pyrite film to decompose into pyrrhotite. On the other hand, higher temperatures, which we used to increase the size of the particles, eventually caused the pyrite films to decompose as well, due to a higher equilibrium sulfur fugacity. Moreover, the large clusters formed during coalescence of the cuboid particles did not form a continuous film, but rather isolated clusters, evidenced by the charging of the films during SEM imaging, from the exposure of the insulate fused silica substrates. Therefore, even if we could prevent decomposition of the film, increase the sulfurization temperature would result in a highly resistive film, because of the formation of cracks from the isolation of the coalesced particles. We then pursued an alternative route to promote particle growth, by varying the oxidation process. The several processes discussed are illustrated in Fig. 4.20.

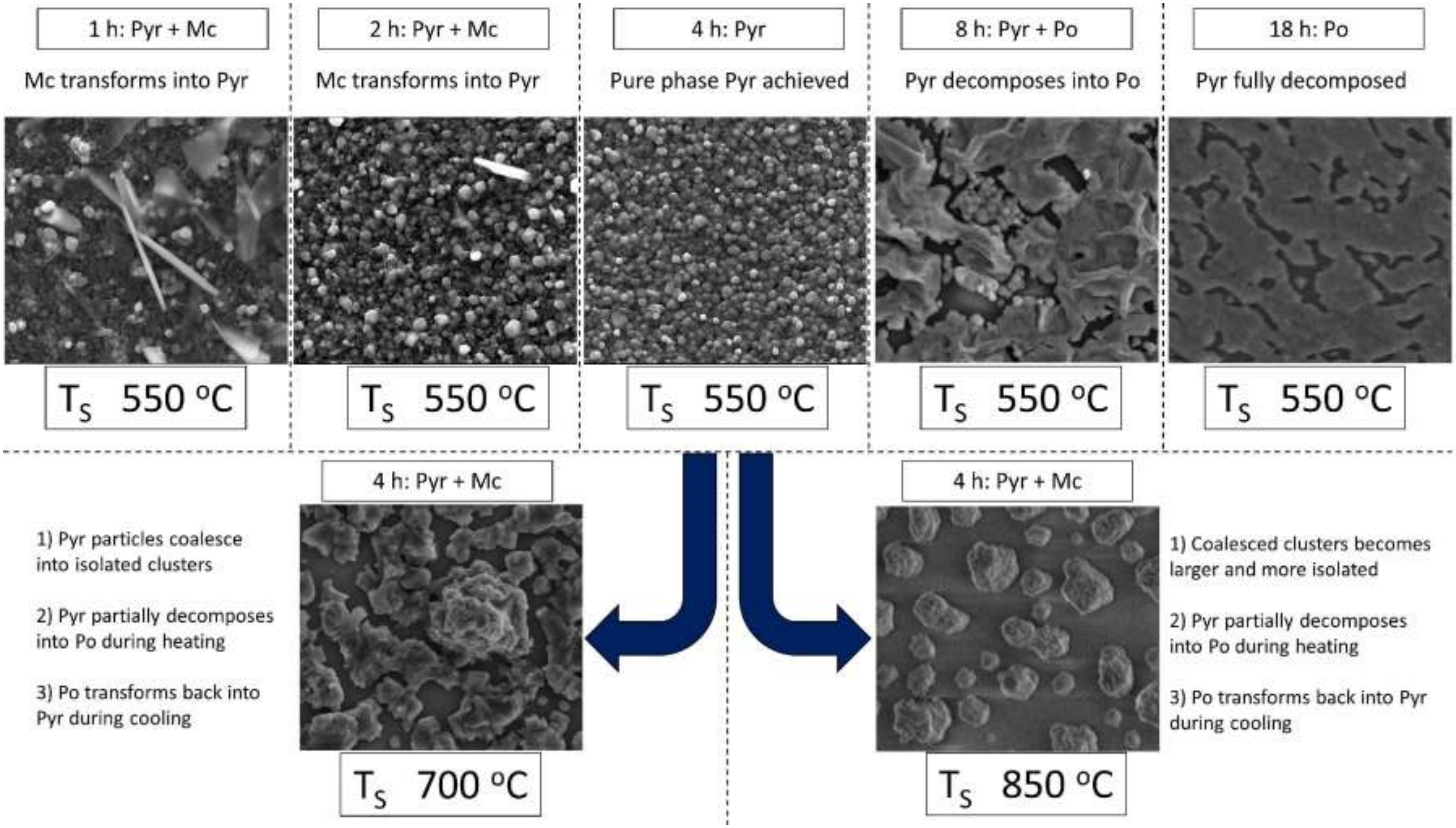

Fig. 4.20: Evolution of the composition of the material in the various sulfurization conditions.

L.P Souza *et al* showed the influence of the oxidation temperatures on both the properties and the microstructure of spin-coated hematite films [5]. According to the authors, increasing oxidation temperatures result in augments in the optical absorption of hematite, as well as in increases in the grain size. We also observed the last phenomenon through Atomic Force Microscopy (AFM) experiments performed on hematite films oxidized at 450 ^oC, 600 ^oC, 750 ^oC, and 1000 ^oC, as shown in Fig. 4.21 below. All hematite films analyzed by AFM were prepared on fused silica substrates. Thus, we decided to analyze the effect of varying the properties of the precursor iron oxide films on the properties of the resulting FeS_2 films, by sulfurizing in the same conditions, hematite films oxidized at different temperatures.

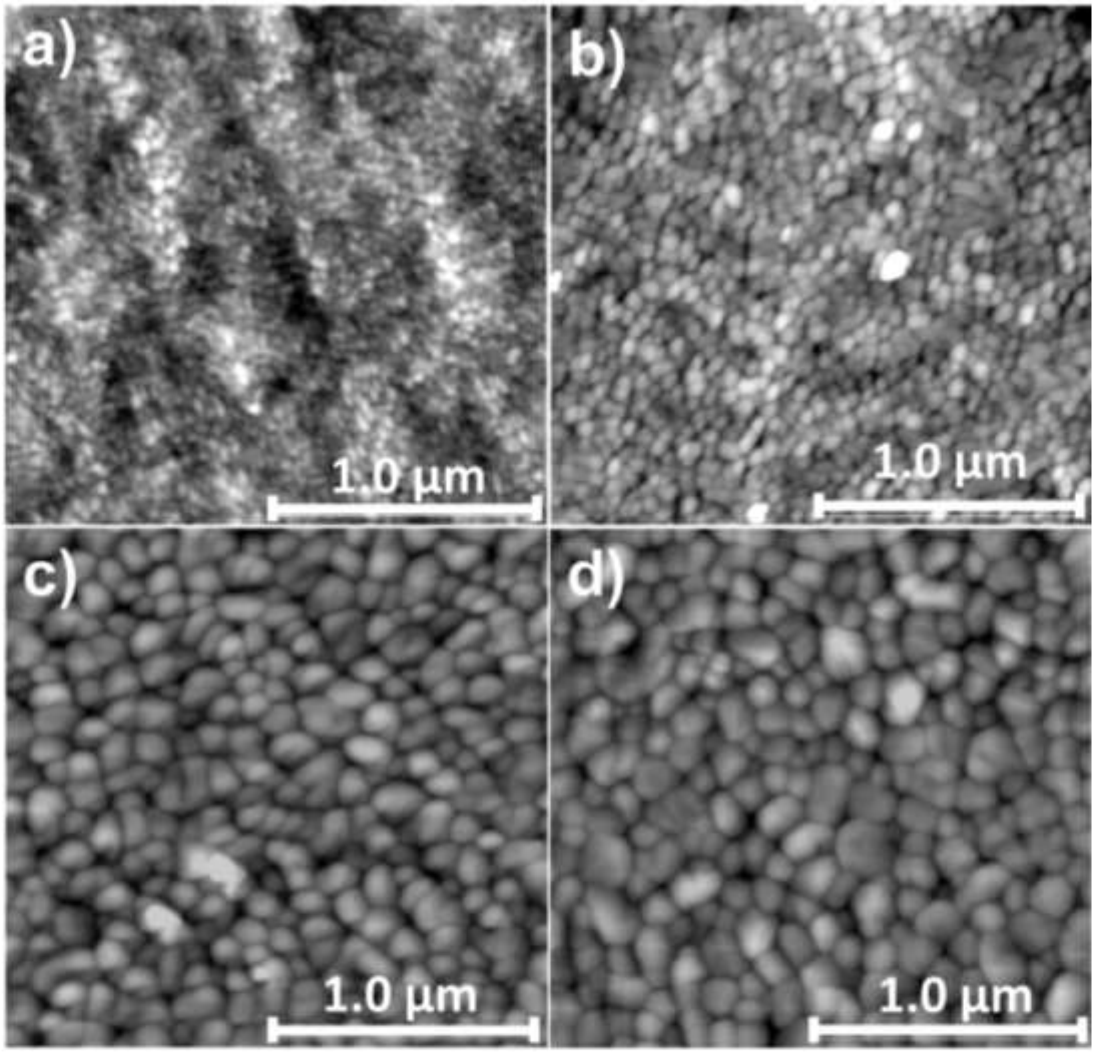

Fig. 4.21: Spin-coated hematite films annealed at **a)** 450 ^oC, **b)** 600 ^oC, **c)** 750 ^oC, and **d)** 1000 ^oC. As the oxidation temperature increased, we also observed an increase in the size of the particles.

When we sulfurized at 550 °C hematite films oxidized at different temperatures, we observed that the FeS_2 particles enlarged as the oxidation temperature increased (Fig. 4.11), similarly to the behavior of the iron oxide illustrated in Fig. 4.21. Thus, hematite films with larger particles resulted in pyrite films with larger particles as well. Contrary to increasing both sulfurization time and temperature, the augment in the oxidation temperature did not result in decomposition of the films, neither did the particles grew into isolated clusters, but rather, the enlarged particles maintained a continuous aspect. Thereby, sulfurizing hematite films with larger particles proved to be a good strategy to promote FeS_2 particle growth in our Russian Doll apparatus, and, consequently, to produce pyrite films with better quality. Additionally, we demonstrated that the oxidation stage is not necessary to produce pyrite films, although, sulfurizing amorphous materials will result in films with smaller particles with lower quality.

Pyrite films sulfurized at 700 °C did not show any significant change when we used hematite films with different properties. We perceived no variation on the marcasite content, detected by XRD. Conversely, when we sulfurized hematite films with different properties at 850 °C, we obtained films with different compositions. As shown in Fig. 4.14, amorphous hematite films resulted in a mix phase of pyrite and pyrrhotite with traces of marcasite, whereas hematite films oxidized at 500 °C resulted, predominantly, in pyrite with minor marcasite content and traces of pyrrhotite. Moreover, as we increased the oxidation temperature, the size of the sulfurized clusters also increased. Since the decomposition reaction does not occur homogenously across the pyrite particles, but rather start at the surface and moves toward the center, larger clusters demand more time to be fully decomposed into pyrrhotite than smaller clusters. Therefore, the difference in composition is related to the variation of the clusters size.

The replacement of pyrrhotite by pyrite and/or marcasite may follow the same unreacted core model, but may also result in the formation of several FeS_2 nuclei with no crystallographic relation to the parent pyrrhotite [19]. Hence, a pyrite particle that has been fully decomposed during sulfurization, may transform back into FeS_2 during the cooling stage (as previously discussed in the chapter) following one of the two paths: unreacted core model, or through the formation and growth of several independent nuclei. As a result, fully decomposed particles are more likely to present reminiscent content of pyrrhotite during cooling, whereas partially decomposed particles are more likely to be fully converted back into FeS_2.

Fig. 4.22 illustrates the process of decomposition and reformation of FeS_2 particles that occurs during sulfurization and cooling, respectively. We distinguish from amorphous and crystalline hematite films as precursor for sulfurization. We note that, since we observed a rapid transformation from oxide to disulfide – as shown in the results of the t_S series – we consider that every oxide particle has fully transformed into FeS_2. In Fig. 4.22 **a** we analyze the sulfurization of an amorphous hematite film, which goes through the steps: I) after being formed, pyrite begins to decompose into pyrrhotite, following the unreacted core model; II) the pyrrhotite layer advances towards the center of the unreacted pyre core, ultimately transforming every portion of pyrite into pyrrhotite; III) as the system begins to cool down, the equilibrium sulfur fugacity of the decomposition reaction drops drastically, getting lower than the sulfur partial pressure inside the Russian Doll apparatus, hence favoring the formation of pyrite nuclei inside the pure pyrrhotite particle; IV) At the end of the cooling step, several nuclei have been formed and some grew inside the pyrrhotite particle, without recovering a phase pure pyrite material. In Fig. 4.22 **b)** we analyze the sulfurization of a fully formed hematite film, which goes through similar steps: I) pyrite also starts to decompose due to the high value of the equilibrium sulfur; II) as pyrite continues to release sulfur vapor, the pyrrhotite layer formed grows toward the center of the unreacted pyrite core; III) conversely to the sulfurization of amorphous hematite, the system begins to cool down before the initial pyrite particle is fully decomposed, which causes an expansion of the unreacted FeS_2 core; IV) after cooling, pyrrhotite fully transformed back into FeS_2 due to the growth of the unreacted pyrite core, and marcasite is formed at the surface, as a result of sulfur deficiency in regions near the surface.

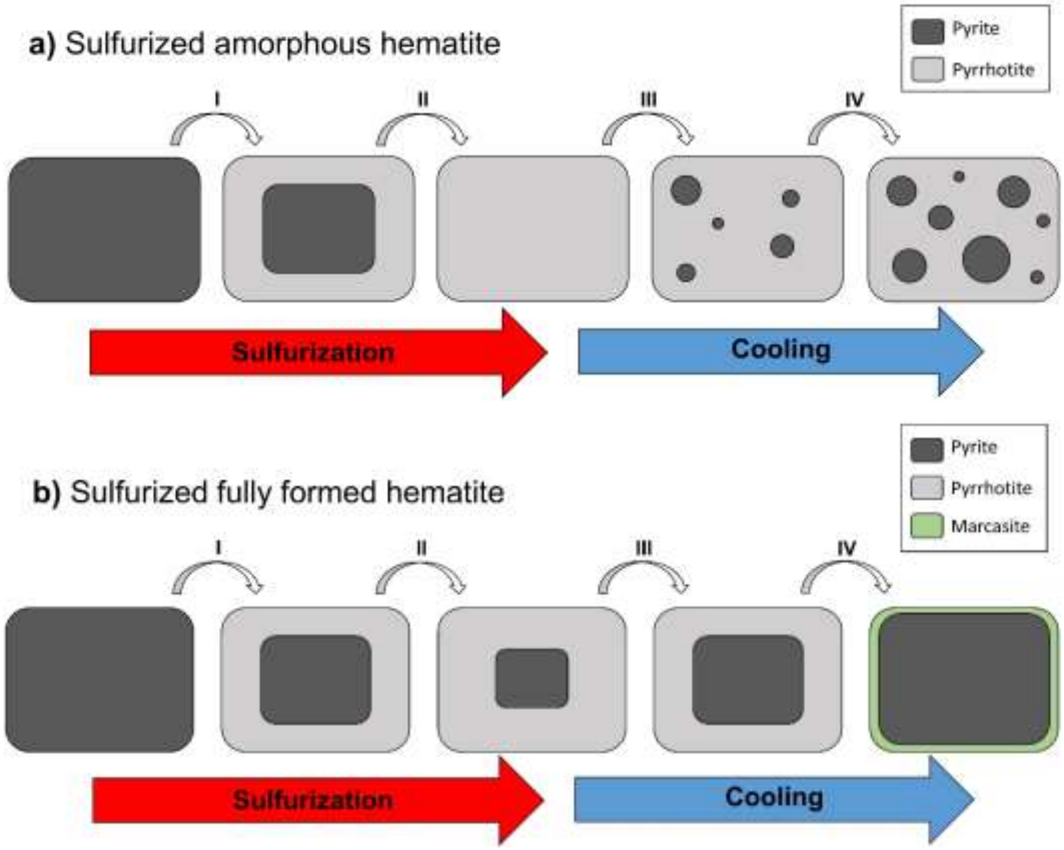

Fig. 4.22: Model to explain the difference in composition of **a)** amorphous and **b)** fully formed hematite films, when sulfurized at 850 ^{o}C.

We have stablished correlations with the microstructure of the precursor Fe_2O_3 with the resulting FeS_2 films. Therefore, we also decided to analyze the influence of the oxidation temperature on the optical properties of iron pyrite films. L.P Souza *et al* recently investigated the influence of the oxidation temperature on the microstructure and optical properties of spin-coated hematite films by SE [5]. The authors stated that increasingly oxidation temperature caused, mainly, an overall increase of the amplitude of the dielectric function (ε_1, ε_2) of hematite, and that no differences in the energy of optical transitions were observed. Such overall increase of (ε_1, ε_2) indicated a densification of the films, which is more pronounced at higher oxidation temperatures. However, when we analyzed FeS_2 films from sulfurizing both amorphous and crystalline hematite films, we observed more complex changes that could not be attributed solely to a variation in the density of the films. Contrary to the oxide case, where it is possible to model (ε_1, ε_2) of films oxidized at lower temperatures as a combination of the most dense film (oxidized at the highest temperature) and voids, we could not perform a similar modelling for pyrite.

The more profound differences observed in the dielectric function of the material may still be attributed to the optical model used, for it has not been fully optimized yet. Thus, we have begun to perform a more systematic analysis of the optical properties of pyrite, in order to understand better the changes detected, regarding the oxidation temperature of the precursor Fe_2O_3 film. Nevertheless, preliminary results shown in Fig. 4.23 show good agreement with literature data, also depicted in the graph. The literature data was extracted from the work of M.Law *et al*,[20] who investigated the optical properties of a natural and polished pyrite single crystal analyzed by SE at 77 K [20]. Even though the energy gap of pyrite is commonly thought to be ~ 0.95 eV, the SE data of both the authors of ref 20 and ourselves show non zero values of ε_2 for excitation energies below 0.95 eV. The authors in ref 20 suggested that the lack of an abrupt fundamental absorption edge may be attributed to the presence of native oxide on the surface, since the oxidation of pyrite surface may occur rapidly. However, the phenomenon is more likely related to surface defects, which may induce states within the gap, as it has been shown that such defects are also the main cause of the formation of the hole-rich inversion layer in pyrite [16]. Moreover, we noted an overall blue shift from the sulfurized amorphous oxide to the sulfurized crystalline material, and, finally, to the single crystal reported in the literature. Such blue shift may also be related to surface induced defects, since the sulfurized amorphous film resulted in smaller particles and, thus, have a higher surface to volume ration than both the sulfurized crystalline film and the single crystal. We also note that these differences may also be attributed to the presence of the hole-rich superficial layer, whose effects on pyrite optical properties have not been analyzed yet. As mentioned, we are preparing a more detailed study of pyrite optical properties, which will also include a multilayer analysis of the material, in order to identify the effect of the surface inversion layer in (ε_1, ε_2).

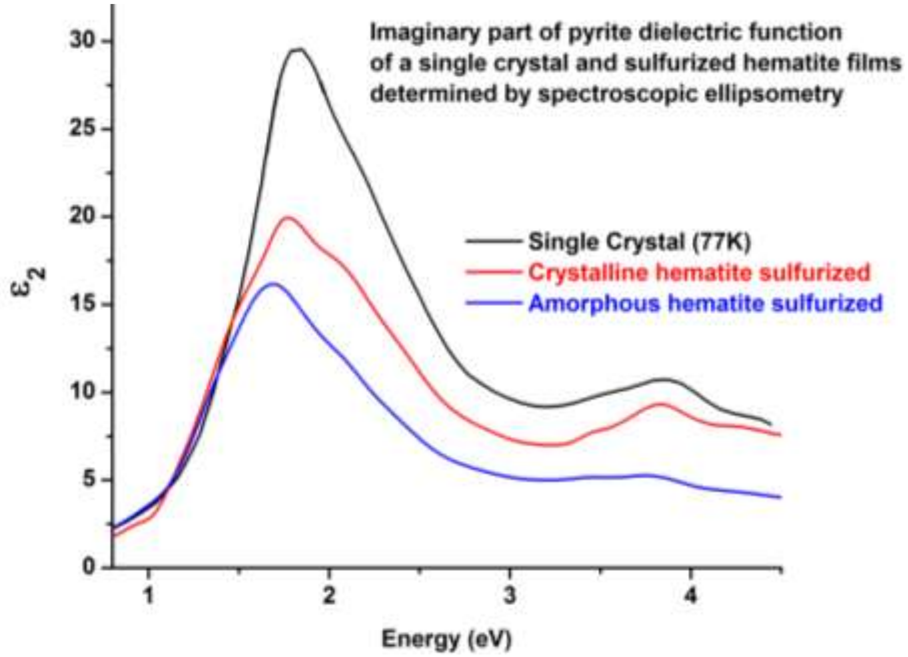

Fig. 4.23: Imaginary part of the dielectric function of a pyrite single crystal (extracted from ref 20), and pyrite films prepared by sulfurization of both crystalline and amorphous hematite films. We observed a good agreement between our model and the results extracted from the literature.

We also investigated the influence of the oxidation temperature on the electric properties of the films, and performed Hall effect measurements using the Van der Pauw method. We observed that both the amorphous and crystalline hematite films, after sulfurization, presented **n**-type conductivity, in accordance with the previous result obtained for the phase pure pyrite film obtained in the t_S series, as discussed earlier in the chapter. As shown in Table I, pyrite thin films were often reported having **p**-type behavior – in contrast with single crystal samples –, however, in 2012, C. Leighton *et al* [18] published a more detailed study of the electrical properties of FeS_2 films produced from the sulfurization of sputtered Fe films. In the study, the authors observed a crossover from **p**-type to **n**-type conductivity for increasingly sulfurization temperature, and correlated the variation in the electrical properties with changes in the microstructure of the films, as shown in Fig. 4.24. As the sulfurization temperature rose, the films became more crystalline, given by the observed increment in the intensity of the (200) peak and an enlargement of the grains. These effects on the crystal and microstructure of the films correlated well with the change in the doping character of the films, in addition to corroborate the finding of the inversion layer at the surface. Additionally, the doping type of the films for temperatures higher than 450 °C, as well as the values of both resistivity and grain size, agrees well with our results, shown in Table II. We are preparing a more detailed study of the electrical properties of the sulfurized films to better correlate with the changes in the microstructure, in view of the presence of the inversion layer.

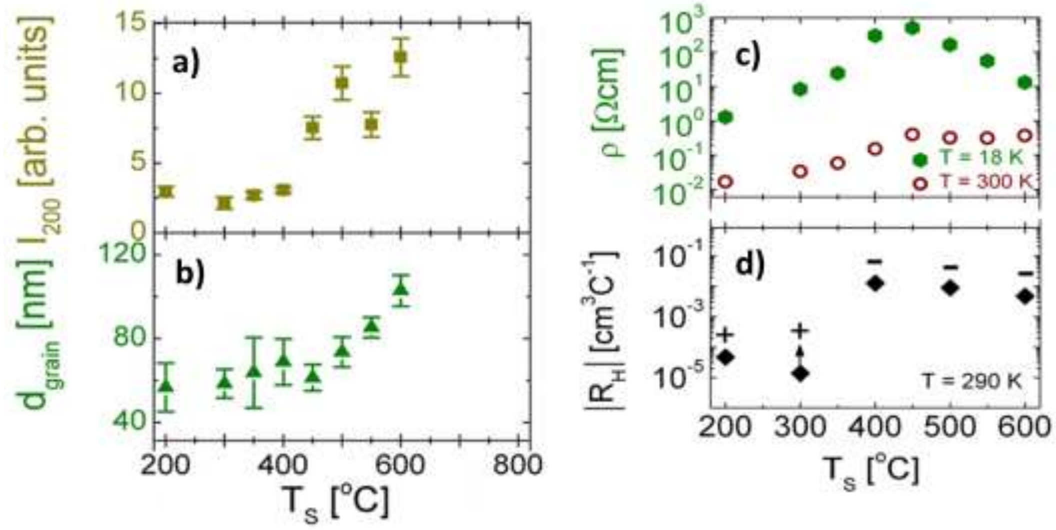

Fig. 4.24: Correlation between **a)**, **b)** changes in the crystal and microstructure, and **c)**, **d)** variations in the electronic properties of Fe films sulfurized at different temperatures. From ref [18].

Table II: Electrical properties of pyrite films prepared from sulfurization at 550 °C of iron oxide films annealed at different temperatures. The "xxxx" stems for the amorphous film who was not annealed.

T_o (°C)	T_s (°C)	ρ (Ωcm)	n (x10^{19} cm^{-3})	Doping
xxxx	550	0.37	0.96	n
500	550	1.04	7.0	n
850	550	0.74	0.69	n

Concluding, we have succeeded in obtaining good quality phase pure pyrite films, from sulfurization of spin-coated hematite films. We have defined optimum parameters to prevent the formation of secondary iron sulfide phases, plus, we have established a correlation between the microstructure of the precursor iron oxide films with the sulfurized iron disulfide films. All the films produced presented **n**-type doping, with values of resistivity and carrier concentrations that agreed well with the values found in the literature.

In the next chapter, we present preliminary results obtained regarding the production of two other metal sulfides, namely, molybdenum disulfide (MoS_2) and tin sulfide (SnS), using our Russian Doll apparatus.

References

---

1 J. Oertel, K. Ellmer, W. Bohne, J. Röhrich, H. Tributsch, J. Cryst Growth **198/199** (1999) 1205
2 M. Akhtar, A.L. Abdelhady, M.A. Malik, P.O`Brien, J. Cryst. Growth **346** (2012) 106
3 J.W. Anthony, R.A. Bideaux, K.W. Bladh, M.C. Nichols, Eds., Handbook of Mineralogy, Mineralogical Society of America, Chantilly, VA 20151-1110, USA. http://www.handbookofmineralogy.org/
4 G. Hu, K. Dam-Johansen, S. Wedel, J.P Hansen, Progr. En Combust. **32** (2006) 295
5 L.P. de Souza, R.O. G. Chaves, A. Malachias, R. Paniago, S.O. Ferreira, A.S. Ferlauto, J. Appl. Phys. **119** (2016) 245104
6 F.K. Lotgering, J. Inorg. Nucl. Chem. **9** (1959) 113
7 F. Gronvold, E.F. Westrum Jr, J. Chem. Thermodynamics **8** (1976) 1039
8 M.E Fleet, Canadian Mineralogist, **10** (1970) 225
9 A.R. Lennie, D.J. Vaughan, Americ. Miner. **77** (1992) 1166
10 J.W. Christian, The theory of transformations in metals and alloys Part I: Equilibrium and general kinetic theory (2nd edition), Oxford, England: Pergamon Press, 1975
11 P. Toulmin III, P.B. Barton Jr, Geochim Cosmochim Acta **28** (1964) 641
12 Y. Hong, B.Fegley, Planet.Space Sci. **46** (1998) 683
13 L.V. Gurvich, I.V. Veyts, C.B. Alcock. Thermodynamic properties of individual substances. Part 2, vol. 1, 4th ed. New York: Hemisphere; 1989.
14 M.J. Buerger, Am. Mineral. **19** (1934) 37
15 M. Limpinsel, N. Farhi, N. Berry, J. Lindemuth, C.L. Perkins, Q. Linf, M. Law, Energy Environ. Sci., **7** (2014) 1974
16 J.M. Lambert, G. Simkovich, P.L. Walke. Metall Mater Trans B **29** (1998) 385.
17 B. Fegley, K. Lodders. Icarus **115** (1995) 159
18 X. Zhang, M. Manno, A. Baruth, M. Johnson, E.S. Aydil, C. Leighton, ACS Nano **7** (2013) 2781
19 G. Qian, F. Xia, J. Brugger, W.M. Skinner, J. Bei, G. Chen, A. Pring, Am. Mineral. **96** (2011) 1878
20 S.G. Choi, J. Hu, L.S. Abdallah, M. Limpinsel, Y.N. Zhang, S. Zollner, R.Q. Wu, M. Law, Phys. Rev. B **86** (2012) 115207

5 Other Metal Sulfides

In this chapter, we present preliminary results regarding the synthesis of metal sulfides using our Russian Doll apparatus. Two materials were tested, both produced by sulfurization: MoS_2 and SnS. The former has been widely studied due to its layered structure, whose properties may be tuned by varying the number of layers of the material and with a careful choice of substrate, providing the material with high potential use in electronics and optoelectronics. The later has been regarded as a potential material for solar energy conversion due to favorable optical properties. In addition, SnS has intrinsic **p**-type doping, which enables the material to be used conjointly with our **n**-type pyrite, in heterojunction based photoactive devices.

5.1 MOLYBDENUM DISULFIDE – MoS_2

In recent years, much research has been performed with two dimensional (2D) materials, such as graphene, boron nitride (BN), and transition metal dichalcogenides (TMD), due to their suitability for application in electronics and optoelectronics [1]. Amongst these materials, MoS_2 stands out because of the possibility to tune its properties through control of the number of layers or by careful selection of substrates [2]. Despite the intrinsic **n**-type electronic behavior of MoS_2, advances have been achieved regarding **p**-doping using, for example, Nb, $AuCl_3$, and P. [3,4,5]. In fact, recently, it was reported a **p-n** homojunction of intrinsic **n**-doped MoS_2 with **p**-doped MoS_2 using $AuCl_3$ [4]. The high optical absorption coefficient over the visible region of the radiation spectrum, combined with a suitable band gap value between 1.2 – 1.8 eV, also makes MoS_2 a promising material for photoconversion devices [2,6]. The most used techniques to produced MoS_2 remain mechanical and chemical exfoliation and CVD, but many authors have reported high quality films produced by sulfurization of Mo, even enabling control over thickness and number of layers [1,7,8,].

We prepared thin films of MoS_2 by sulfurizing sputtered metallic Mo thin films. The precursor Mo films were grown in a RF DC magnetron sputtering with 50 W power, chamber pressure of 3 mTorr, 10 sccm argon flow, without heating the substrates. We used both glass and silicon as substrates in each deposition. We controlled the films thickness by varying the deposition time, assuming a constant deposition rate, estimated by the determining the final thickness. Films deposited for 10 min presented a final thickness of approximately 10 nm, as determined by SE. We also deposited Mo films for 2 min, which, considering a constant deposition rate, resulted in 2 nm thick films. The films were extremely smooth, with roughness values lower than 1 nm, also determined by SE. The Mo films were sulfurized using the Russian Doll apparatus, with 15 mg of sulfur powder, at 550 ^{o}C and a heating rate of 10.5 ^{o}C/min, for 2 hours. XRD experiments – Fig. 5.1 **a** and **b** – suggests that the Mo films deposited on glass and Si were both fully sulfurized into MoS_2, with small crystallites, given by the large width of the XRD peaks, which overlapped in some occasions. However, due to the low number of XRD peaks, one may not affirm so strongly that the resulting phase is, indeed, MoS_2. Still, we analyzed the overlapped peaks with a pseudo Voigt function, and with the obtained values of the full width at half maximum (FWHM), we estimated the order of the crystallite sizes by means of the Scherer equation. The experimental data of the isolated peaks and the fitted curves with the resulting parameters are shown in Fig. 5.1 **c**, and **d**. Both films presented an average crystallite size in the order of 10 nm.

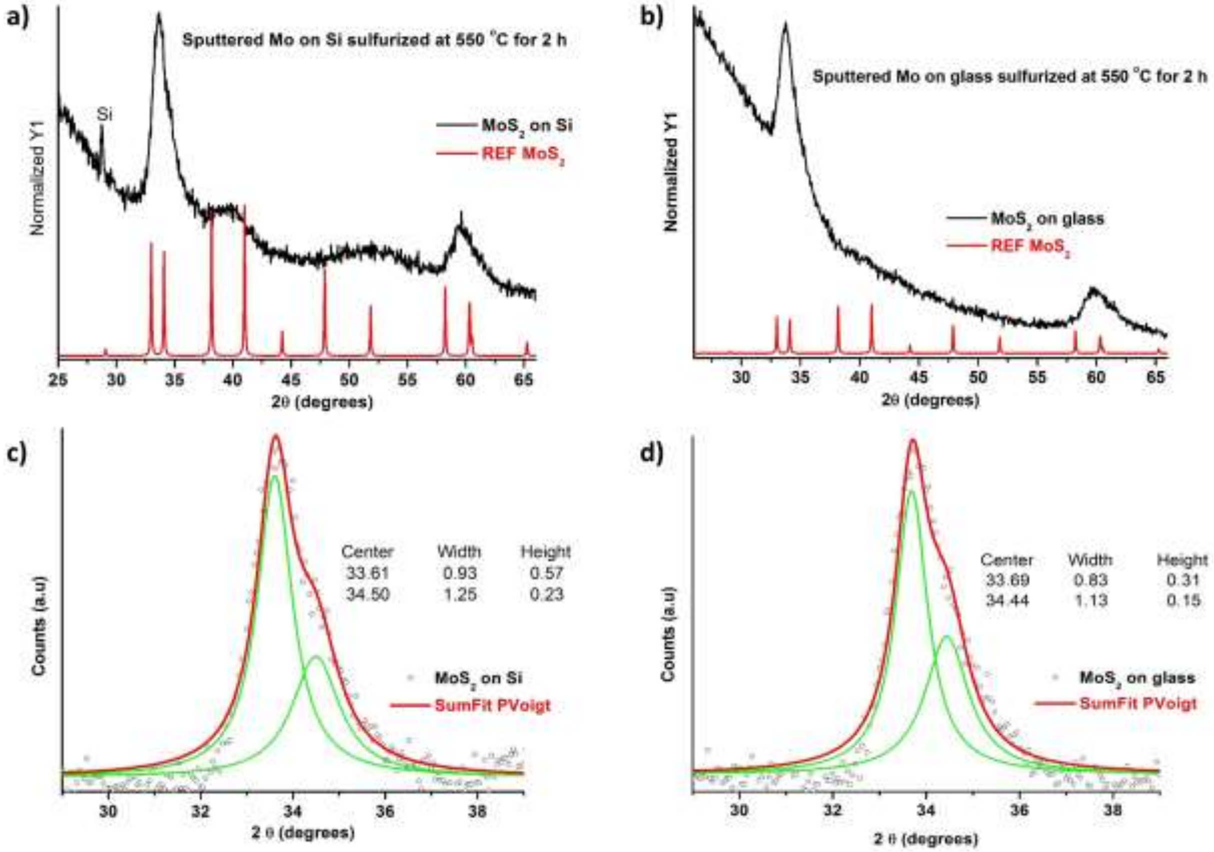

Fig 5.1: XRD patters of sputtered Mo films, sulfurized at 550 °C for 2 hours using the Russian Doll apparatus, with the modeling Pseudo Voigt curve used to extract the value of the FWHM to calculate the average crystallite size. **a)** and **c)** represent films deposited on Si, whereas **b)** and **d)** represent films deposited on glass. The values of the FWHM in both cases were very close.

It has been reported that the Raman shift of MoS$_2$ is related to the number of layers of the materials, according to the relative positon of two vibrational modes – A_{1g} and E^1_{2g} [7,9]. Fig. 5.2 **a** displays the measured Raman shifts of the 10 nm Mo film sulfurized on glass substrate, as well as MoS$_2$ reference samples with varying number of layers up to bulk material. The MoS$_2$ reference samples were supplied by MsC Bruno Carvalho of the Raman Laboratory of UFMG, who also performed the experiments. The dashed line represents the difference in the peak positions of the monolayer sample from the bulk sample. Fig. 5.2 **b)** shows the difference in the A_{1g} and E^1_{2g} MoS$_2$ vibrational modes for every sample, indicating the sulfurized film approaches the bulk case. MoS$_2$ produced from sulfurization of Mo is, typically, twice as thick as the precursor metallic films [10].

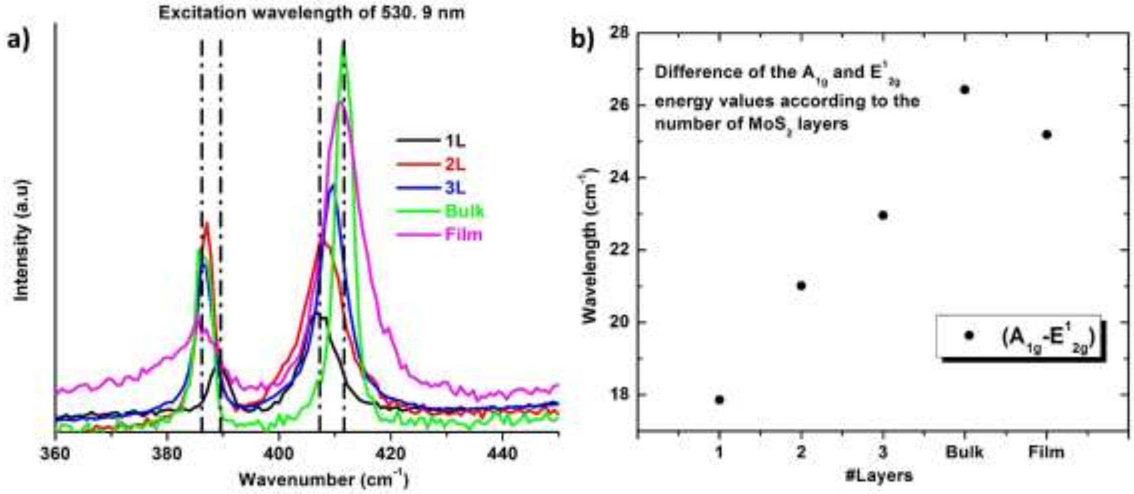

Fig. 5.2: **a)** Raman shift of MoS_2 produced by sulfurization of sputtered Mo at 550 ºC for 2 h (Mo_S_2h). Also shown are the Raman shifts of bulk MoS_2, as well as MoS_2 with 1-3 layers. **b)** Difference of the A_{1g} and E^1_{2g} energy values according to the number of MoS_2 layers. As observed, the sulfurized material approaches the bulk case.

SEM images of the films prepared on glass substrates exhibit a peeling effect of the films after sulfurization (Fig. 5.3). As mentioned earlier in the chapter, the sputtered Mo films were homogenous and presented extremely smooth surfaces, however, after being sulfurized in the Russian Doll apparatus, we observed, spread over the entire surface of the films, cracks resulted from the mentioned peeling effect. We attribute such phenomenon to a combination of two properties of the precursor Mo film: **i)** poor adhesion to the substrate, which has been observed by some authors as correlated with the deposition conditions of sputtered Mo, enabling the films to be peeled off during sulfurization as a result of **ii)** strain across the film, which has also been associated with the Mo sputtering conditions, and whose effects is boosted by the sulfurization process, due to the growth of the primitive cell as Mo transforms into MoS_2 – as mentioned, MoS_2 doubles the thickness of Mo after sulfurization [11].

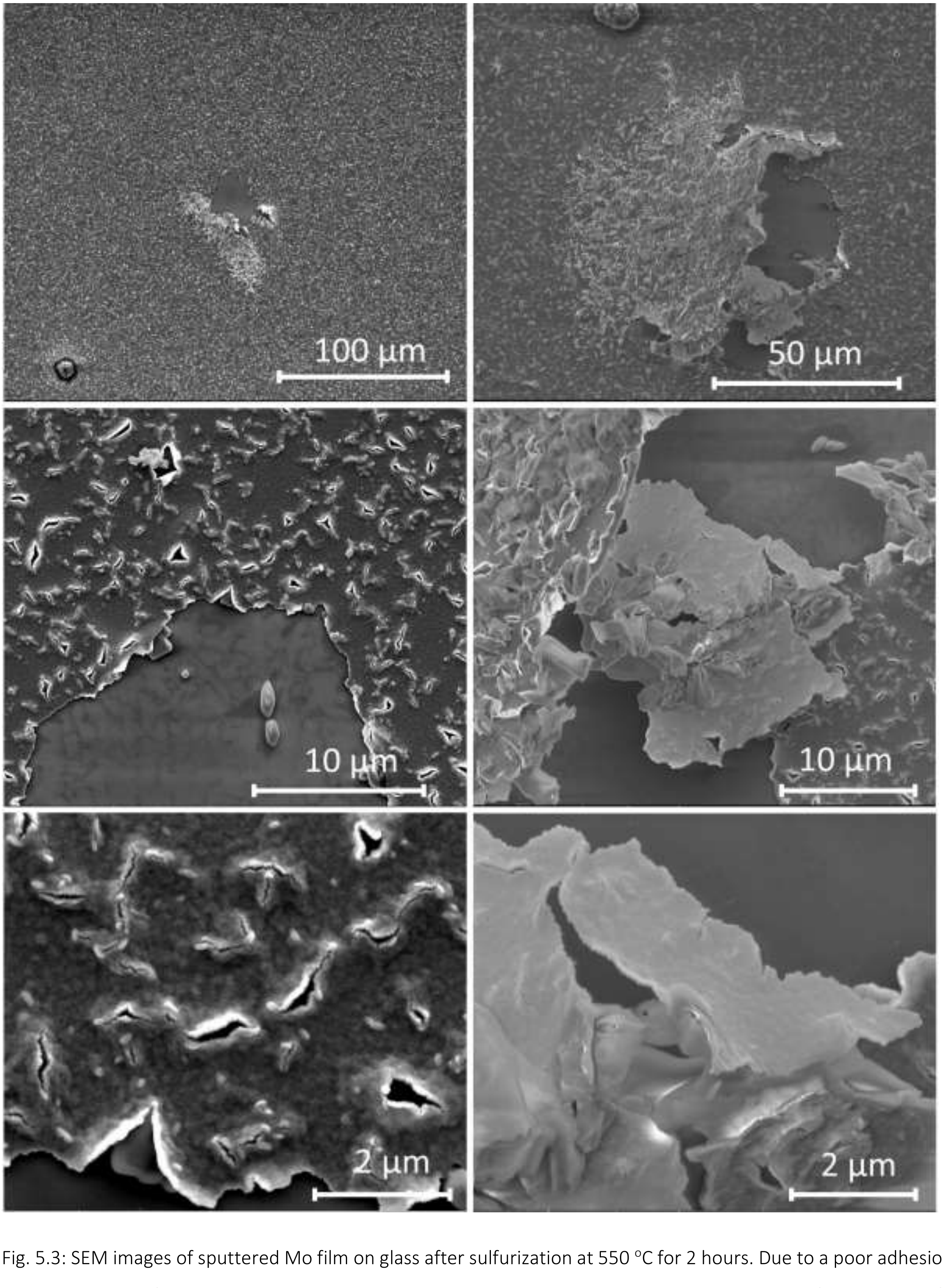

Fig. 5.3: SEM images of sputtered Mo film on glass after sulfurization at 550 °C for 2 hours. Due to a poor adhesion of the precursor Mo film to the substrate, and strain, which was enhanced during the enlargement of the volume of the primitive cell, the MoS_2 film was peeling off the substrate.

We also sulfurized a thinner Mo film, which was sputtered in the same conditions, however for 2 minutes only. As discussed, we estimated that such film, considering that the rate deposition was kept approximately constant, had a final thickness close to 2 nm. We measured the Raman shift of the films and, as previously done, we compared with Raman shifts of MoS_2 reference samples with layers from 1-3 and a bulk material. The results displayed in Fig. 5.4 reveals that, according to the energy value of the A_{1g} mode, the film behaves closely to a 3 layered MoS_2, conversely to the bulk scenario obtained when we sulfurized a 10 min sputtered Mo film. However, the energy value of the E^1_{2g} mode was rather too low, lower than the bulk material – similarly to what had been noted for the 10 min Mo film, as displayed in table I – yet the 2 min sulfurized Mo presented an even lower value. The results of the Raman experiments are summarized in Table III. Also, Fig. 5.4 shows that the film had good homogeneity, for the positions and intensity of the peaks were very similar when measured in different regions of the sample (middle and border).

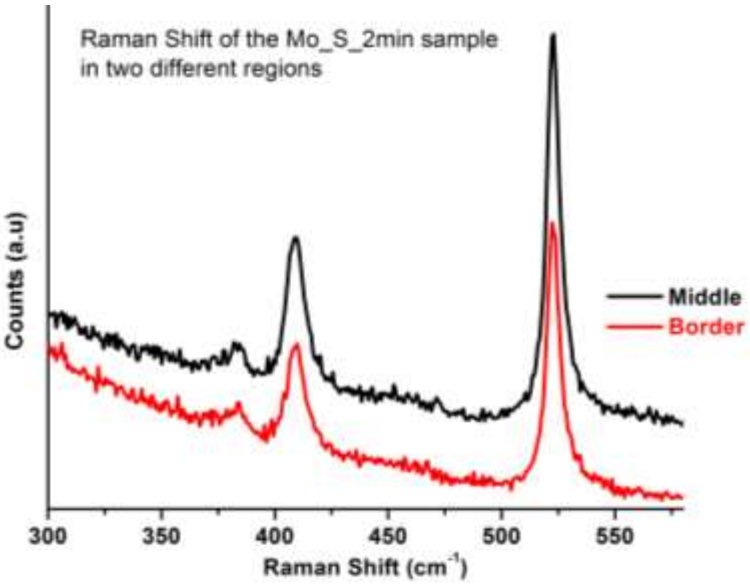

Fig. 5.4: Raman shift of a MoS_2 film prepared by sulfurizing a 2 nm thick metallic Mo film, deposited by sputtering. The Raman signal was collected in two different regions, to verify the homogeneity of the sample.

Table III: Raman shift values of the E_{2g} and A_{1g} MoS_2 modes of different layered MoS_2 samples, as well as of films produced by sulfurization of Mo films with different thickness.

Sample	**E^1_{2g} position (cm^{-1})**	**A_{1g} position (cm^{-1})**	**ΔE_{modes} (A_{1g} - E^1_{2g})**
1 Layer	389.273	407.136	17.863
2 Layers	386.949	407.695	21.016
3 Layers	386.586	409.548	22.962
Bulk	386.482	411.673	26.435
Mo_S_10min	384.973	411.408	25.191
Mo_S_2min	383.307	409.174	25.867

Many authors have studied the effect of strain in the properties of MoS_2 and some reported its correlation with a decrease in the energy of the E^1_{2g} vibrational mode, leading, in more extreme cases of strain, to a degeneracy break of the mode. Thus, the MoS_2 films we produced from sulfurization are indeed strained, as expected, due to the strained nature of the precursor sputtered Mo, and as mentioned, is one of the reasons the films is peeling off.

Concluding, we have managed to produce MoS_2 by sulfurization of metallic Mo, deposited by sputtering. Sputtering deposition times of 10 min and 2 min have resulted, after sulfurization, in MoS_2 films with approximately 20 nm and 4 nm, respectively. The thicker film has a characteristic bulk Raman shift, whereas the thinner one approaches a three layered material. Nevertheless, the synthesis still needs to be optimized in order to prevent the films from peeling off, which generates cracks on the surface and would lead to eventual poor electrical properties. Amongst other strategies to do so, promptly we will sulfurize films with lower sulfur concentrations – in an attempt to decrease the sulfurization rate, which may be enhancing the strain in the MoS_2 films – as well as increase the sulfurization temperature, as higher quality films are normally produced under such conditions [7,8]. Moreover, we will deposit Mo films with higher pressures, in order to increase the adhesion of the precursor Mo to the substrate, also in an attempt to lessen the strain and prevent the formation of cracks [11].

TIN SULFIDE – SNS

Tin (II) monosulfide, similarly to FeS_2, has huge potential in solar cell applications, due to favorable optical and electronic properties [12,13,14]. For example, SnS has a high optical absorption coefficient – higher than CdTe – and an effective optical onset – 1.4 eV – close to the optimum band gap value for maximum efficiency, determined by the Schockley-Queisser limit [12]. SnS presents intrinsic **p**-type doping resulted from tin vacancies whose origin is still matter of discussion amongst researchers [12]. Moreover, up to this point, the higher light-to-electricity efficiency reported for SnS devices is still less than 2.0 %. Nevertheless, the favorable properties of this semiconductor, combined with its intrinsic **p**-type conductivity, make it a suitable option for building heterojunction based photoactive devices with our produced n-doped pyrite films.

We deposited thin films of tin oxide by spin coating, following the same procedure used to deposit hematite thin films, described in chapter 2. We prepared a 0.5 M solution of tin (IV) chloride ($SnCl_4$) and ethanolamine in 2-methoxyethanol, and spin-coated the solution on glass substrates. Then, the films were heated in a hot plate at 300 ^oC to evaporate the solvent and later annealed at 500 ^oC for 30 min. The resulting tin oxide films presented solely the Tin (IV) oxide, SnO_2, structure, as shown in Fig. 5.5.

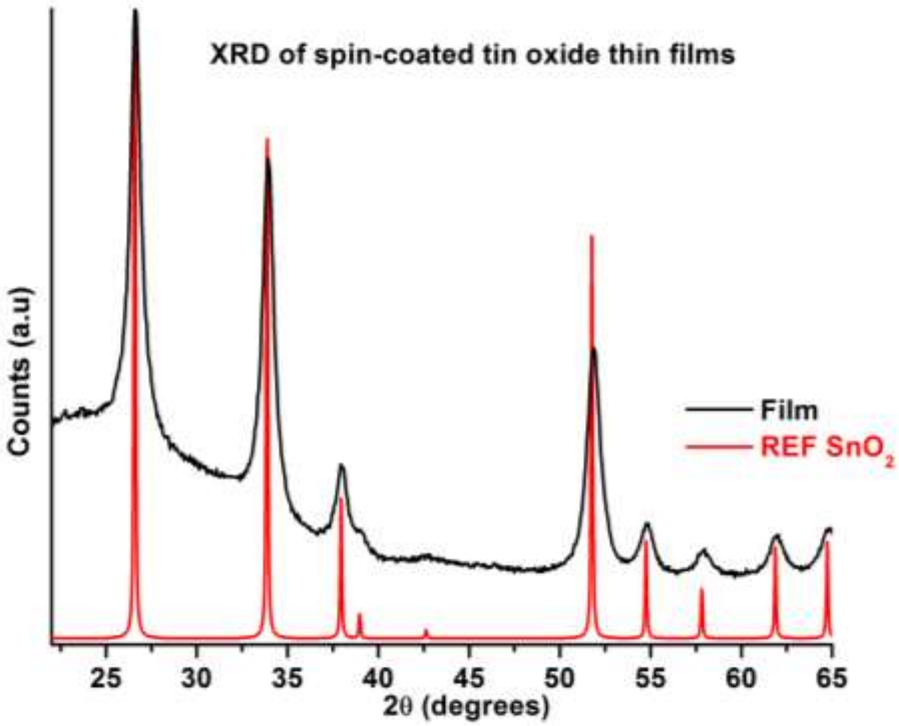

Fig. 5.5: XRD pattern of a spin-coated tin oxide film, annealed at 500 °C for 30 minutes. The formed oxide has tin (IV) oxide – SnO_2 – structure.

Later, we sulfurized a spin-coated SnO_2 film using our Russian Doll apparatus at 550 °C for 2 hours, firstly, with 5 mg of sulfur powder, at a heating rate of 10.5 °C/min. The sulfurization of SnO_2 may occur through either reaction 5.1 or 5.2, depending on the presence or not of H_2 in the atmosphere [15]. In our case, the atmosphere was H_2 free, thus the reaction followed eq. 5.1.

$$SnO_2(s) + 1.5S_2(g) \rightarrow SnS_2(s) + SO_2(g) \qquad [5.1]$$

$$SnO_2(s) + 1.5S_2(g) + H_2(g) \rightarrow SnS(s) + SO_2(g) + H_2S(g) \qquad [5.2]$$

Fig 5.6 unveils that, after sulfurization, SnO_2 underwent a phase transformation to a mix composition of SnS_2 and Sn_2S_3. P. Scardala *et al* studied decomposition reactions of every tin sulfide phase, meaning, SnS_2, Sn_2S_3, and SnS, and reported the following reaction equations [16]:

$$SnS_2(s) \rightarrow \frac{1}{2}Sn_2S_3(s) + \frac{1}{4}S_2(g),\ \Delta H^0 = 54.5\ \text{kJ/mol} \qquad [5.3]$$

$$Sn_2S_3(s) \rightarrow 2SnS(s) + \frac{1}{2}S_2(g),\ \Delta H^0 = 112.0\ \text{kJ/mol} \qquad [5.4]$$

$SnS(s) \rightarrow SnS(g)$, $\Delta H^0 = 220.0$ kJ/mol [5.5]

Equations 5.1-3 above states that, during heating, SnS_2 starts to release sulfur gas, transforming, first, into Sn_2S_3, which presents both oxidation states of tin, Sn (II) and Sn (IV), and later to SnS, in which Sn has only the lowest oxidation state. The presence of both SnS_2 and Sn_2S_3 phases in the sulfurized film indicates, then, that sulfur partial pressure was low enough for partial SnS_2 to occur, and a further decrease in its value could lead to SnS formation, as a result of a more advanced stage of SnS_2 decomposition.

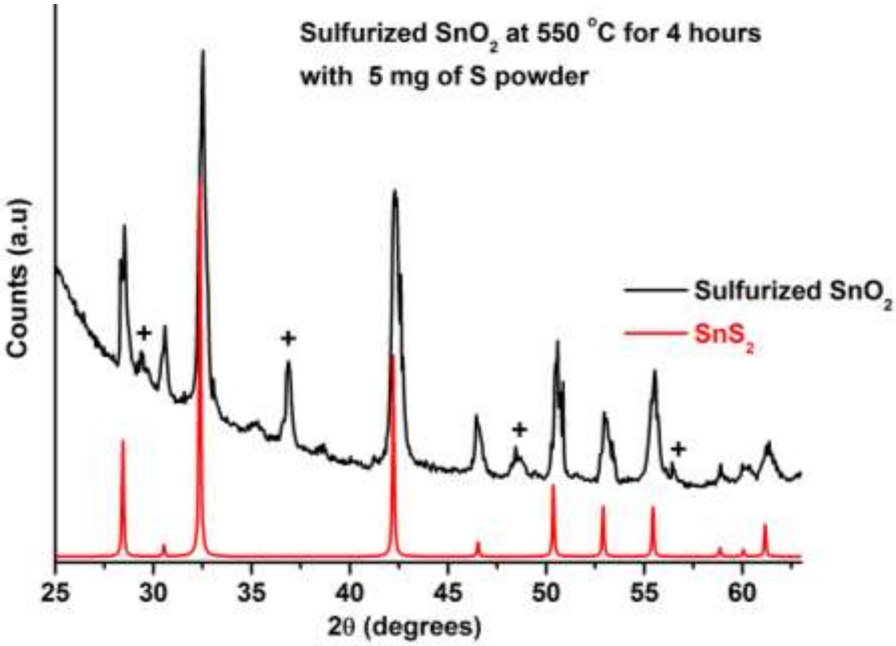

Fig. 5.6: XRD pattern of SnO_2 film sulfurized at 550 °C for 4 hours with 5 mg of sulfur powder. Crosses represent XRD peaks of Sn_2S_3, indicating the sulfurized films is composed by a SnS_2 and Sn_2S_3 mix phase.

In order to decrease the sulfur partial pressure during sulfurization, we prepared a new experiment with a lower concentration of sulfur powder, in an attempt to promote decomposition of the formed phases SnS_2 and Sn_2S_3. The sulfurization, as well as the oxide deposition conditions, were, then, repeated with 1 mg of sulfur powder. However, as Fig. 5.7 shows, we did not succeed in obtaining the SnS phase, but conversely, the sulfurized film presented even less content of the Sn_2S_3 phase, evidenced by the decrease in the relative peak intensities between both phases.

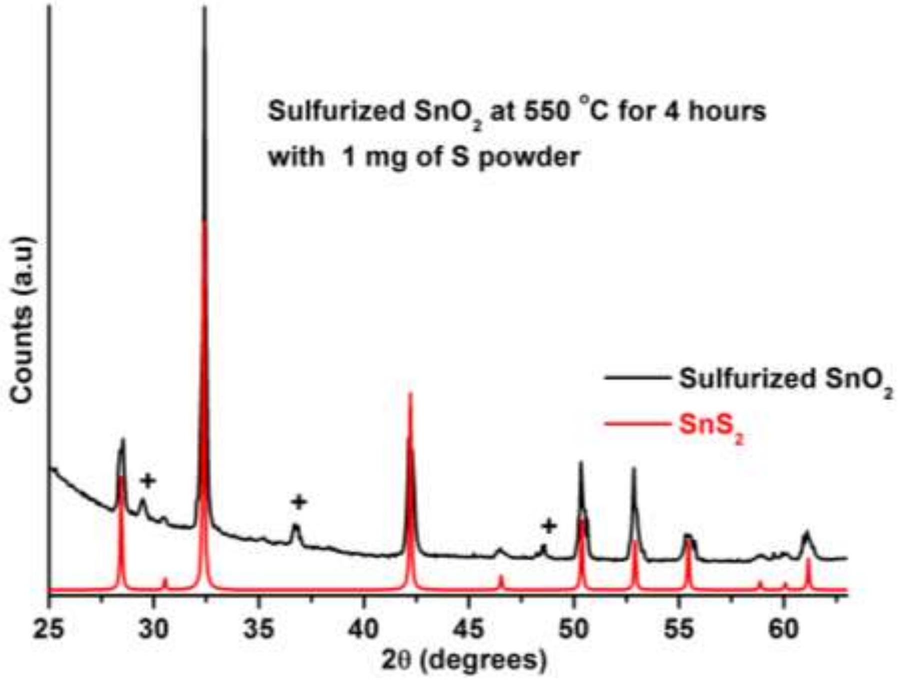

Fig 5.7: XRD pattern of SnO_2 sulfurized at 550 °C for 4 hours with 1 mg of sulfur powder.

We did not succeed yet in obtaining a pure phase SnS thin film, however, preliminary results achieved so far are rather promising. Up to this point, every sample prepared presented the sulfur rich phase sulfide, SnS_2, which has the highest oxidation state of tin. Such phase, along with the intermediate Sn_2S_3, have been reported as **n**-type semiconductors, and neither are as appealing as the tin monosulfide, in the context of solar energy conversion [12]. Moreover, the presence of such phases in otherwise dominant SnS films, have been appointed as one of the reasons for the low light-to-electricity conversion in SnS based devices, meaning that it is utterly important to learn how to prevent their formation [12]. In order to produce pure phase high quality SnS films, we will try replacing Sn (IV) chloride for Sn (II) chloride in the spin coating solution, which, for having the same oxidation state of tin in SnS, it may favor the formation of the monosulfide phase; and increase sulfurization time and temperature. The former may eventually lead to the formation of SnS due to decomposition of the other sulfide phases, described by equations 5.1-3, whereas the later may speed up such decomposition reaction, whilst also promoting particle growth. All of these experiments are currently under progress in the Laboratory of Nanomaterials. We hope to dominate the production of good quality pure phase SnS films, in order to produce self-assembled SnS-FeS_2 heterojunction, by simultaneously sulfurizing tin and iron oxide precursors, as illustrated in Fig. 5.8.

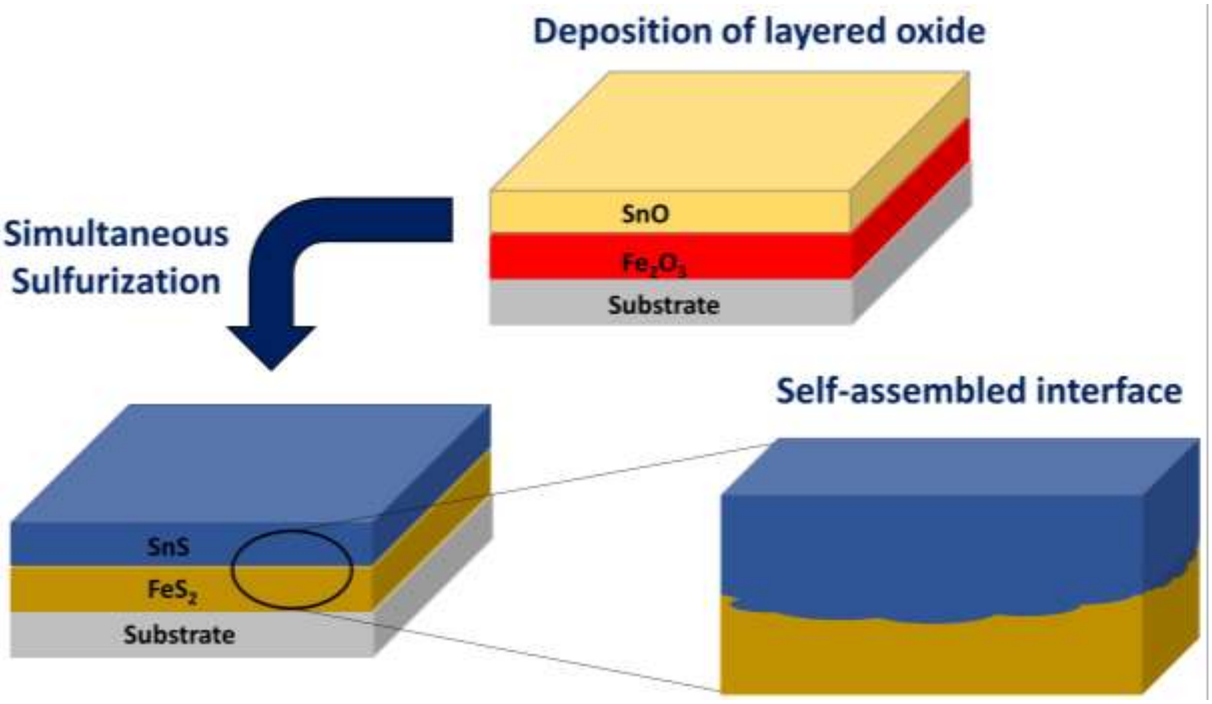

Fig 5.8: Proposed self-assemble SnS-FeS_2 heterojunction, to be used in photoactive solar cells.

References

---

1 K. Lee , R. Gatensby , N. McEvoy , T. Hallam , G.S. Duesberg, Adv. Mater. **25** (2013) 6699
2 C. Yim, M. O'Brien, N. McEvoy, S. Winters, I. Mirza, J.G. Lunney, G.S. Duesberg, Appl. Phys. Lett. **104** (2014) 103114
3 M.R. Laskar, D.N. Nath, L. Ma, E.W. Lee II, C.H. Lee, T. Kent, Z. Yang, R. Mishra, M.A. Roldan, J. Idrobo, S.T. Pantelides, S.J. Pennycook, R.C. Myers, Y. Wu, S. Rajan, Appl. Phys. Lett. **104** (2014) 092104
4 M.S. Choi, D. Qu, D. Lee, X. Liu, K. Watanabe, T. Taniguchi, W.J. Yoo, ACS Nano **8** (2014) 9332
5 A. Nipane, D. Karmakar, N. Kaushik, S. Karande, S. Lodha, ACS Nano **10** (2016) 2128
6 A. Castellanos-Gomez, M. Barkelid, A.M. Goossens, V.E. Calado, H.S.J. van der Zant, G.A. Steele, Nano Lett. **12** (2012) 3187

---

7 C.M. Orofeo, S. Suzuki, Y. Sekine, H. Hibino, Appl. Phys. Lett. **105** (2014) 083112

8 Y. Zhan, Z. Liu, S. Najmaei, P.M. Ajayan, J.Lou, Small **8** (2012) 966

9 M.A. Pimenta, E. del Corro, B.R. Carvalho, C. Fantini, L.M. Malard, Acc. Chem. Res. **48** (2015) 41

10 S.H. El-Mahalawy, B.L. Evans, J. Appl. Cryst. **9** (1976) 403

11 J.H. Scofield, A. Duda, D. Albin, B.L. Ballard, P.K. Predecki, Thin Solid Films **260** (1995) 26

12 L.A. Burton, D. Colombara, R.D. Abellon, F.C. Grozema, L.M. Peter, T.J. Savenije, G. Dennler, A. Walsh, Chem. Mater. **25** (2013) 4908

13 S.A. Bashkirov, V.F. Gremenok, V.A. Ivanov, V.V. Lazenka, K. Bente, Thin Solid Films **520** (2012) 5807

14 O.E. Ogah, G. Zoppi, I. Forbes, R.W. Miles, Thin Solid Films **517** (2009) 2485

15 J.C. Park, K.R. Lee, H. Heo, S.H. Kwon, J.D. Kwon, M.J. Lee, W. Jeon, S.J. Jeong, J.H. Ahn, Cryst. Growth Des. **16** (2016) 3884

16 V. Piacente, S. Foglia, P. Scardala, J. Alloy Compd. **177** (1991) 17

6 Conclusions & Perspectives

In this chapter, we summarize the main results obtained throughout the work, and express our conclusions accordingly. Moreover, we stress the next steps to be taken, regarding the study of the optoelectronic properties of pyrite films, as well as the synthesis of other metal sulfides using our Russian Doll apparatus. We highlight the production of **p**-type sulfides, to be used conjointly with pyrite films in heterostructured devices.

6.1 CONCLUSIONS

We studied the band alignment at the interface of CdS nanoparticles with MWCNTs, by means of photoelectron spectroscopies. We used E_f as a reference level energy, imposing the same value for every sample by grounding the samples to the detector. We observed a metallic character of the MWCNTs and determined the position of the valence band maximum of bulk CdS by UPS, obtaining a value of 2.3 eV. We determined E_g of the decorating CdS nanoparticles by diffuse reflectance, and obtained 2.45 eV, which is in accordance with the literature. Subtracting E_{VBM} from E_g, we determined 0.15 eV as the position of E_{CBM} of the CdS NPs. Finally, we measured the shifts of Cd and S core levels when measured in bulk and near interface CdS by XPS, which were -0.2 eV, indicating a downward band bending of CdS at the interface with MWCNTs. Then, we determined the position of the conduction band minimum at the CdS/MWCNTs interface, and observed a zero energy potential barrier between the conduction band of CdS and E_f of the MWCNTs, evidencing the formation of an ohmic contact.

We built an AACVD reactor to produce FeS_2 films from FeDTC molecules, synthesized in the Chemistry Department of UFMG. We varied several deposition parameters in order to obtain pure phase iron pyrite films, however unsuccessfully. We could, but, produce films with mix composition of pyrite and pyrrhotite, when we used highly concentrated solutions and the process occurred at 325 ^{o}C, which was the lowest deposition temperature – since lower temperatures did not result in film growth. Because the films grown in the homemade AACVD reactor had sulfur deficiencies, we established routes to sulfurize the mix phase iron sulfide films, which were also tested on spin-coated hematite films. After a few trials, we optimized the sulfurization process by implementing a new apparatus, which we named Russian Doll, due to its resemblance to the Matrioska toy. We, thus, implanted a three-step process to produce FeS_2 films, which consisted in: i) spin coating Fe_2O_3 films; ii) annealing of the spin-coated film; and iii) sulfurization of the annealed film.

We studied the influence of the synthesis parameters on the phase composition and the microstructure of the pyrite films. We observed the formation of both FeS_2 polymorphs – cubic pyrite and orthorhombic marcasite – in early stages of the sulfurization process, with a dominance of cubic pyrite. Nevertheless, as the process continued, the orthorhombic marcasite underwent a transformation reaction to the cubic phase which was completed after 4 hours, when pure phase pyrite films were obtained. We also observed that the transformation reaction was boosted when we increased the sulfurization temperature from 450 ^{o}C to 550 ^{o}C, which is in accordance with reports from the literature.

We attempted to increase the size of the particles by further increasing the sulfurization temperature above 550 ^{o}C. However, we observed that the pyrite particles coalesced into isolated clusters (evidenced by charging effects observed during SEM imaging), forming cracks in the films. The formation of cracks is undesirable, since it results in films with poorer electric properties. In addition, marcasite was detected in the final composition of the films sulfurized at higher temperatures. The orthorhombic FeS_2 phase was evidenced by the presence of both marcasite XRD peaks and the formation of cockscomb shaped structures (typical marcasite crystal habit) on the surface of the clusters. We correlated the formation of marcasite in such conditions with the decomposition reaction of pyrite, which produces pyrrhotite and S_2 vapor. The lack of pyrrhotite XRD peaks indicates that the inverse reaction must have occurred during cooling. Moreover, the presence of the cockscomb structures on the surface of the coalesced clusters corroborates results in the literature regarding a slight difference in the stoichiometry between pyrite and marcasite. We also raised the duration of the sulfurization process, producing films at 550 ^{o}C, for

8 and 16 hours. Such films were almost completely, and completely decomposed into pyrrhotite, respectively, as a consequence of the continuous outward sulfur flow in our apparatus. Therefore, we established an enclosing limit time for our Russian Doll apparatus.

We studied the influence of the properties of the precursor iron oxide films in the resulting disulfide material, varying the parameters of the oxidation process. We noted that films oxidized at higher temperatures resulted in FeS_2 films with larger particles. Since the grains of the hematite films also grow for increasing annealing temperature, our findings established a correlation between the microstructure of the precursor Fe_2O_3 with the sulfurized FeS_2 films. Additionally, pyrite films produced from amorphous hematite films decomposed more easily than films produced from crystalline hematite films, when they were sulfurized at temperatures higher than 550 ^oC, which further strengthened the correlation between both materials. We also started to investigate the effect of different oxidation temperatures in the optical properties of the sulfurized films by means of spectroscopic ellipsometry. Preliminary results showed a more profound change in pyrite dielectric function with the oxidation temperature, when compared to hematite. Conversely to the oxide case, we could not correlate the variations in the dielectric function of pyrite solely to a densification of the films, or other microstructure variation, alone. Nevertheless, we stress that the optical model was not optimized for the pyrite case yet.

All the pure phase pyrite films we produced presented **n**-type behavior, as determined by Hall effect experiments, using the Van der Pauw method. This result, according to the literature guarantees our films have good quality, as the effect of the superficial inversion layer was minimized. We found no correlation between pyrite films prepared from Fe_2O_3 with distinct crystallinity.

We obtained promising preliminary results regarding the synthesis of other metal sulfides, using our Russian Doll apparatus. Even though MoS_2 has been detaching from the substrate during the sulfurization, we believe that by optimizing the sputtering process and increasing the sulfurization temperature we will be able to prevent such phenomenon. Additionally, we started to study the Sn:S system, in order to produce SnS, which is an intrinsic **p**-type semiconductor, which could then, be used to build a **p-n** heterojunction with FeS_2 without the need for extrinsic doping. However, in the first few trials, we obtained either SnS_2 or a mix of Sn_2S_3 with SnS_2.

6.2 PERSPECTIVES

We have established a route to produce good quality **n**-doped pure phase pyrite films. We observed variations in the dielectric function of pyrite when the oxidation temperature of the precursor hematite film was changed. We will study systematically the optical properties of pyrite films, possibly correlating with the presence of the superficial inversion layer, which has been assigned as the main reason for the low values of V_{OC}.

We will also continue the study of the synthesis of isolated SnS and MoS_2, in the interest of optimizing the processes. We will change synthesis parameters to prevent MoS_2 films from peeling off the substrate. We will also study the correlation between the strain regime of the precursor Mo films with the sulfurized films. We will also pursue the production of good quality pure phase SnS films, in order to produce a **p-n** heterojunction with pyrite. We hope to use such heterojunction in photoactive devices.

I APPENDIX A

"Determination of the band alignment of multi-walled carbonnanotubes decorated with cadmium sulfide". Silva, MFO *et al*, Applied Surface Science, **321** (2014) 283 – 288

Abstract

Many authors have already succeeded on decorating carbon nanotubes with semiconductor (SC) nanoparticles (NPs), however little is still known about the resulting interfaces. In this work, we determined the band alignment of CdS NPs and metallic MWCNTs by means of Photoelectron Spectroscopy measurements. We observed a zero valued Schottky barrier at the resulting CdS⁄MWCNTs interface, thus the MWCNTs works as ohmic contacts for the CdS NPs. The formation of the ohmic contact corroborates the results regarding charge transfer from NPs to CNTs in hybrid materials and indicates the possibility to use MWCNTs as charge collectors in CdS based devices.

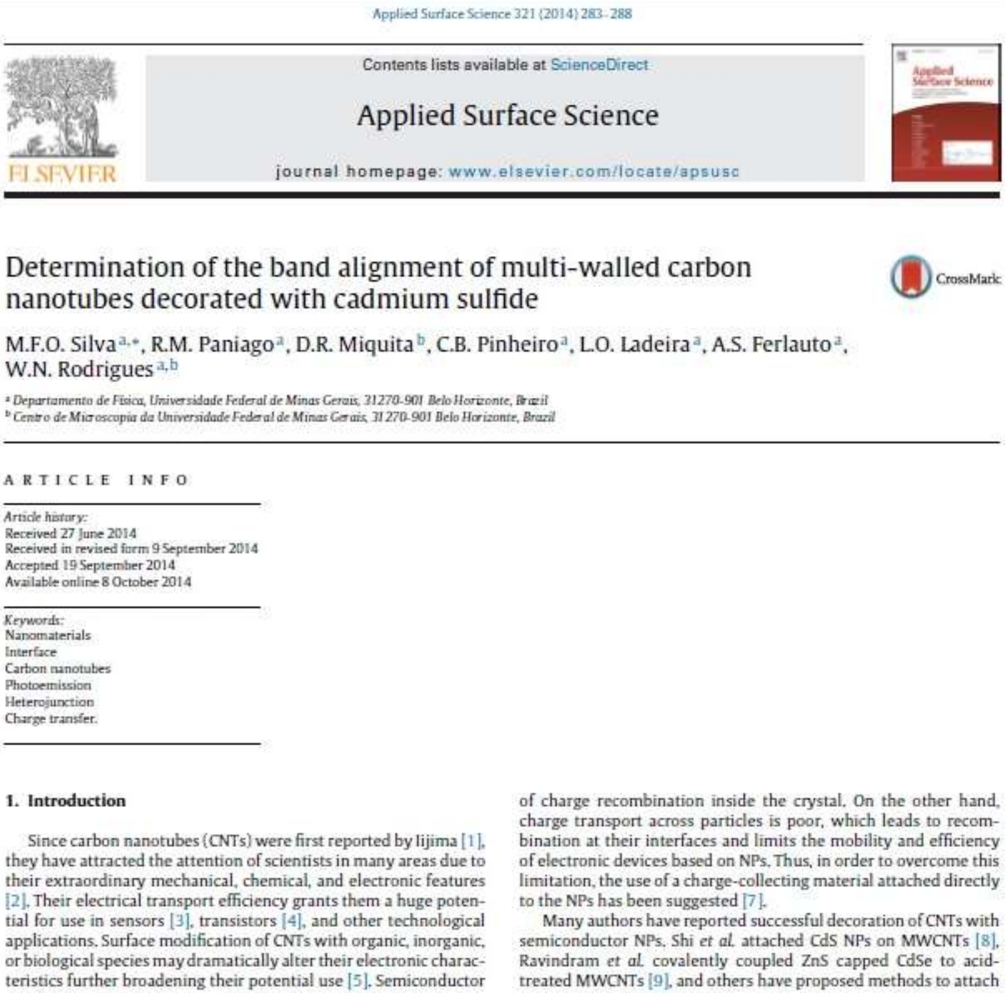

Applied Surface Science 321 (2014) 283–288

Contents lists available at ScienceDirect

Applied Surface Science

journal homepage: www.elsevier.com/locate/apsusc

Determination of the band alignment of multi-walled carbon nanotubes decorated with cadmium sulfide

M.F.O. Silva[a,*], R.M. Paniago[a], D.R. Miquita[b], C.B. Pinheiro[a], L.O. Ladeira[a], A.S. Ferlauto[a], W.N. Rodrigues[a,b]

[a] *Departamento de Física, Universidade Federal de Minas Gerais, 31270-901 Belo Horizonte, Brazil*
[b] *Centro de Microscopia da Universidade Federal de Minas Gerais, 31270-901 Belo Horizonte, Brazil*

ARTICLE INFO

Article history:
Received 27 June 2014
Received in revised form 9 September 2014
Accepted 19 September 2014
Available online 8 October 2014

Keywords:
Nanomaterials
Interface
Carbon nanotubes
Photoemission
Heterojunction
Charge transfer.

1. Introduction

Since carbon nanotubes (CNTs) were first reported by Iijima [1], they have attracted the attention of scientists in many areas due to their extraordinary mechanical, chemical, and electronic features [2]. Their electrical transport efficiency grants them a huge potential for use in sensors [3], transistors [4], and other technological applications. Surface modification of CNTs with organic, inorganic, or biological species may dramatically alter their electronic characteristics further broadening their potential use [5]. Semiconductor

of charge recombination inside the crystal. On the other hand, charge transport across particles is poor, which leads to recombination at their interfaces and limits the mobility and efficiency of electronic devices based on NPs. Thus, in order to overcome this limitation, the use of a charge-collecting material attached directly to the NPs has been suggested [7].

Many authors have reported successful decoration of CNTs with semiconductor NPs. Shi *et al.* attached CdS NPs on MWCNTs [8], Ravindram *et al.* covalently coupled ZnS capped CdSe to acid-treated MWCNTs [9], and others have proposed methods to attach

II APPENDIX B

"Synthesis of iron pyrite thin films by Russian Doll sulfurization apparatus". Silva, MFO *et al*, Thin Solid Films, **616** (2016) 303 – 310

Abstract

In this work, we present a sulfurization apparatus, we call Russian Doll, which provides a quasi-stationary sulfur rich environment. We prepared several pyrite films using the technique to sulfurize iron oxide films. We studied the influence of the synthesis parameters in the phase composition and microstructure of the disulfide films. We found no traces of iron oxides nor of secondary iron sulfide phases, such as pyrrhotite. Nevertheless, we observed the formation of the marcasite polymorph at two different temperature ranges, due to the similarity in the thermodynamic properties of both disulfide phases. At temperatures lower than 550 °C, however, marcasite undergoes a transformation reaction to pyrite, which is completed after 4 h at 550 °C. At temperatures higher than 550 °C, pyrite slowly decomposes producing pyrrhotite and sulfur gas, due to the high sulfur equilibrium fugacity. During cooling, the sulfur equilibrium fugacity drops shifting the reaction inversely towards the formation of iron disulfide, resulting in a core-surface pattern of pyrite-marcasite. We also observed that oxide films with larger particles generated pyrite films also with larger particles.

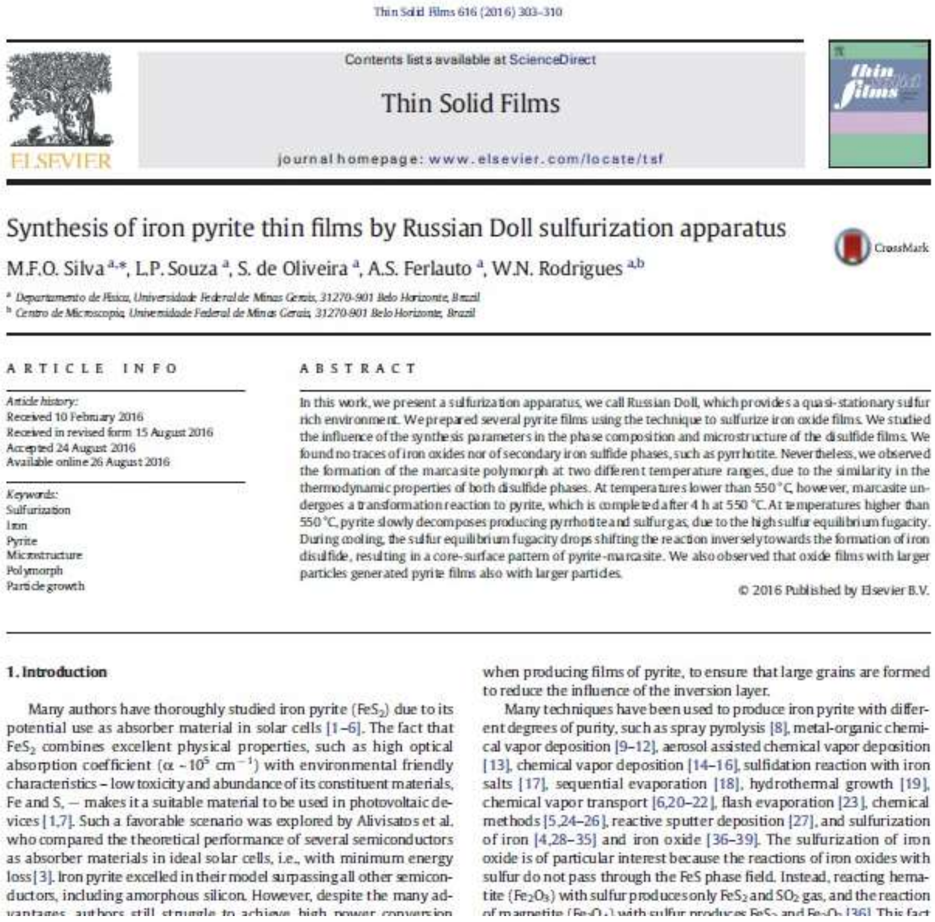

Thin Solid Films 616 (2016) 303–310

Contents lists available at ScienceDirect

Thin Solid Films

journal homepage: www.elsevier.com/locate/tsf

Synthesis of iron pyrite thin films by Russian Doll sulfurization apparatus

M.F.O. Silva [a,*], L.P. Souza [a], S. de Oliveira [a], A.S. Ferlauto [a], W.N. Rodrigues [a,b]

[a] Departamento de Física, Universidade Federal de Minas Gerais, 31270-901 Belo Horizonte, Brazil
[b] Centro de Microscopia, Universidade Federal de Minas Gerais, 31270-901 Belo Horizonte, Brazil

ARTICLE INFO

Article history:
Received 10 February 2016
Received in revised form 15 August 2016
Accepted 24 August 2016
Available online 26 August 2016

Keywords:
Sulfurization
Iron
Pyrite
Microstructure
Polymorph
Particle growth

ABSTRACT

In this work, we present a sulfurization apparatus, we call Russian Doll, which provides a quasi-stationary sulfur rich environment. We prepared several pyrite films using the technique to sulfurize iron oxide films. We studied the influence of the synthesis parameters in the phase composition and microstructure of the disulfide films. We found no traces of iron oxides nor of secondary iron sulfide phases, such as pyrrhotite. Nevertheless, we observed the formation of the marcasite polymorph at two different temperature ranges, due to the similarity in the thermodynamic properties of both disulfide phases. At temperatures lower than 550 °C, however, marcasite undergoes a transformation reaction to pyrite, which is completed after 4 h at 550 °C. At temperatures higher than 550 °C, pyrite slowly decomposes producing pyrrhotite and sulfur gas, due to the high sulfur equilibrium fugacity. During cooling, the sulfur equilibrium fugacity drops shifting the reaction inversely towards the formation of iron disulfide, resulting in a core-surface pattern of pyrite-marcasite. We also observed that oxide films with larger particles generated pyrite films also with larger particles.

1. Introduction

Many authors have thoroughly studied iron pyrite (FeS_2) due to its potential use as absorber material in solar cells [1–6]. The fact that FeS_2 combines excellent physical properties, such as high optical absorption coefficient ($\alpha \sim 10^5$ cm^{-1}) with environmental friendly characteristics – low toxicity and abundance of its constituent materials, Fe and S, – makes it a suitable material to be used in photovoltaic devices [1,7]. Such a favorable scenario was explored by Alivisatos et al. who compared the theoretical performance of several semiconductors as absorber materials in ideal solar cells, i.e., with minimum energy loss [3]. Iron pyrite excelled in their model surpassing all other semiconductors, including amorphous silicon. However, despite the many advantages, authors still struggle to achieve high power conversion

when producing films of pyrite, to ensure that large grains are formed to reduce the influence of the inversion layer.

Many techniques have been used to produce iron pyrite with different degrees of purity, such as spray pyrolysis [8], metal-organic chemical vapor deposition [9–12], aerosol assisted chemical vapor deposition [13], chemical vapor deposition [14–16], sulfidation reaction with iron salts [17], sequential evaporation [18], hydrothermal growth [19], chemical vapor transport [6,20–22], flash evaporation [23], chemical methods [5,24–26], reactive sputter deposition [27], and sulfurization of iron [4,28–35] and iron oxide [36–39]. The sulfurization of iron oxide is of particular interest because the reactions of iron oxides with sulfur do not pass through the FeS phase field. Instead, reacting hematite (Fe_2O_3) with sulfur produces only FeS_2 and SO_2 gas, and the reaction of magnetite (Fe_3O_4) with sulfur produces FeS_2 and Fe_2O_3 [36]. This fact